Synthesis, Functionalization and Applications of Carbon Nanotubes

A THESIS SUBMITTED TO THE

UNIVERSITY OF PUNE

FOR THE DEGREE OF

DOCTOR OF PHILOSOPHY

(IN CHEMISTRY)

BY

GIRISH VILAS ARABALE

PHYSICAL & MATERIALS CHEMISTRY DIVISION

NATIONAL CHEMICAL LABORATORY

PUNE- 411008, INDIA

FEBRUARY 2011

DECLARATION

I hereby declare that the work incorporated in the thesis entitled "**Synthesis, Functionalization and Applications of Carbon Nanotubes**" submitted for the degree of Doctor of Philosophy to the University of Pune, has been carried out by me at the Physical Chemistry Division, National Chemical Laboratory, Pune from February, 2006 to August, 2009 under the supervision of Dr. Jayesh Bellare (Research Guide) and Dr. Sourav Pal (Research Co-Guide). The work is original and has not, in full or in part, formed the basis for the award of any degree, diploma, associateship, fellowship, titles in this or any other University or other institution of higher learning. I further declare that the material obtained from other sources has been duly acknowledged in the thesis.

Girish Arabale

Date:

Place: Physical Chemistry Division,
National Chemical Laboratory
Pune - 411008

CERTIFICATE

Certified that the work incorporated in the thesis entitled "**Synthesis, Functionalization and Applications of Carbon Nanotubes**" submitted by Girish Arabale for the degree of Doctor of Philosophy to the University of Pune, was carried out by the candidate under my supervision in Physical Chemistry Division, National Chemical Laboratory, Pune- 411 008. Such material as has been obtained from other sources has been duly acknowledged in the thesis.

Dr. Jayesh Bellare
[Research Guide]

Dr. Sourav Pal
[Research Co-Guide]

Date:

Place: Physical Chemistry Division,
National Chemical Laboratory
Pune - 411008

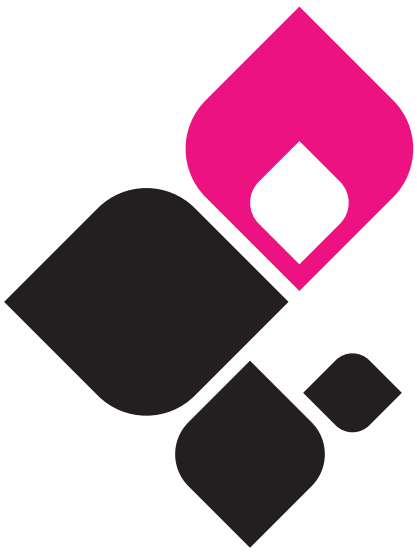

Dedicated to
My Parents

The physicist Leo Szilard once announced to his friend Hans Bethe that he was thinking of keeping a diary:

"I don't intend to publish. I am merely going to record the facts for the information of God."

"Don't you think God knows the facts?" Bethe asked.

"Yes," said Szilard.

"He knows the facts, but He does not know this version of the facts."

-Hans Christian von Baeyer,

Taming the Atom

Table of Contents

Acknowledgements

I take this opportunity to express my gratitude to Dr. Jayesh Bellare, my research supervisor, and Dr. Sourav Pal, my research co-supervisor, for their invaluable guidance, support, and advice throughout the course of this investigation. Thanks for the solid support especially during my difficult times.

I am extremely grateful to Dr. Ajay Sood (IISc) and Dr. A. M. Rao (Clemson University) for the stimulating scientific discussions, suggestions, and occasional help in characterizations.

I am thankful to Dr. Vijayamohanan, Dr. Mulla, Dr. Vernekar, Dr. Satish Ogale, and Dr. Wadgaonkar for their suggestions, advice, and valuable discussions.

I express my heartfelt thanks to Shri Subhash Katte for his help and support. Thanks are also due to our divisional staff Shri Dipak Jori and Shri S. F. Punekar for their willing cooperation.

Many thanks to Salil, Niraj, Shweta, Helois, and Sangram who worked with me for their final semester projects. They were always eager to try new things and most of their projects culminated into full-fledged research topics.

I owe deeply to ever-trustful friends Sumant, Mahesh, Pankaj, Rakesh, Satish, Hamid, Ravi-Sonali, Mukta, Rupali, Archana, Sarvesh, Mukund, Abhijit, Ganesh, Avinash, Sandeep, Chandrashekahr, Anil, Shekahr, Hrushi, Atul, Deepali, Jiten, Nilkashi, Parimal, Rajeshwari, and Mandar for all their affection and help.

Finally, I am deeply and thoroughly indebted to my family members for their sacrifices, patience, and kind support throughout my upbringing. It is difficult to express in words, my gratitude to my parents for their enormous support and inspiration through out my PhD work.

Synthesis, Functionalization and Applications of Carbon Nanotubes

Abstract

The discovery of fullerenes in 1985 and carbon nanotubes (CNTs) in 1991 by Iijima has permanently altered the dogma that carbon can only exist in its two stable allotropes, graphite and diamond. The preparation of molecular and polymeric acetylenic carbon allotropes as well as carbon-rich nanometer sized structures has opened new avenues in fundamentals and technological research at the interface of chemistry and other branches of science. Of these allotropes, CNTs are unique nanostructures with remarkable electronic, structural and mechanical properties. They can be considered conceptually as a prototype one-dimensional (1D) quantum wire. An ideal nanotube can be visualized as a hexagonal network of carbon atoms that has been rolled upto make a seamless hollow cylinder. These hollow cylinders can be tens of micrometers long with diameters typically around ~ 1.4 nm and each end of the long cylinder capped with half a fullerene molecule. Single-Walled nanotube (SWCNT) with one atom in wall thickness is the fundamental structural unit. These structural units are the building blocks of multi-walled carbon nanotubes (MWCNTs), which contain multiple coaxial cylinders of ever increasing diameters about a common axis.

SWCNTs offer a unique combination of electrical, mechanical, thermal, and optical properties that make them highly promising materials for numerous applications ranging from solid-state nanoelectronics, sensing, nanocomposites, biomedical devices, and cellular delivery, to making novel nanoarchitectures. The realization of these applications, particularly biological ones, has been seriously hindered by the insolubility of SWCNTs in water. However, even though exploration of the biomedical applications of carbon nanotubes is in nascent stages, it has already shown significant promise. Such include their use as DNA and protein biosensors or ion channel blockers.

One of the most commonly used strategies to render carbon nanotubes soluble in aqueous media, and therefore, potentially useful to biomedical applications, is through their surface functionalization. Functionalization of carbon nanotubes can be achieved either by covalent or noncovalent methodologies.

The main approaches for the modification of these quasi one-dimensional structures can be grouped into three categories: (a) the covalent attachment of chemical groups through reactions onto the π-conjugated skeleton of CNT; (b) the noncovalent adsorption or wrapping of various functional molecules; and (c) the endohedral filling of their inner empty cavity.

The chemistry of CNT is a current subject of intense research, which produces continuous advances and novel materials. However, the controlled functionalization of CNT has not yet been fully achieved. Solubility continues to be an issue, and new purification and characterization techniques are still needed to realize their full potential.

Objectives of the Present Thesis

The main theme of this thesis is the synthesis of carbon nanostructures, and strategies to functionalize them to realize their applications in energy storage, high-performance composites and biology. A brief outline of the aims and objectives of the present thesis along with the methodologies that are used in the studies is presented in this section.

- **Synthesis of carbon nanostructures by CVD method**
    - Selection of proper hydrocarbon precursors and metal catalyst.
    - Optimization of growth parameters such as hydrocarbon/metal ratio, temperature etc. to grow perfect nanotubes at large scales.
    - Purification and characterization of CNTs.
- **Functionalization carbon nanotubes with different entities**
    - Chemical functionalization with metal nanoparticles, organic molecules, polymers through reactions onto the π-conjugated skeleton of CNT.
    - The noncovalent adsorption or wrapping of various functional molecules especially proteins.
    - Develop a theoretical framework to understand various interactions of CNTs with different molecules.
    - Characterization of functionalized CNTs by various techniques like IR, Raman, SEM, TEM, AFM, fluorescence, UV-VIS, and XRD, etc.
- **Applications of functionalized carbon nanotubes**
    - CNTs as an electrode material in energy storage devices such as supercapacitors, fuel cells and batteries.
    - High-performance Polymer composites for mechanical reinforcement and other applications.
    - Biomass conversion.
    - CNTs as a bio-imaging tool for cytological investigation.
    - Bioapplications such as strengthening the bone structure by forming biocomposites.

Accordingly this thesis has been divided in three parts namely- **A) Energy Storage** (Chapters 1-6)**, B) High-performance composites** (Chapters 7-9), and **C) Bioapplications (**Chapters 10-12**)**. This categorization is not strict but to provide a logical structure to the thesis concordant to the central theme as the scope of some of the chapters may overlap with other parts because of their cross-disciplinary nature.

The **first chapter** provides a comprehensive introduction to carbon nanotubes with special emphasis on their synthesis, functionalization strategies and their applications in energy storage, structural reinforcement and biology. The **second chapter** deals with various nanostructures of carbon such as carbon beads, nanotubes prepared by CVD method varying the metal-hydrocarbon ratio along with temperature. The **third chapter** describes the pseudocapacitive behavior of multi-walled carbon nanotubes functionalized with hydrous ruthenium oxide for supercapacitor applications. The **fourth chapter** shows that the inherent electrochemical capacitance of MWCNTs can be significantly enhanced by Iridium oxide functionalization. The **fifth Chapter** describes the fabrication of all solid-state supercapacitor prototypes that can operate at elevated temperatures (150-180 °C). The **sixth chapter** describes the supercapacitor applications of single-walled carbon nanotubes- polyacrylonitrile composites.

The **seventh chapter** describes the functionalization of SWCNTs with a variant of polybenzimidazole polymer that selectively attaches to semiconducting carbon nanotubes which is reflected in their optical function. Nanotubes enhance the optical signal of polymer in the UV-Visible region and bleach it in the NIR region. The **eighth chapter** describes the solubilities of single-walled carbon nanotubes in variety of organic solvents when wrapped through Pi-conjugation with a polyimide chain synthesized from cardanol-a major constituent of Cashew Nut Shell Liquid. The **chapter nine** describes the synthesis of matrix composite prepared by blending polyvinylidene fluoride with very small amounts of multi-walled carbon nanotubes (1-6%) that shows enhanced thermal stability along with a more than 100 % increase in modulus above the glass transition temperature.

The **chapter 10** describes a novel method for bio-inspired enzymatic synthesis of nanosized hydroxyapatite and its polymorphs on carbon nanotubes matrix using cheap agro-based waste materials i.e. wheat bran and a novel extra cellular enzyme phytase, produced by solid state fermentation of fungus Aspergillus niger. The **chapter 11** describes a superior method for the conversion of cellulose to glucose and cellooligomers using carbon nanotubes. The **chapter 12** describes a unique way to tag the amine functionality on carbon nanotubes using an aldehyde molecule which forms indole adduct with two adjacent primary amine groups. This indole adduct shows strong fluorescence signal in the 380-450 nm region. The **chapter 13** summarizes and concludes the work described in above chapters along with an outline of possible future work.

CHAPTER 1

General introduction to carbon nanotubes.

This chapter provides a comprehensive introduction to carbon nanotubes with special emphasis on their synthesis, functionalization strategies and their applications in energy storage, structural reinforcement and biology.

1.1 Introduction

The discovery of fullerenes [1] in 1985 and carbon nanotubes (CNTs) in 1991 by Iijima [2] has permanently altered the dogma that carbon can only exist in its two stable allotropes; graphite and diamond. The preparation of molecular and polymeric acetylenic carbon allotropes as well as carbon-rich nanometer sized structures has opened new avenues in fundamentals and technological research at the interface of chemistry and other branches of science. Of these allotropes, CNTs are unique nanostructures with remarkable electronic, structural and mechanical properties. They can be considered conceptually as a prototype one-dimensional (1D) quantum wire. An ideal nanotube can be visualized as a hexagonal network of carbon atoms that has been rolled upto make a seamless hollow cylinder. The length of these hollow cylinders can be tens of micrometers with diameters typically around 0.7 - 10 nm and each end of the long cylinder capped with half a fullerene molecule. Single-Walled nanotube (SWCNT) with one atom in wall thickness is the fundamental structural unit. These structural units are the building blocks of multi-walled carbon nanotubes (MWCNTs), which contain multiple coaxial cylinders of ever increasing diameters about a common axis. Figure 1-1

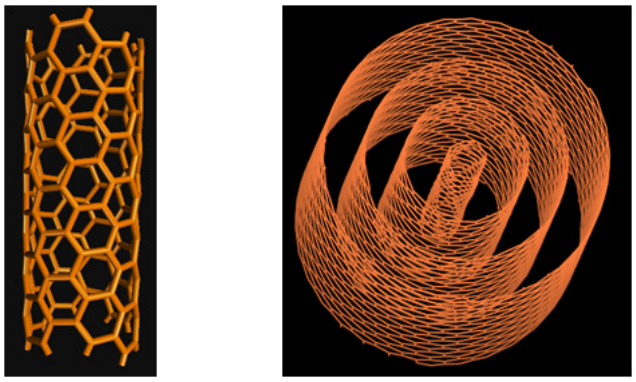

Figure 1-1. Conceptual diagrams of single-walled carbon nanotubes (SWCNT; left side) and multi-walled carbon nanotubes (MWCNT; right side).

shows the conceptual diagrams of SWCNT- a rolled sheet of graphene and MWCNT- a collection of concentric SWCNTs with different diameters. From a fundamental point of view the most distinct features of SWCNTs are their electronic (semiconducting or metallic), mechanical, optical and chemical properties whereas the properties of MWCNTs are very different from their single-walled counterparts. The potential applications and the promises offered by CNTs are varied greatly and they often utilize their unique electrical, mechanical (Young's modulus ~1 TPa) and structural properties. Examples include electronics (transistors, memory storage devices), opto-electronics (LED, lasers), sensors, field-emission devices (scanning electron microscopes, displays), tough materials (reinforced polymer composites), energy storage devices (supercapacitors, batteries, fuel cells), biology (fluorescent markers, labels, drug delivery carriers), catalysis and gas storage.

1.2 Structure of CNTs

CNTs have strong structural correlations particularly with crystalline 3D graphite, and its constituent 2D layers called graphene layers. The electronic configuration of carbon is $1s^2$, $2s^2\,2p^2$. The crystalline phase of carbon involves $2s$, $2p_x$, $2p_y$, and $2p_z$ orbitals which are important in the formation of covalent bonds. As the energy difference between $2p$ and $2s$ levels is small, the electronic wavefunctions for the four electrons in these orbitals can readily mix with each other that give rise to three possible hybridizations- *sp*, sp^2, and sp^3. These hybridizations involve different bonding states resulting in different structural arrangements such as *sp* bonding gives rise to planar structure, sp^2 bonding to planar structures and sp^3 bonding to tetrahedral structures. Thus carbon can exist in a variety of forms such as graphite, diamond, fullerenes and CNTs. Bonding in CNTs is essentially sp^2. However the strong curvature results in quantum confinement causing σ-π rehybridization with three σ bonds slightly out of plane and to compensate these; π orbital is more delocalized outside the tube. This is the reason why CNTs are more mechanically stronger, more conductive, and chemically and biologically more active than graphite.

The structure of CNTs has been explored early by high-resolution transmission electron microscopy (HRTEM) [3] and scanning tunneling microscopy (STM) [4]. The structure of SWCNT is conveniently explained in terms of its 1D unit cell, defined by the chiral vectors C_h as shown in Figure 1-2. The circumference of any CNT is expressed in

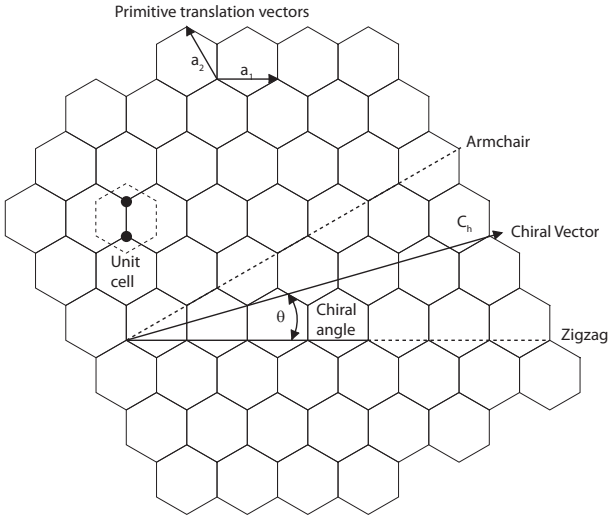

Figure 1-2. Honeycomb lattice of carbon atoms with chiral vector C_h defined by unit vectors a_1 and a_2 and the chiral angle θ.

terms of the chiral vector $C_h = na_1 + ma_2$ (where n & m are integers) which connects two crystallographically equivalent sites on a 2D graphene sheet [5]. A nanotube (n,m) is

formed by rolling a graphite sheet along the chiral vector $C_h = na_1 + ma_2$ on the graphite where a_1 and a_2 are graphite lattice vector. Three distinct types of nanotubes structures can be generated by rolling up the graphene sheet into a cylinder [6]. The zigzag and armchair nanotubes, respectively, correspond to chiral angles of $\theta = 0$ and 30°, and chiral nanotubes correspond to $0 < \theta < 30°$. In the (n, m) notation for $C_h = na_1 + ma_2$, the vectors $(n, 0)$ or $(0, m)$ denote the zigzag nanotubes and the vectors (n, n) denote armchair nanotubes. All other vectors (n, m) correspond to chiral nanotubes. The diameter (D) of the tube is given by the equation(1.1), where $a = |a_1| = |a_2|$ is the lattice constant of graphite.

$$D = \frac{|C_h|}{\pi} = a\frac{\sqrt{n^2 + nm + m^2}}{\pi} \qquad 1.1$$

The chiral angle θ in the chiral tubes is defined by the equation (1.2). The θ ranges from

$$\theta = \frac{\sqrt{3}\, m}{Tan(m + 2n)} \qquad 1.2$$

0 for zigzag (m = 0) and 30° for armchair (m = n) tubes. Thus using lattice constant and intertube spacing we can generate the structures of SWCNT and MWCNT. Figure 1-3 shows the schematic models of armchair, chiral and zigzag SWCNTs. Experimental

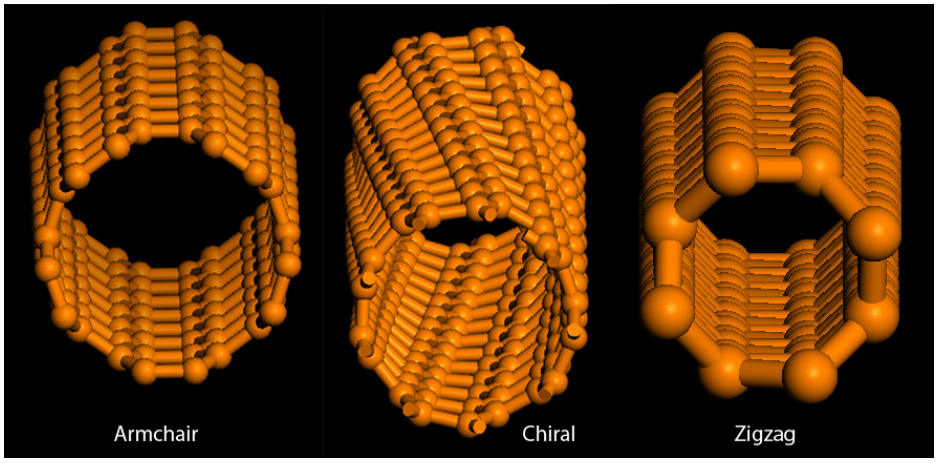

Figure 1-3. Conceptual models of armchair (n = 5, m = 5), chiral (n = 5, m = 4) and zigzag (n = 5, m = 0) SWCNTs. The C-C bond length in all the models is 1.422 Å. Chiral and zigzag tubes are semiconducting while armchair is metallic.

measurements and theoretical calculation have shown that the average C-C bond length in CNT is 0.142 nm or $a = |a_1| = |a_2| = 0.246$ nm with an intertubular spacing 0.34 nm[7]. Tube chirality is an important parameter in carbon nanotubes science as it bears direct relation with electronic, optical and magnetic properties of a nanotube. Controlling the chirality of CNTs is a challenging task to realize many potential applications of CNTs.

1.3 Synthesis of CNTs

The synthesis of CNTs is carried out mainly by three methods; laser ablation [8], arc discharge [9], and chemical vapor deposition (CVD) [10]. A summary of these major synthesis methods along with their efficiency is given in Table 1-1.

Table 1-1. A summary of carbon nanotubes synthesis methods along with their efficiency. Among these methods chemical vapor deposition is the only scalable method for industrial production [11].

Methods	Arc discharge	Chemical vapor deposition	Laser ablation
How	Connect two graphite rods to a power supply; place them a few millimeters apart. At 100 amps, carbon vaporizes and forms hot plasma.	Place substrate in oven, heat to 600 °C, and slowly add a carbon-bearing gas such as methane. As gas decomposes it frees up carbon atoms, which recombine in the form of CNTs.	Blast graphite with intense laser pulses; use the laser pulses to generate carbon gas from which the CNTs form; try various conditions until hit on one that produces prodigious amounts of SWCNTs.
Typical yield	30 - 90%	20 - 100%	Up to 70%
SWCNT	Short tubes with diameters of 0.6 - 1.4 nm.	Long tubes with diameters ranging from 0.6 - 4 nm.	Long bundles of tubes (5 - 20 microns), with individual diameter from 1 - 2 nm.
MWCNT	Short tubes with inner diameter of 1 - 3 nm and outer diameter of approximately 10 nm.	Long tubes with diameter ranging from 10 - 240 nm.	Not very much interest in this technique, as it is too expensive, but MWCNT synthesis is possible.
Pros	Can easily produce SWCNT, MWCNTs. SWCNTs have few structural defects; MWCNTs without catalyst, not too expensive, open air synthesis possible.	Easiest to scale up to industrial production; long length, simple process, SWCNT diameter controllable, quite pure.	Primarily SWCNTs, with good diameter control and few defects. The reaction product is quite pure.
Cons	Tubes tend to be short with random sizes and directions; often needs a lot of purification	CNTs are usually MWCNTs and often riddled with defects	Costly technique, because it requires expensive lasers and high power requirement, but is improving.

1.4 Functionalization of CNTs

The outstanding mechanical, electronic and structural properties of CNTs make them ideal nanoscale materials. A wide variety of applications ranging from electronic devices, composite materials, energy storage, field emission, sensors, and medicine have been envisioned for CNTs. Most of these applications utilize the unique properties of CNTs such as high mechanical strength, excellent electrical and thermal conductivity. However the inert nature of CNTs hinders their manipulation and subsequently limits their proposed applications. CNTs contain hexagonal frameworks of conjugated carbon atoms with sp^2 hybridization which makes them chemically inert and limits their solubility in all solvents. Some of these difficulties can be overcome by chemical functionalization of CNTs at their defect sites or at the ends [12]. The formation of covalent linkages not only enhances the solubility of CNTs in various solvents but also maintains the structural integrity of by keeping the nanotube skeleton intact. However this method involves the modification of sp^2 carbon framework that results in the alteration of inherent physical properties; especially the electronic properties of CNTs.

An alternative strategy for preserving the intrinsic electronic and mechanical properties of CNTs consists in the noncovalent functionalization of CNTs as it does not destroy the conjugation in the CNTs [13]. Noncovalent functionalization usually involves physical adsorption of suitable molecules onto the sidewalls of CNTs through hydrophobic, van der Waals and electrostatic or ionic interactions. It is generally achieved by polymer wrapping, surfactant adsorption, or interaction with supramolecules such as porphyrins or biomolecules such as DNA, proteins and peptides.

The chemical reactivity of CNTs can be understood in the context of other carbon allotropes- graphite and fullerenes. Graphite and graphene have planar aromatic sp^2 bonded carbon framework which makes them chemically inert. However functionalization of spherical fullerenes can be carried out very easily. The relatively high reactivity of C_{60} is due to the introduction of strain by bending the planar graphene sheet into a three-dimensional carbon framework. The chemical reactivity in non-planar conjugated carbon structures arises from two basic factors: pyramidalization of the conjugated carbon atoms [14], and π-orbital misalignment between adjacent pairs of conjugated atoms [15]. Fullerenes and CNTs both have spherical carbon structures. The curvature of fullerenes is morphed in two dimensions while that of CNTs is in one dimension only. As a result, the reactivity of fullerenes is due the conversion of trigonal carbon atoms (sp^2 -hybridized) to tetrahedral carbon atoms (sp^3 -hybridized) which results in the release of pyramidalization strain energy. This is because the pyramidalization angle θ_p of the curvature at a conjugated carbon atom of C_{60} ($\theta_p = 11.64°$) is quite closer to ideal tetrahedral angle ($\theta_p = 19.47°$) than to planar geometry required for trigonal hybridization ($\theta_p = 0$). There is no π-orbital misalignment in C_{60} because of their spheroidal geometry.

A CNT with the same radius as C_{60} exhibits a less distorted π-framework due to its 1D curvature. The C-C bonds at the tube ends experience a similar degree of strain due to pyramidalization to that of the equivalent fullerene. However, as the degree of

curvature in a CNT is much less than that in a fullerene of similar diameter, the carbon-carbon bonds along the sidewall of a CNT are less reactive than those in the end caps.

Another factor that governs the reactivity of CNTs is the π-orbital misalignment. In the case of the armchair CNT, there are two types of C-C bonds in the sidewall: one is parallel to the circumference plane (or perpendicular to the axis of the CNT) with a π-orbital misalignment angle of $\Phi = 0°$, whereas the other lies at an angle to the circumference plane with a π-orbital misalignment angle of $\Phi = 21.3°$ [16]. This π-orbital misalignment is the source of torsional strain in nanotubes and the relief of this strain energy is the basis of CNTs relative reactivity.

There is a direct correlation between tube diameter and reactivity as both the pyramidalization angle and the π-orbital misalignment angle scale inversely with the diameter [17]. As a result, smaller CNTs are more reactive than their larger counterparts. Tubes with similar diameter distributions may exhibit different chiralities and their reactivity can not be explained by the usual parameters Φ and θ_p alone as they do not take account of strain energies of various C-C bonds present in different tube chiralities. The strain energy of a C-C bond perpendicular to the tube axis is more pronounced than the strain in C-C bonds parallel to the tube axis. Therefore, a new parameter- the local curvature radius has been introduced to explain the chirality selective functionalization [18]. Thus understanding the correlation between electronic structure and chemical reactivity is of utmost importance for the manipulation of semiconducting and metallic SWCNTs properties.

As mentioned earlier, CNT functionalization can be divided into different categories:

1.4.1 Noncovalent exohedral functionalization

Noncovalent interactions of CNTs with small aromatic molecules such as cyclohexane, cyclohexadiene, benzene, anthracene derivatives, pyrene and polyaromatic derivatives through π-π interactions [19]. Noncovalent interactions of CNTs with heterocyclic polyaromatic systems such as porphyrins [20], phthalocyanines [21], and sapphyrins. Noncovalent interactions of CNTs with surfactants [22] and ionic liquids [23] for the solubilization of CNTs. Noncovalent interactions of CNTs with polymers that includes polymeric amphiphiles such as poly (diallyldimethylammonium) chloride (PDDA), polystyrene sulfonate, conjugated polymers like poly (phenylenevinylene), poly (m - phenylenevinylene - *co* - 2, 5 - dioctyloxy - *p* - phenylenevinylene). Noncovalent interactions of CNTs with biopolymers such as DNA.

1.4.2 Endohedral functionalization

Endohedral functionalization of CNTs involves trapping of fullerenes, metal atoms or metal clusters into a CNT cylinder. It naturally combines the inherent properties of CNTs and encapsulated species together. Experiment have been done to feel MWCNTs with cesium, selenium, sulphur [24], lead [25], silver [26], cobalt and nickel [27], etc.

1.4.3 Defect-group functionalization

Defects in CNTs serve as anchor groups for further functionalization to generate highly functional nanotubes derivatives. One of the common method to generate defects on CNTs is liquid-phase or gas-phase oxidative process. Widely used oxidants are conc. HNO_3, H_2SO_4, mixtures of hydrogen peroxide and H_2SO_4 (piranha solution), gaseous oxygen, ozone and $KMnO_4$ [28]. Oxidative treatment not only removes the amorphous carbon impurities but also creates surface oxygenated functionalities such as carboxylic, quinonic, ketonic and aldehydic among which carboxylic is predominant. The carboxylic functionalities is usually treated with thionyl chloride to convert into corresponding acid chlorides which are usually reacted with amines to form CNT amide derivatives [29]. The carboxylic acid-based amidation and esterification sequence is the most widely used route for the construction of soluble CNT derivatives. The amide- and ester-derivatized CNTs have also been used for the generation of cofunctionalized carbon nanotubes, where the first moiety is used for CNT solubilization and the second to express additional functionality [30].

1.4.4 Direct sidewall functionalization of CNTs

The direct chemical functionalization of nanotube sidewalls is usually carried by addition reactions such as fluorination and nucleophilic substitution [31], hydrogenation [32], epoxidation [33], cycloaddition reactions such as addition of carbenes [34], nitrenes [35], and Diels–Alder reactions [36], radical-based functionalization [37], diazonium-based functionalization [38]. The main drawback of this functionalization is the loss of electronic and mechanical properties of CNTs.

1.5 Unique properties of CNTs

CNTs exhibit unique electronic, structural, optical and mechanical properties mainly due their 1D structure. The most important properties of CNTs and their molecular background are stated below.

1.5.1 Electronic properties

The electronic structure SWCNT depends critically on the chiral *n* and *m* integers. In particular, if |n-m| is a multiple of three, then the nanotube acts as a 1D metal and otherwise it behaves as a semiconductor. In metallic SWCNT, the density of electronic states at the Fermi level is non-zero. Since n and m can have any value, one third of SWCNT are expected to be metallic and the remaining two thirds are expected to be semi-conducting having an energy band-gap. The size of this band gap is given by $E_g = 0.8/D$ eV, where *D* is the diameter of the nanotube [7]. Metallic SWCNTs have two 1D sub-bands that cross the Fermi level otherwise they are quite similar to semi-conducting tubes. These metallic SWCNTs are fascinating, particularly because they have been shown to be act as ballistic conductors with the conductance ($G = 4\ e^2/h$, where '*e*' is the charge on electron and '*h*' is Planck constant) of approximately 150 μS. The semiconducting and metallic structure of SWCNT exhibits remarkable electronic

behavior of nanotubes that may be exploited in several potential applications such as molecular electronics, quantum computing etc. CNT is predicted to act as a 1D quantum wire, at a finite length turns it into a 1D quantum dot, which is a generic example of a small, confined structure containing electrons. A perfect metallic nanotube is supposed to be a ballistic conductor. Thus CNTs present an ideal system for the realization of molecular electronics for making devices such as field-effect transistors, single electron-tunneling transistors or rectifiers.

1.5.2 Optical properties

Defect-free SWCNTs are ideal for optical and optoelectronic applications as they offer direct band gap and well-defined band and subband structure. Optical properties of SWCNTs have been explored using fluorescence, UV-VIS-NIR, and resonant Raman spectroscopy [39]. Optical properties can be understood from the band structure or electronic density states (DOS) of a SWCNT. The DOS of SWCNT are dominated by sharp singularities called van Hove singularities [40] which are characteristics of a truly uni-dimensional electronic system. In terms of DOS, these singularities represent the distinct energy levels that can be occupied by an electron, with the distance between these singularities indicating the energy required for an electron to transition between adjacent levels. The distribution of these van Hove singularities governs the electronic properties of SWCNT system.

The band gap and van Hove singularities play important roles in the optical properties of SWCNTs. When the DOS is tuned by varying the Fermi level of the SWCNT with these van Hove singularities, visible light can be used to resonate with the second transition- where electrons are transferred from an energy level directly below the bandgap to an energy level directly above the bandgap. With this resonance, the electron-hole pair will decay to the band edge causing light to be emitted in the near infrared region. CNTs are one of the few materials to emit stable near-infrared radiation [41]. The optical signal in the near-infrared region can used to examine the chiralities of of semiconducting SWCNTs. The metallic SWCNTs do not have a bandgap, but they have a dispersed van Hove singularity and show absorption in the blue to UV region. This absorption signal can be used to study different kinds of metallic SWCNTs [42].

1.5.3 Mechanical properties

Nanotube framework is made up of all σ bonding which is the strongest in nature and thus CNT can be regarded as ultimate fibre with the strength in its tube axis. Experimental measurements and theoretical calculations show that CNT possess highest Young modulus and tensile strength making it more stiffer than diamond [43].

Table 1-2 summarizes the mechanical properties of CNTs, graphite and steel [44]. Generally CNTs are stronger than graphite because the axial component of σ bonding is greatly increased when a graphite sheet is rolled over to form a seamless cylindrical structure of SWCNT. Young's modulus is independent of chiralities but dependent on tube diameter. MWCNTs have greater Young's modulus than SWCNTs because of contributions from coaxial coupling or van der Waals force. The elastic response of CNTs

is also remarkable as they can sustain up to 15% tensile strain before fracture.

Table 1-2. Comparison of mechanical properties of different types carbon nanotubes with graphite and steel.

Material	Young's modulus (GPa)	Tensile Strength (GPa)	Density (g/cm^3)
MWCNT	1200	-150	2.6
SWCNT	1054	75	1.3
SWCNT bundle	563	-150	1.3
Graphite (in-plane)	350	2.5	2.6
Steel	208	0.4	7.8

1.6 Applications of CNTs

As described in the previous sections, CNTs possess unique electronic, structural and mechanical properties and a broad range applications have been proposed, including, for example: energy storage such as hydrogen storage, fuel cells, and the lithium battery, composites for coating, filling, and structural materials, transistors, memories, logic devices, and other nanoelectronic devices, field emission devices for x-ray instruments, flat panel display, etc. Among these, applications in energy storage especially supercapacitors, high-performance polymer composites and biology are described here briefly as these are more relevant to this thesis.

1.6.1 Energy storage (supercapacitors)

CNTs due to their excellent conducting and mechanical properties are the ideal materials for energy storage devices such as supercapacitors. Their randomly entangled network presents a labyrinth of mesoporous network to the electrolyte ions, thus allowing them to access maximum surface area [45]. Moreover their chemical inertness makes them ideal choice for supercapacitor electrodes. The mechanism of charge storage across the CNT/electrolyte interface is usually by double layer formation. Functionalization of CNTs with metal oxides such as RuO_2 [46], IrO_2, MnO_2 [47], conducting polymers such as Poly(3, 4- ethylenedioxythiophene) (PEDOT), polyaniline, polypyrrole can enhance their capacitance dramatically [48]. Charge storage in these composite materials is usually involves faradaic mechanism.

1.6.2 High-performance composites

Due to their excellent mechanical (tensile modulus on the order of 1 TPa and a tensile strength 100 times greater than steel at one sixth the weight) and electrical properties, CNTs are the best reinforcing elements for polymer matrix composites. The intrinsic high conductivity of nanotubes makes them an ideal choice for making conductive polymers. Due to their high aspect ratios, CNTs have low percolation threshold than any other fillers. Many researchers have reported percolation threshold

less than 1wt.% nanotubes [49]. Table 1-3 shows the percolation thresholds of CNTs for various polymers to enhance their electrical conductivity [50].

Table 1-3. Percolation thresholds of CNTs for different polymers where electrical enhancements have been observed.

Polymer	Nanotube Type	Nanotubes Conc. (wt. %)	Percolation Threshold (wt. %)
ABS	SWCNT	0.5–10	
Epoxy	MWCNT	0.0225–0.15	0.0225–0.04
Polyimide	SWCNT	0.01–1.0	0.02–0.1
PMMA	SWCNT	0.1–8.0	<1
Polystyrene	MWCNT	1–5	<1
PmPV & PVOH	MWCNT	0.037–4.3	0.055 for both composites
PVOH	MWCNT	5–50	5–10

Most important commercial applications of CNT composites are the aerospace materials (that requires lightweight, high-strength, high-temperature-resistant composites) and in energy (nanotube-reinforced rubber seals for large oil recovery platforms). With advances in synthesis methods, the cost of CNTs is almost comparable to other regular fillers, commodities such as CNT- filled rubber tyres could become reality.

1.6.3 Biological applications

Many biological applications of CNTs have been envisaged. Their capability to penetrate into cells is the major driving force for their biomedical explorations. CNTs can translocate into a wide variety of cells by phagocytosis, endocytosis, or membrane piercing processes [51]. Experiments with plant cell walls showed that CNTs enter cells without toxicity and cells preserved their morphology and proliferation rate [52].

The possibility of endohedral functionalization provides a new approach to drug reservoirs. CNTs have been used in drug delivery for cancer treatments [53]. Experiments have also been done to explore the genetic material delivery by complexing RNA polymer poly (rU) to SWCNTs by nonspecific interactions [54]. Neuronal circuits grown on CNT substrates have shown the improvement in the neural signal transfer owing to high electrical conductivity of CNTs [55]. Semiconducting SWCNTs show photoluminescence in the near-infrared region where no biological species show any optical signal. Thus CNTs can be used in *in vitro* and *in vivo* imaging [56].

1.7 Objectives of the Present Thesis

The main theme of this thesis is the synthesis of carbon nanostructures, and strategies to functionalize them to realize their applications in energy storage, high-performance composites and biology. A brief outline of the aims and objectives of the

present thesis as well as the methodologies that are used in the studies is presented in this section.

1.7.1 Synthesis of carbon nanostructures by CVD method

- Selection of proper hydrocarbon precursors and metal catalyst.
- Optimization of growth parameters such as hydrocarbon/metal ratio, temperature etc. to grow perfect nanotubes at large scales.
- Purification and characterization of CNTs.

1.7.2 Functionalization carbon nanotubes with different entities

- Chemical functionalization with metal nanoparticles, organic molecules, polymers through reactions onto the π-conjugated skeleton of CNT.
- The noncovalent adsorption or wrapping of various functional molecules especially proteins.
- Develop a theoretical framework to understand various interactions of CNTs with different molecules.
- Characterization of functionalized CNTs by various techniques like IR, Raman, SEM, TEM, AFM, fluorescence, UV-VIS, and XRD, etc.

1.7.3 Applications of functionalized carbon nanotubes

- CNTs as an electrode material in energy storage devices such as supercapacitors, fuel cells and batteries.
- High-performance Polymer composites for mechanical reinforcement and other applications.
- Biomass conversion.
- CNTs as a bio-imaging tool for cytological investigation.
- Bioapplications such as strengthening the bone structure by forming biocomposites.

Accordingly this thesis has been divided in three parts namely- **A) Energy Storage, B) High-performance composites** and **C) Bioapplications**. This categorization is not strict but to provide a logical structure to the thesis concordant to the central theme as the scope of some of the chapters may overlap with other parts because of their cross-disciplinary nature.

1.8 References

1. H. W. Kroto, J. R. Heath, S. C. O'Brien, R. F. Curl, R. E. Smalley, Nature 1985, 318, 162-163.
2. S. Iijima, Nature 1991, 354, 56-58.
3. A. Hashimoto, K. Suenaga, A. Gloter, K. Urita, S. Iijima, Nature 2004, 430, 870-873.
4. J. W. G. Wildöer, L. C. Venema, A. G. Rinzler, R. E. Smalley, C. Dekker, Nature 1998, 391, 59-62.
5. M. S. Dresselhaus, G. Dresselhaus, R. Saito, Carbon 1995, 33, 883-891.
6. R. Saito, M. Fujita, G. Dresselhaus, M. S. Dresselhaus, Applied Physics Letters 1992, 60, 2204-2206.
7. M. Dresselhaus, G. Dresselhaus, P. Eklund, D. Jones, Science of fullerenes and carbon nanotubes, Academic Press San Diego, 1995.
8. (a) T. Guo, P. Nikolaev, A. Thess, D. T. Colbert, R. E. Smalley, Chemical Physics Letters 1995, 243, 49-54; (b) A. Thess, R. Lee, P. Nikolaev, H. Dai, P. Petit, J. Robert, C. Xu, Y. H. Lee, S. G. Kim, A. G. Rinzler, D. T. Colbert, G. E. Scuseria, D. Tománek, J. E. Fischer, R. E. Smalley, Science 1996, 273, 483-487.
9. (a) M. Tomita, Y. Saito, T. Hayashi, Japanese Journal of Applied Physics, Part 1: Regular Papers and Short Notes and Review Papers 1993, 32, 280-282; (b) R. S. Ruoff, D. C. Lorents, B. Chan, R. Malhotra, S. Subramoney, Science 1993, 259, 346-348.
10. (a) G. G. Tibbetts, D. W. Gorkiewicz, R. L. Alig, Carbon 1993, 31, 809-814; (b) R. Sen, A. Govindaraj, C. N. R. Rao, Chemistry of Materials 1997, 9, 2078-2081.
11. M. Daenen, R. de Fouw, B. Hamers, P. Janssen, K. Schouteden, M. Veld, Eindhoven University of Technology 2003, 1–35.
12. (a) V. Popov, P. Lambin, Carbon nanotubes: from basic research to nanotechnology, Springer Verlag, 2006; (b) S. Niyogi, M. A. Hamon, H. Hu, B. Zhao, P. Bhowmik, R. Sen, M. E. Itkis, R. C. Haddon, Accounts of Chemical Research 2002, 35, 1105-1113.
13. (a) A. Hirsch, Angewandte Chemie International Edition 2002, 41, 1853-1859; (b) D. Britz, A. Khlobystov, Chemical Society Reviews 2006, 35, 637-659.
14. R. Haddon, Accounts of Chemical Research 1988, 21, 243-249.
15. Z. Chen, W. Thiel, A. Hirsch, ChemPhysChem 2003, 4, 93-97.
16. Y. Sun, K. Fu, Y. Lin, W. Huang, Acc. Chem. Res 2002, 35, 1096-1104.
17. G. Zheng, Z. Wang, S. Irle, K. Morokuma, J. Am. Chem. Soc 2006, 128, 15117-15126.
18. (a) J. Li, G. Jia, Y. Zhang, Y. Chen, Chem. Mater 2006, 18, 3579-3584; (b) Y. Miyata, T. Kawai, Y. Miyamoto, K. Yanagi, Y. Maniwa, H. Kataura, physica status solidi (b) 2007, 244, 4035-4039.
19. G. Sumanasekera, B. Pradhan, H. Romero, K. Adu, P. Eklund, Physical Review

Letters 2002, 89, 166801.

20. H. Li, B. Zhou, Y. Lin, L. Gu, W. Wang, K. Fernando, S. Kumar, L. Allard, Y. Sun, J. Am. Chem. Soc 2004, 126, 1014-1015.
21. X. Wang, Y. Liu, W. Qiu, D. Zhu, Journal of Materials Chemistry 2002, 12, 1636-1639.
22. M. Islam, E. Rojas, D. Bergey, A. Johnson, A. Yodh, Nano Letters 2003, 3, 269-273.
23. T. Fukushima, T. Aida, Chemistry-A European Journal 2007, 13, 5048-5058.
24. E. Dujardin, T. Ebbesen, H. Hiura, K. Tanigaki, Science 1994, 265, 1850.
25. P. M. Ajayan, S. Iijima, Nature 1993, 361, 333-334.
26. A. Chu, J. Cook, R. Heesom, J. Hutchison, M. Green, J. Sloan, Chem. Mater 1996, 8, 2751-2754.
27. S. Tsang, Y. Chen, P. Harris, M. Green, 1994.
28. (a) A. Osorio, I. Silveira, V. Bueno, C. Bergmann, Applied Surface Science 2008, 255, 2485-2489; bH. Yu, Y. Jin, F. Peng, H. Wang, J. Yang, 2008; cY. Wang, Z. Iqbal, S. Mitra, J. Am. Chem. Soc 2006, 128, 95-99.
29. (a) J. Liu, A. Rinzler, H. Dai, J. Hafner, R. Bradley, P. Boul, A. Lu, T. Iverson, K. Shelimov, C. Huffman, Science 1998, 280, 1253; (b) J. Chen, M. Hamon, H. Hu, Y. Chen, A. Rao, P. Eklund, R. Haddon, Science 1998, 282, 95.
30. J. Stephenson, J. Hudson, A. Leonard, B. Price, J. Tour, Chem. Mater 2007, 19, 3491-3498.
31. L. Valentini, D. Puglia, I. Armentano, J. Kenny, Chemical Physics Letters 2005, 403, 385-389.
32. S. Pekker, J. Salvetat, E. Jakab, J. Bonard, L. Forro, J. Phys. Chem. B 2001, 105, 7938-7943.
33. X. Lu, Q. Yuan, Q. Zhang, Org. Lett 2003, 5, 3527-3530.
34. Y. Chen, R. Haddon, S. Fang, A. Rao, P. Eklund, W. Lee, E. Dickey, E. Grulke, J. Pendergrass, A. Chavan, J. Mater. Res 1998, 13, 2423–2431.
35. M. Holzinger, J. Abraham, P. Whelan, R. Graupner, L. Ley, F. Hennrich, M. Kappes, A. Hirsch, J. Am. Chem. Soc 2003, 125, 8566-8580.
36. X. Lu, F. Tian, N. Wang, Q. Zhang, Org. Lett 2002, 4, 4313-4315.
37. M. Holzinger, O. Vostrowsky, A. Hirsch, F. Hennrich, M. Kappes, R. Weiss, F. Jellen, Angewandte Chemie International Edition 2001, 40, 4002-4005.
38. J. L. Bahr, J. Yang, D. V. Kosynkin, M. J. Bronikowski, R. E. Smalley, J. M. Tour, Journal of the American Chemical Society 2001, 123, 6536-6542.
39. M. O'connell, S. Bachilo, C. Huffman, V. Moore, M. Strano, E. Haroz, K. Rialon, P. Boul, W. Noon, C. Kittrell, Science 2002, 297, 593.
40. L. Van Hove, Physical Review 1954, 95, 249-262.
41. A. Hartschuh, H. Pedrosa, L. Novotny, T. Krauss, Science 2003, 301, 1354.

42. M. S. Strano, C. A. Dyke, M. L. Usrey, P. W. Barone, M. J. Allen, H. Shan, C. Kittrell, R. H. Hauge, J. M. Tour, R. E. Smalley, Science 2003, 301, 1519-1522.

43. (a) J. Lu, Physical Review Letters 1997, 79, 1297-1300; (b) A. Garg, J. Han, S. Sinnott, Physical Review Letters 1998, 81, 2260-2263.

44. J. Lu, J. Han, Quantum-Based Electronic Devices and Systems 1998, 101–123.

45. E. Frackowiak, K. Metenier, V. Bertagna, F. Beguin, Applied Physics Letters 2000, 77, 2421-2423.

46. G. Arabale, D. Wagh, M. Kulkarni, I. Mulla, S. Vernekar, K. Vijayamohanan, A. Rao, Chemical Physics Letters 2003, 376, 207-213.

47. S. Chou, J. Wang, S. Chew, H. Liu, S. Dou, Electrochemistry Communications 2008, 10, 1724-1727.

48. E. Frackowiak, V. Khomenko, K. Jurewicz, K. Lota, F. Béguin, Journal of Power Sources 2006, 153, 413-418.

49. (a) E. V. Barrera, JOM 2000, 52, 38-42; (b) C. Park, Z. Ounaies, K. Watson, R. Crooks, J. Smith, Chemical Physics Letters 2002, 364, 303-308.

50. M. Meyyappan, Carbon nanotubes: science and applications, CRC, 2005.

51. K. Kostarelos, L. Lacerda, G. Pastorin, W. Wu, S. Wieckowski, J. Luangsivilay, S. Godefroy, D. Pantarotto, J. Briand, S. Muller, Nature Nanotechnology 2007, 2, 108-113.

52. Q. Liu, B. Chen, Q. Wang, X. Shi, Z. Xiao, J. Lin, X. Fang, Nano Lett 2009, 9, 1007-1010.

53. S. Hampel, D. Kunze, D. Haase, K. Krämer, M. Rauschenbach, M. Ritschel, A. Leonhardt, J. Thomas, S. Oswald, V. Hoffmann, Nanomedicine 2008, 3, 175-182.

54. Q. Lu, J. Moore, G. Huang, A. Mount, A. Rao, L. Larcom, P. Ke, Nano Lett 2004, 4, 2473-2477.

55. V. Lovat, D. Pantarotto, L. Lagostena, B. Cacciari, M. Grandolfo, M. Righi, G. Spalluto, M. Prato, L. Ballerini, Nano Lett 2005, 5, 1107-1110.

56. (a) P. Cherukuri, S. Bachilo, S. Litovsky, R. Weisman, J. Am. Chem. Soc 2004, 126, 15638-15639; (b) P. Barone, R. Parker, M. Strano, Anal. Chem 2005, 77, 7556-7562; (c) N. Kam, M. O'Connell, J. Wisdom, H. Dai, Proceedings of the National Academy of Sciences of the United States of America 2005, 102, 11600.

PART A

| Energy Storage |

CHAPTER 2

Synthesis of nanostructures of carbon allotropes including carbon nanotubes and their supercapacitor applications.

Which carbon allotrope is best for supercapacitor applications? This chapter tries to provide answer to this question. Various nanostructures of carbon such as carbon beads, nanotubes were prepared by CVD method varying the metal-hydrocarbon ratio along with temperature. These nanostructures were characterized by SEM, IR, and XRD to follow their structural changes. Their supercapacitor performance was evaluated by cyclic voltammetry and impedance spectroscopy. Carbon nanotubes seems to provide better energy storage owing to their unique structure.

2.1 Introduction

Carbon is an unique element which has the ability to exist in different physical forms that exhibit altogether different properties. This uniqueness arises from the many possible configurations of electronic states of a carbon atom resulting in different hybridizations of atomic orbitals thus making it possible to exist in different bonding states. Three possible hybridizations occur in carbon: *sp, sp^2 and sp^3*, as compared to other group IV elements such as Si and Ge which exhibit primarily sp^3 hybridization [1]. The various bonding states show certain structural arrangements, so that *sp* bonding gives rise to chain structures, sp^2 bonding to planar structures and sp^3 boning to tetrahedral structures. More importantly, these structures exhibit different physical properties.

This chapter discusses the synthesis of different forms of carbon such as mesophase spheres or beads, bamboo like structures and carbon nanotubes, using CVD method by varying the metal-hydrocarbon ratio along with temperature. These nanostructures were characterized by SEM, IR, and XRD to follow their structural patterns. The electrochemical properties of these nanostructures were studied by cyclic voltammetry and impedance spectroscopy to explore their possible applications in supercapacitor devices. The power and energy storage capability of a supercapacitor is closely connected to the physical and chemical characteristics of different forms of carbon and further improvements in the performance can be achieved by manipulating the structural properties of carbon [2]. Among different forms of carbon here, CNTs show better energy storage owing their unique structure.

2.2 Experimental

2.2.1 Synthesis of carbon nanostructures

The different carbon nanostructures were prepared by CVD method. The CVD apparatus was home made and consisted of two-stage furnace system fitted with quartz tube (33 mm OD). The first stage heater was maintained at the temperature 150 - 200 °C to vaporize the metal-hydrocarbon mixture. The second stage furnace was maintained at 675 - 1000 °C to decompose the incoming hydrocarbon vapor to form different carbon structures. The gas used was argon with 10% hydrogen (AR grade). The nanostructures were grown by injecting a 0.01 g/ml solution of ferrocene (Aldrich) in xylene (Aldrich) into the first stage heater where it gets vaporized and this vapor was carried into the second stage heater by carrier gases where it gets decomposed at 700 - 1000 °C to form black deposits on the substrates (Si wafer) and also on the quartz tube walls. The ferrocene to xylene ratio was varied along with temperature to get CNTs and mesophase spheres.

2.2.2 Purification

The lumps CNTs and mesophase spheres obtained on the substrates were first sonicated in toluene to remove fullerenes and undecomposed metal-hydrocarbon impurities [3]. Further purification was done by acid treatment followed by air-oxidation.

The samples were refluxed in 3:1 HNO_3/H_2SO_4 mixture at 120 °C for 6 h to remove the metal impurities. The oxidized samples were diluted to 250 ml by deionized water and filtered thorough PTFE membrane (47 mm, 0.2 μ). the samples were washed with 10 mM NaOH and again by deionized water to make the pH neutral. The samples were dried in an oven at 110 °C and then heated in air at 300 -350 °C to remove the amorphous carbon impurities.

2.2.3 Characterization

The surface chemical compositions of the samples were determined by FTIR in combination with diffuse reflectance mode (DRIFT) on a Perkin-Elmer model. The samples were dispersed in isopropanol (Aldrich) by bath sonication and a drop of this solution was put on Si wafer and the solvent was evaporated under IR lamp.

The morphology and shape of various samples were observed scanning electron microscopy (SEM) on a Leica stereoscan 440 model using an accelerated voltage of 20 kV. The surface of the samples were typically coated with a thin film of gold (ca. 50 -200 Å thick) for SEM studies, to facilitate charge dissipation.

The X-ray diffraction (XRD) analysis was done by using Philips model PW 1830 with Cu Kα (λ = 1.54179 Å) radiation source. The 2 θ range for all the samples was 0 - 80° with a step of 0.02°. The corresponding *d*-spacing was calculated by using Bragg's equation, $n\lambda = 2d \sin\theta$, where n is the order of diffraction, λ is the wavelength of x-rays used, and θ is the diffraction angle. The corresponding crystallite size was calculated by using Scherrer's formula: $L = (K\lambda/\beta \cos\theta)$, where K is 0.9 and β is the half-maximum line width in radians.

The electrochemical measurements were carried out in a three electrode assembly consisting of Ag/AgCl as a reference electrode, platinum as a counter electrode and carbon nanostructures pasted on glassy carbon electrode (GCE) surface as working electrode. The measurements were carried out in 0.1 M H_2SO_4 using a computer controlled potentiostat/galvanostat (Autolab PG 30 with GPES) and impedance analyzer (with FRA software). Impedance measurements were carried out by using an ac signal of 10 mV amplitude over the frequency range 10 mHz to 100 kHz.

2.3 Results and Discussion

2.3.1 Growth Conditions

During the growth of carbon nanostructres ferrocene acts as the nucleation initiator and xylene as the carbon source. The appearance of carbon nano and micro-particles gradually changed with the increase in the ferrocene to xylene ratio. Table 2-4 summarizes the effect of temperature and metal-hydrocarbon ratio on the growth different forms of carbon. The growth of MWCNTs was observed with higher wt.% of metal catalyst. The optimum temperature for the growth of MWCNTs was found to be 720 °C. The other forms such as beads, mesophase spheres, bamboo like structures were observed at different temperatures and lower metal catalyst concentration.

Table 2-4. Growth conditions for the synthesis of different carbon nanostructres. Reaction time was 1.5 min. for all the samples. Gas flow rate was 900 ml/min.

Sample No	Temp. (°C)	Ferrocene wt% in xylene	Product appearance
A	800	1	Carbon beads with thin graphitic shells
B	900	1	Nanotubules with round nodules at the ends
C	900	2	Carbon beads with thick graphitic shell
D	850	2	Carbon beads with thick graphitic shell
E	720	9.6	Long carbon micro fibers with bamboo like shape
F	950	1	Mesophase spheres with graphite shell along with CNTs
G	700	1	Polydispersed carbon beads with filaments
H	720	1	MWCNTs
I	720	9.6	MWCNTs
J	760	9.6	Monodispersed carbon beads
K	760	9.6	Monodispersed carbon beads

It is believed that during the decomposition of hydrocarbon vapor in presence of metal catalyst, bead-like structures are formed, initially as a small non-graphitic amorphous carbon sphere with a diameter around 250 nm. This sphere acts as nucleating center and grows further in various shapes. Graphite shell either forms a thin layer above these spheres or it grows so thick that it coalesces in to a train of interconnected carbon beads [4]. The hydrocarbon vapor activated by metal particles initially forms amorphous carbon which grows further into quasi-spherical shape with embedded metal particles. Graphitic shells grow around these spheres initially with open edges and gradually eliminates the dangling bonds to reduce the surface tension to form carbon spheres.

2.3.2 SEM analysis

The morphological and structural features were studied by SEM analysis. Figure 2-1 shows the various forms of carbon obtained by the growth conditions as described in Table 2-1.

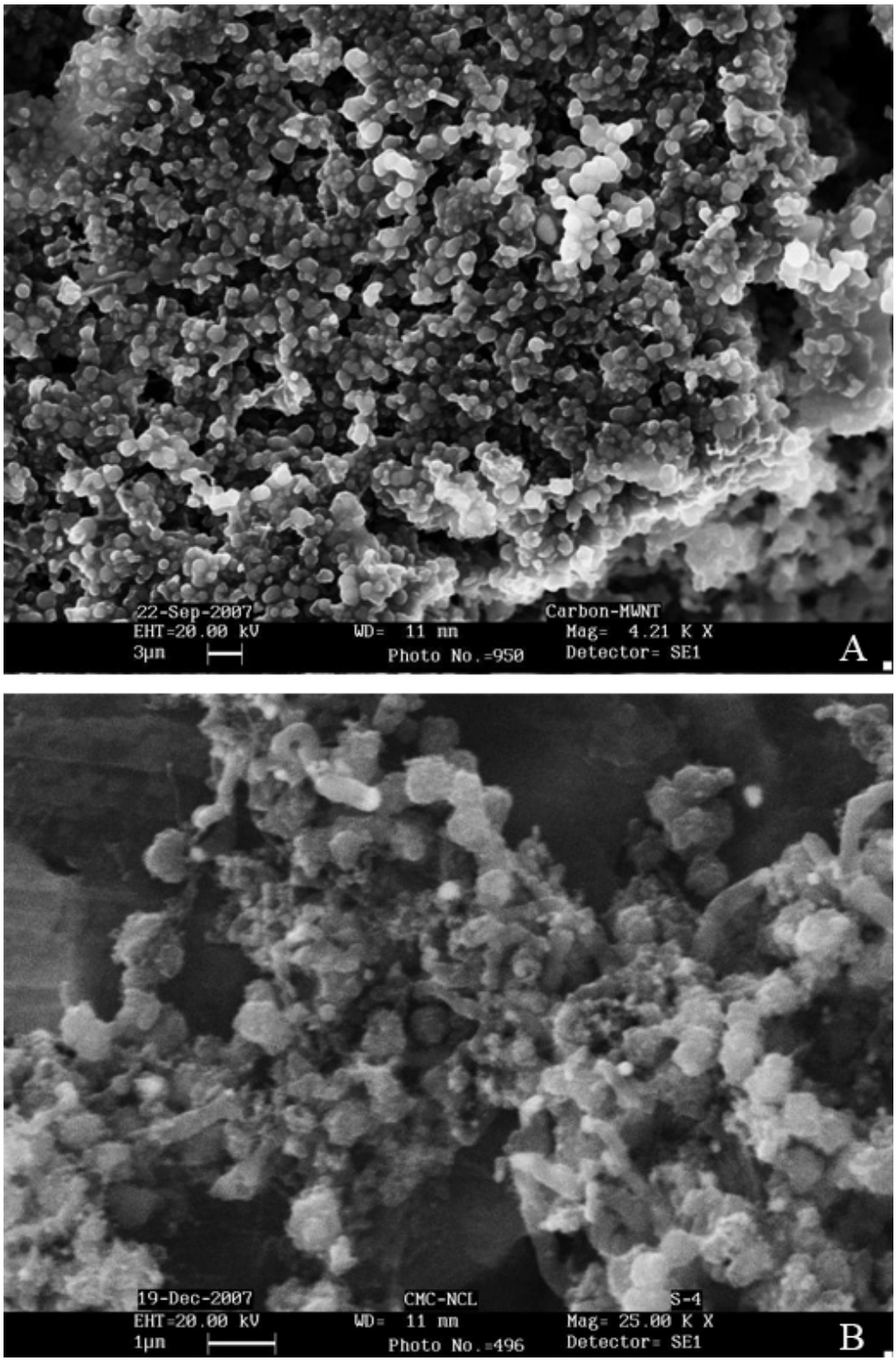
22-Sep-2007
EHT=20.00 kV
3µm
WD= 11 mm
Photo No.=950
Carbon-MWNT
Mag= 4.21 K X
Detector= SE1
A
19-Dec-2007
EHT=20.00 kV
1µm
WD= 11 mm
Photo No.=496
CMC-NCL
Mag= 25.00 K X
Detector= SE1
S-4
B

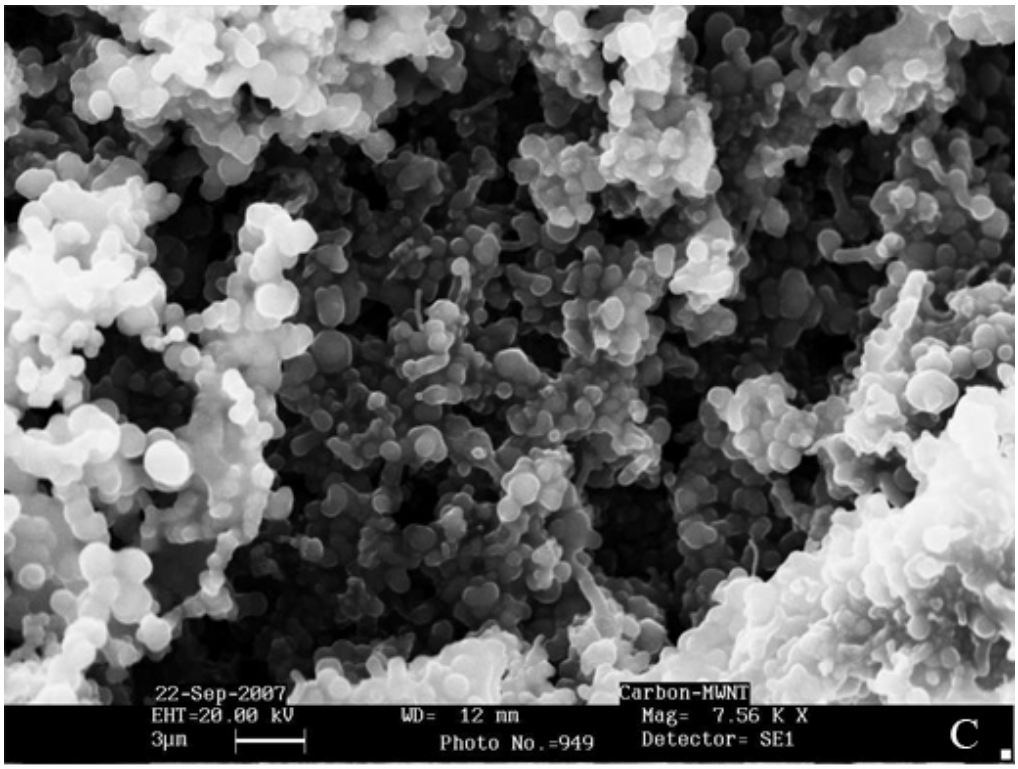
22-Sep-2007
EHT=20.00 kV
3µm
WD= 12 mm
Photo No.=949
Carbon-MWNT
Mag= 7.56 K X
Detector= SE1
C

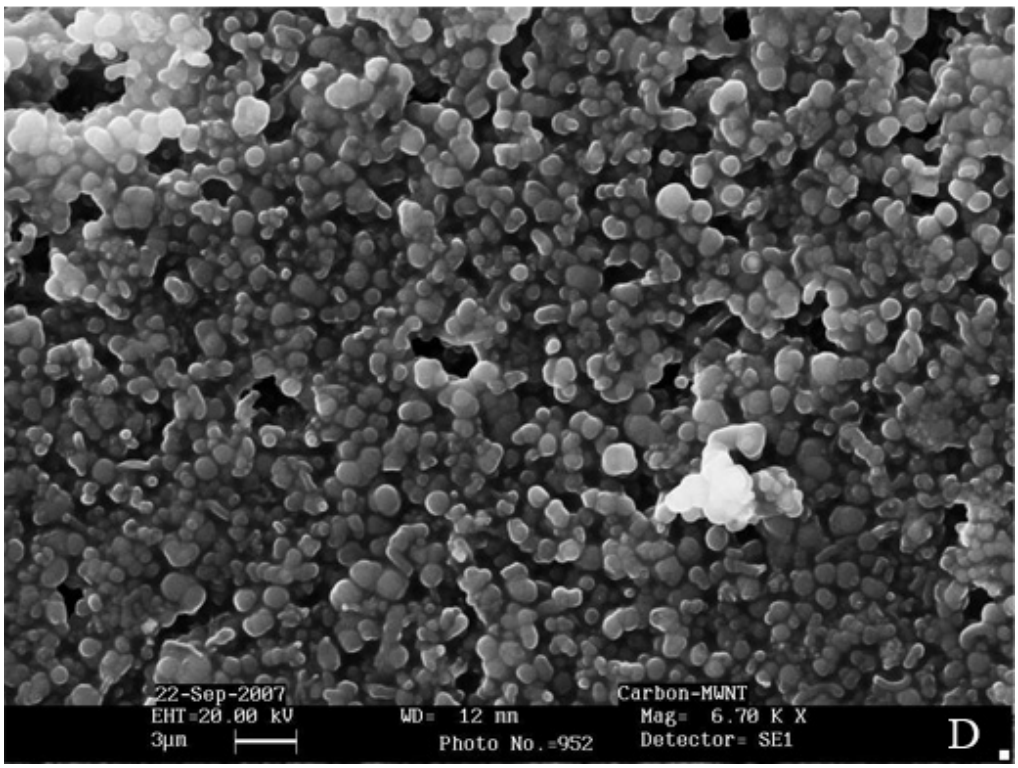
22-Sep-2007
EHT=20.00 kV
3µm
WD= 12 mm
Photo No.=952
Carbon-MWNT
Mag= 6.70 K X
Detector= SE1
D

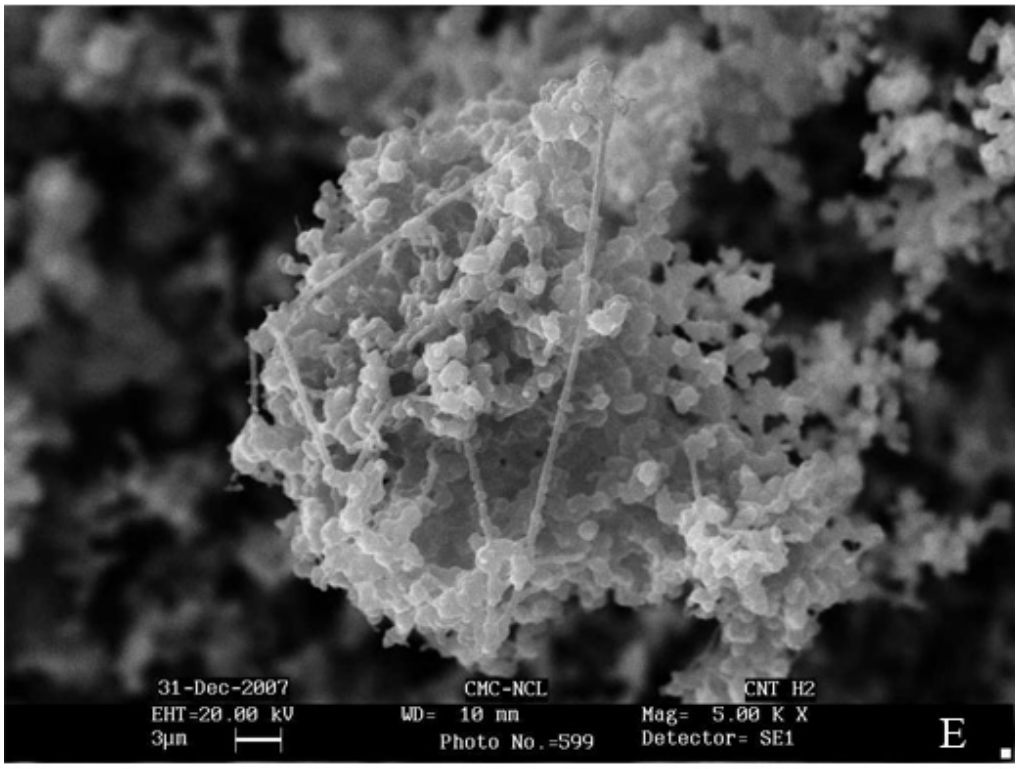
31-Dec-2007
CMC-NCL
CNT H2
EHT=20.00 kV
WD= 10 mm
Mag= 5.00 K X
3µm
Photo No.=599
Detector= SE1
E

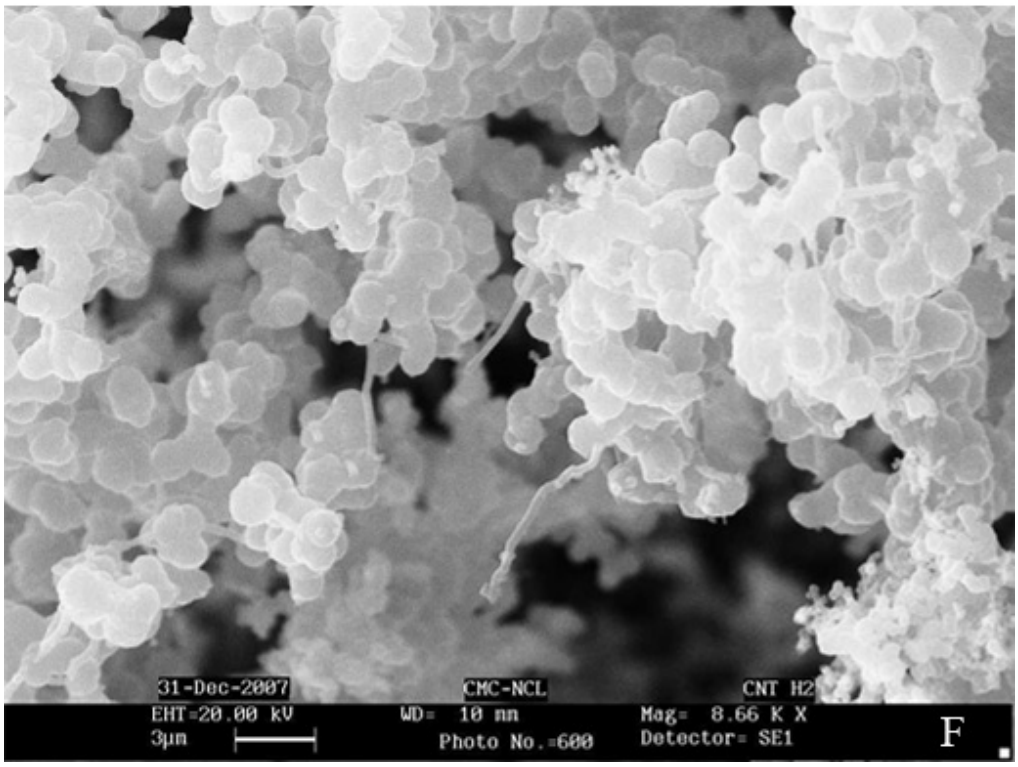
31-Dec-2007
CMC-NCL
CNT H2
EHT=20.00 kV
WD= 10 mm
Mag= 8.66 K X
3µm
Photo No.=600
Detector= SE1
F

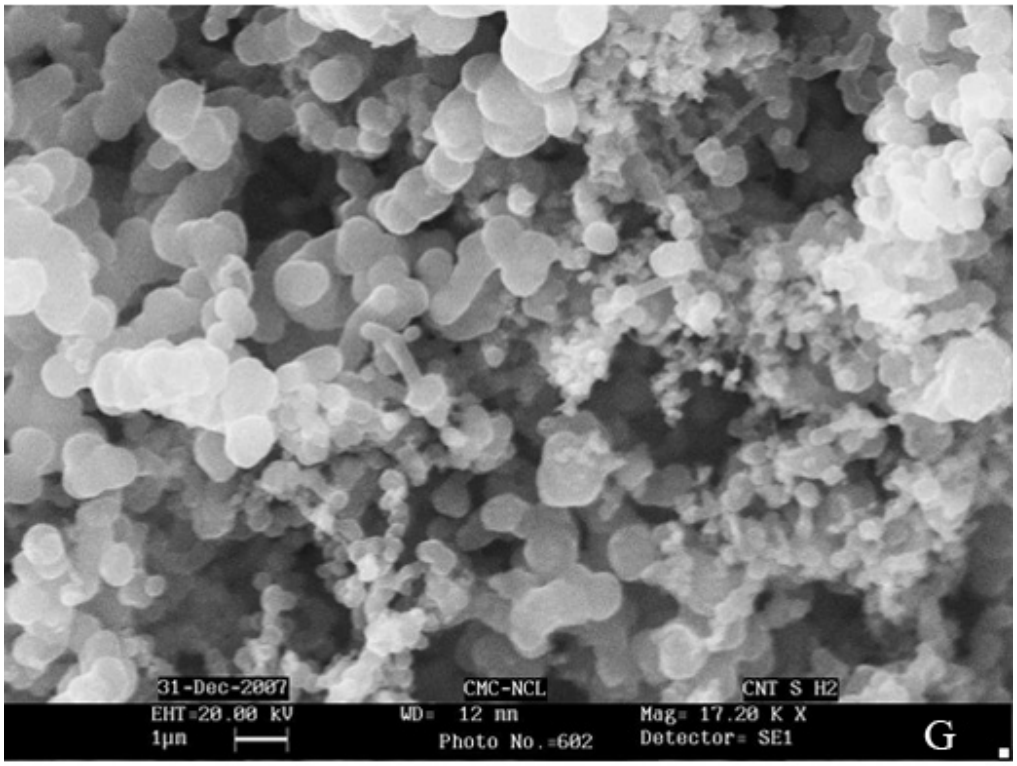
31-Dec-2007
CMC-NCL
CNT S H2
EHT=20.00 kV
WD= 12 nn
Mag= 17.20 K X
1µn
Photo No.=602
Detector= SE1
G

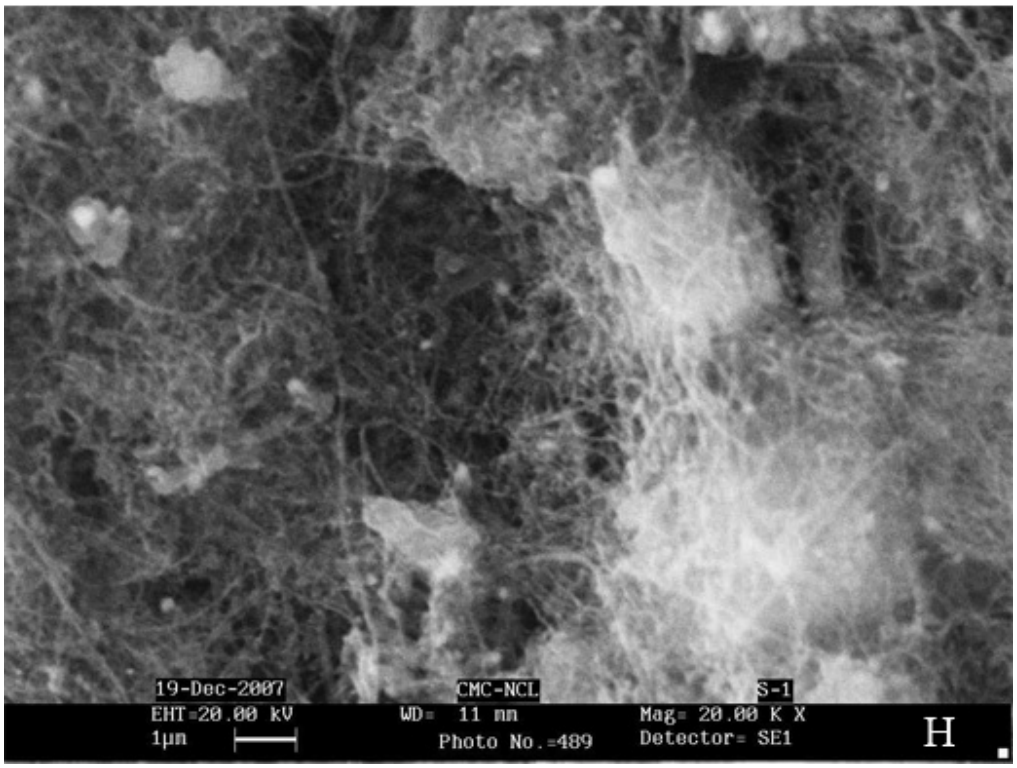
19-Dec-2007
CMC-NCL
S-1
EHT=20.00 kV
WD= 11 nn
Mag= 20.00 K X
1µn
Photo No.=489
Detector= SE1
H

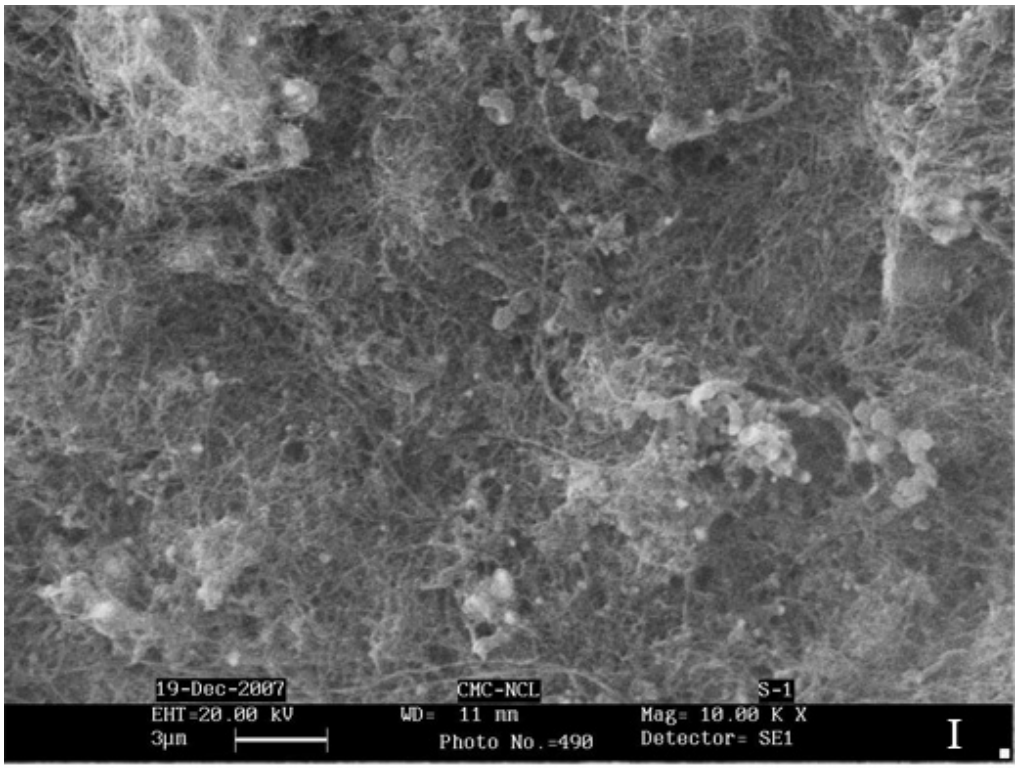
19-Dec-2007
CMC-NCL
S-1
EHT=20.00 kV
WD= 11 mm
Mag= 10.00 K X
3µm
Photo No.=490
Detector= SE1
I

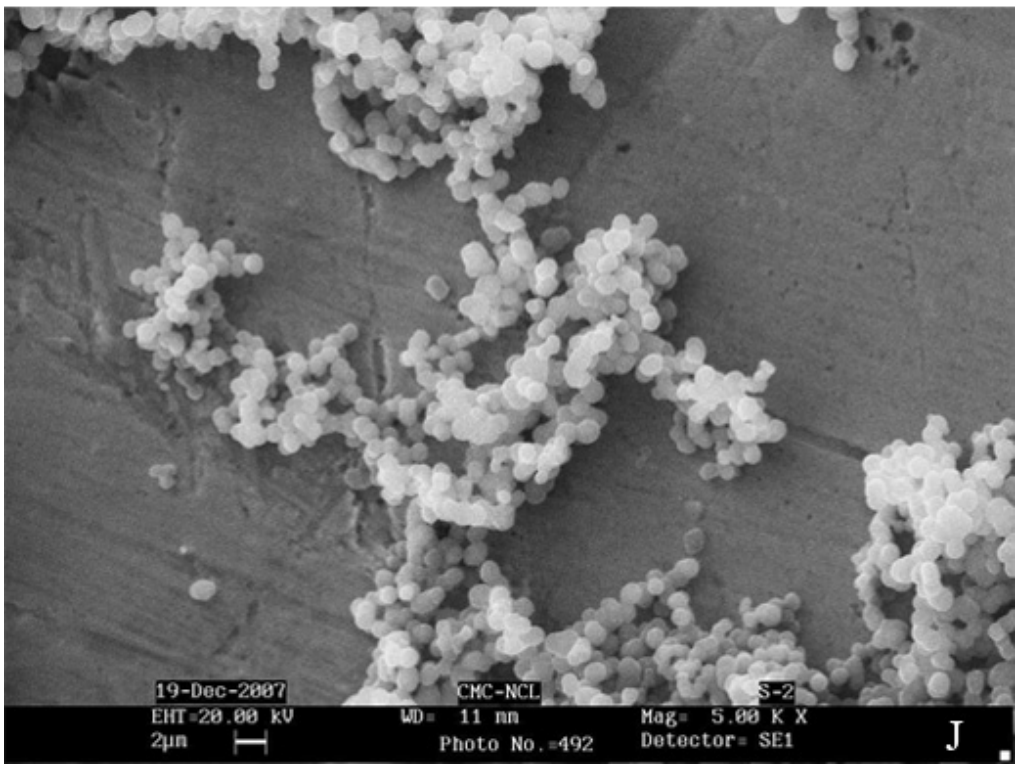
19-Dec-2007
CMC-NCL
S-2
EHT=20.00 kV
WD= 11 mm
Mag= 5.00 K X
2µm
Photo No.=492
Detector= SE1
J

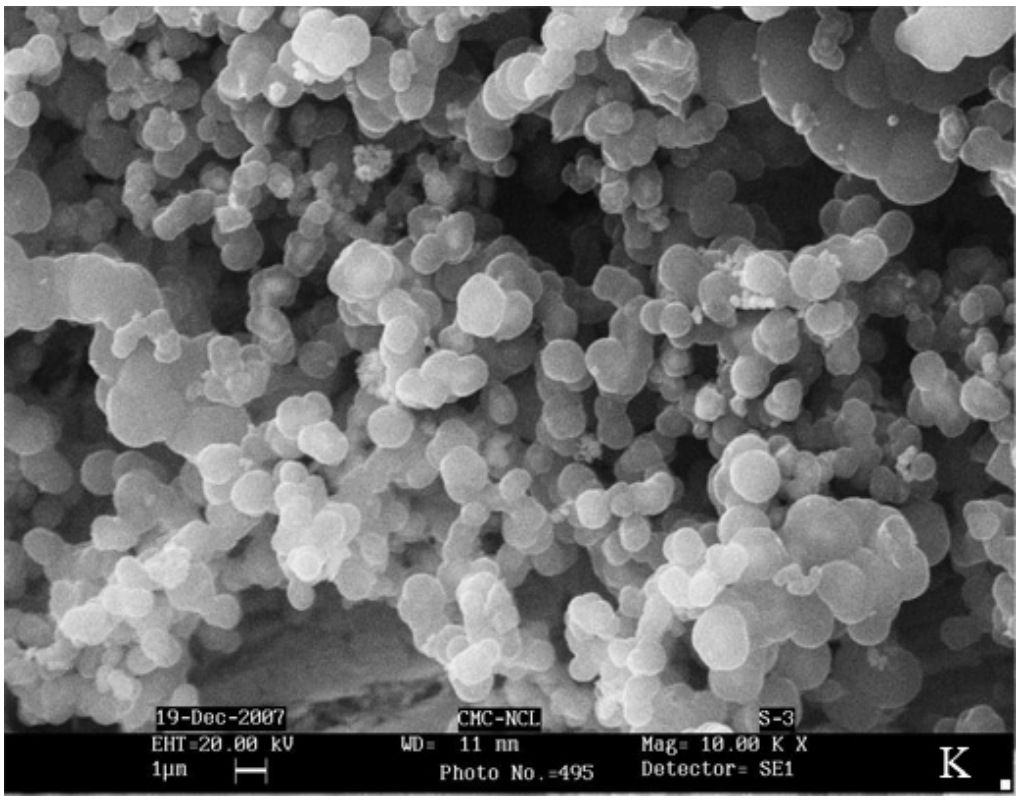

Figure 2-1. SEM images of different forms of carbon obtained by changing metal-hydrocarbon ratio along with temperature as described in Table 2-1. The labels at the right corners of every figure (A, B, C, D, E, F, G, H and K) correspond to the sample no. given in the first column of the Table 2-1.

The formation of MWCNTs occurs with higher metal catalyst concentrations at temperature 720 °C. The open edges of the unclosed graphitic layers in carbon beads are expected to play key role in their microstructures. The electrochemical measurements carried for all these samples showed (values not mentioned here) that there is a marginal difference in the capacitance values among the carbon spheres with sample J- monodispersed carbon beads; showing the highest value. The three samples (E- bamboo like structures, H- MWCNTs and J- monodispersed carbon beads) represented the best difference in the capacitance values. The rest of the discussion in this chapter pertains to these three samples.

2.3.3 FTIR (DRIFT) analysis

The surface chemical composition of the samples E, H and J was followed by FTIR study. Figure 2-2 shows the FTIR spectra of these three samples. In case of MWCNT sample, the acid treatment created a number of functional groups such as α-diketon, ketone, phenolic, carboxylic, lactone, of which carboxylic groups are dominant. The bands around 3400 cm^{-1} can be assigned to the O-H stretching vibrations in alcohols. The peaks at 1748 and 2356 cm^{-1} are assigned to the carboxylic groups [5]. The peak at 1056 cm^{-1} can assigned to C-OH stretching mode. The peaks at 2950, 2920, 2850, 1460, and 1335 cm^{-1} can be assigned to the aliphatic C-H stretching [5]. The peaks between 1300 - 1000

cm^{-1} can be assigned to stretching vibrations of C-O single bonds in the ether, epoxide and phenolic structures. The peak at 1500 cm^{-1} is due to the double bond vibrations. Below 800 cm^{-1}, bands can be assigned to the out of plane deformation vibrations of O-H groups present at the edges of the aromatic planes [5].

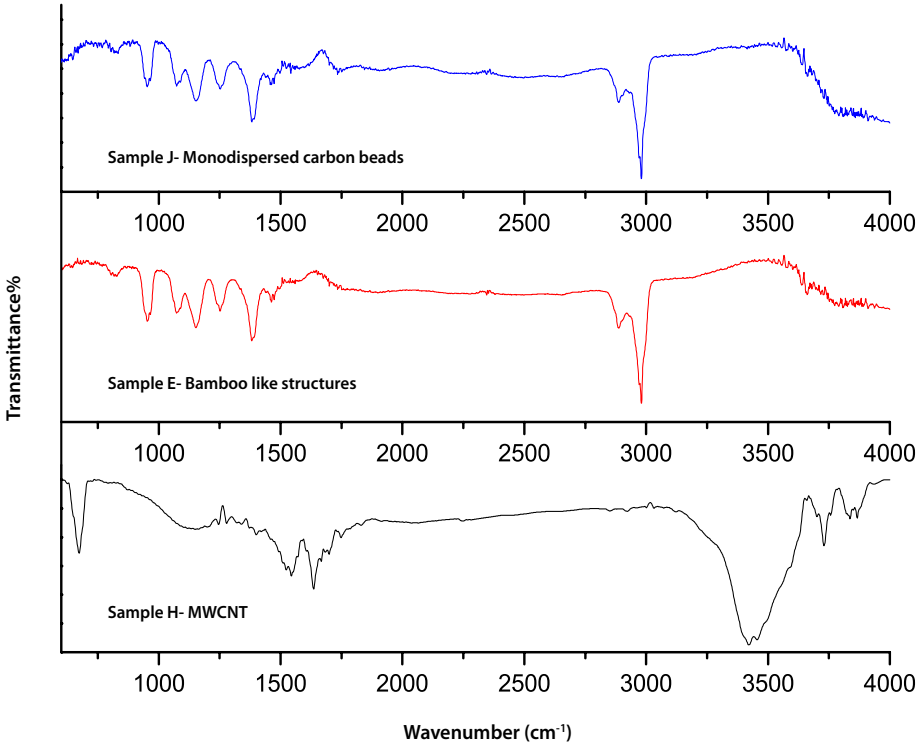

Figure 2-2. FTIR (DRIFT) spectra of MWCNTs (sample H), bamboo like structures (sample E) and monodispersed carbon beads (sample J).

The FTIR spectra of samples E and J show two prominent peaks at 2927 cm^{-1} and 2962 cm^{-1} which correspond to C-H stretching for a sp^3 and sp^2 bonded carbon atom respectively. The peaks at 1730 cm^{-1} corresponding to C=O stretching were absent in both samples. From the peak intensities (2927 and 2962 cm^{-1}), the ratio of sp^3 and sp^2 type carbons were calculated for both the samples. From this ratio and the sum of the peak intensities at 2927 and 2962 cm^{-1}, the percentage of sp^3 carbon atoms present in the samples is calculated to be around 16.23% (sample E) and 17.32 (sample J), and while the percentage of sp^2 carbon atoms was 83.77% (sample E) and 82.68% (sample J).

2.3.4 XRD analysis

The extent of graphitization in turn the crystallinity of the samples was studied by XRD analysis. All the samples show a rather broad peak around 26°. This peak is a characteristic of the 002 graphitic plane [6]. This peak is quite sharp in the MWCNT sample indicating the crystalline nature of nanotubes. The 002 graphitic plane peaks for samples E and J were quite broad and they show less degree of graphitization. Figure 2-3 shows the XRD of the samples E, J, and H.

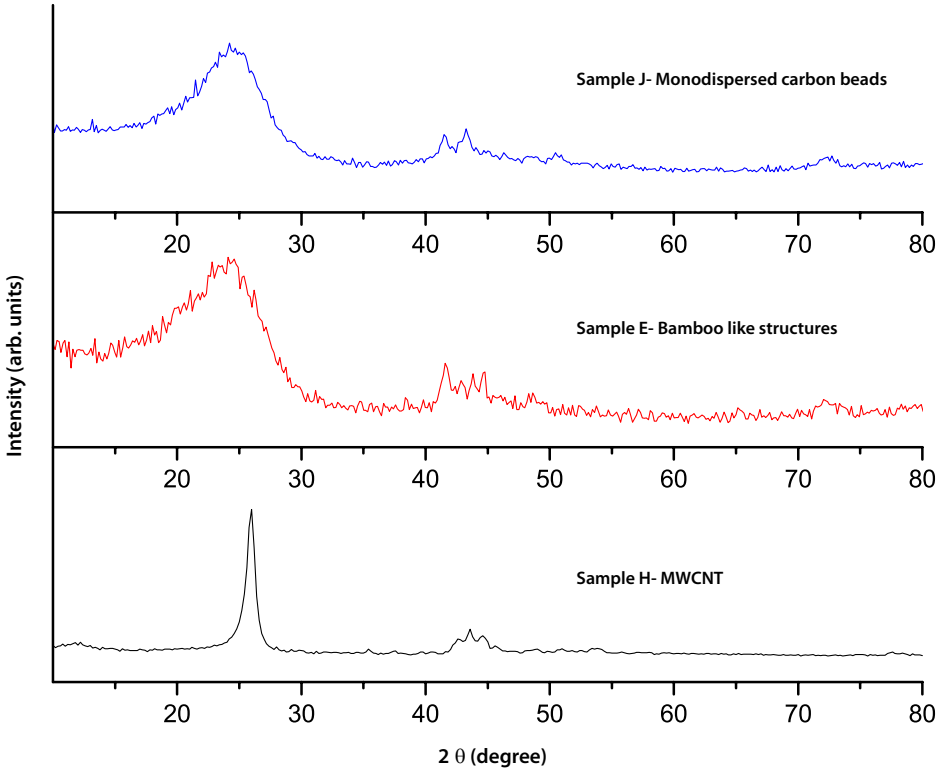

Figure 2-3. XRD of MWCNTs (sample H), bamboo like structures (sample E), and monodispersed carbon (sample J).

In addition to the strong (002) peak, all the samples showed three smaller peaks at 42.44°, 65.11°, and 72.10° positions that correspond to the 100, and 110 planes of graphite.

2.3.5 Cyclic voltammetry studies

Cyclic voltammetry measurements were carried out to study the effect of operational parameters like sweep rate, cycling, etc. on the capacitance of carbon samples.

Figure 2-3 shows the cyclic voltammograms of all the three samples at 10 mV/s scan rate. The peaks observed at 0.25 V (anodic) and around 0.5 V (cathodic) vs . Ag/AgCl are associated with the oxygen-containing surface functionalities such as carboxylic acids present on the surface. These peaks were quite prominent in MWCNTs sample as they contain a number of oxygenated surface functionalities as shown earlier in FTIR study. The pseudocapacitive behavior associated with these surface functional groups diminishes after number of cycling due to the irreversibility of the redox reactions [2].

The double layer capacitance across the interface depends on the accessibility of electrolyte ions to the interiors of carbon samples [2]. The MWCNTs, due to their randomly entangled network, presents a labyrinth for the electrolyte ions. The presence of central core, intertubular spaces behaves like mesoporous network for the electrolyte

ions to travel [7]. This is the reason why MWCNTs showed largest capacitance values among three samples. The gravimetric capacitances of all the samples were calculated in the linear region of the voltammograms where they show ideal double layer capacitive behavior, using the relation $C = Q/V = I\,t/V$, where Q are the charges, I is the current, t is

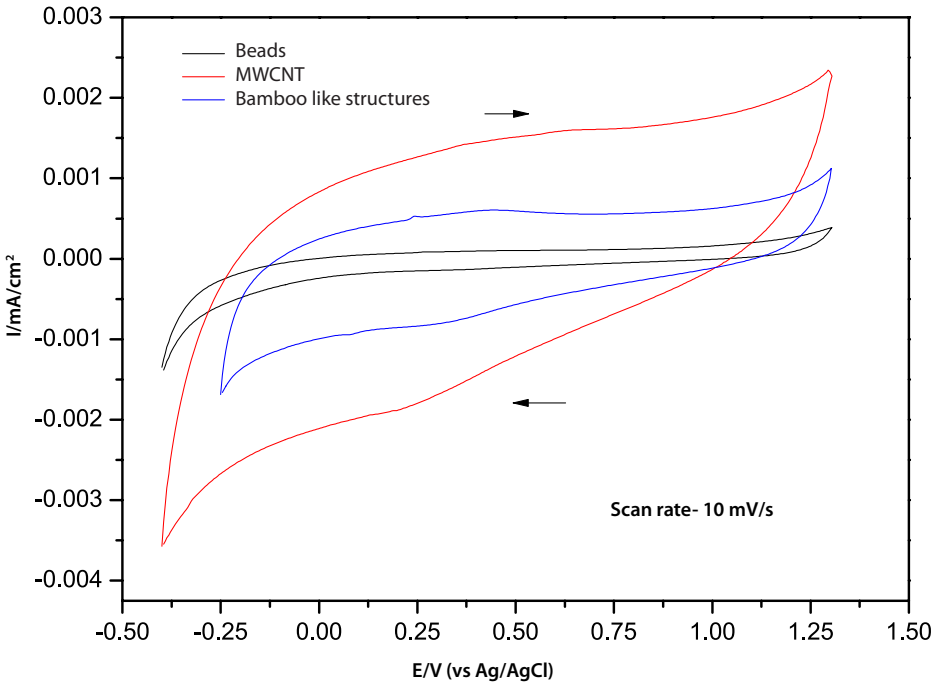

Figure 2-4. Cyclic voltammograms of MWCNTs, carbon beads, and bamboo like structures in 0.1 M H2SO4. The reference electrode was Ag/AgCl. Arrows show the direction of voltammograms.

time and V is the voltage applied. The capacitance values obtained for MWCNTs were in the range of 48-56 F/g while for bamboo like structures and beads, it was in the range of 28-32 F/g and 12-19 F/g respectively.

The carbon beads and bamboo like structures also contain dangling bonds like CNTs because of the presence of unclosed graphitic shells but their concentration is small compared to CNTs.

2.3.6 Impedance analysis

Electrochemical impedance spectroscopy (EIS) is the valuable tool not only to determine the equivalent series resistance but also to study the interfacial and psuedocapacitance of the electrode structure [2]. In this technique an alternating voltage is applied to the electrode interface, the response is measured by the imaginary component, Z", of the impedance which is the capacitance of the electrode given by the equation: $Z'' = 1/2\pi f C$, where f is the frequency.

Figure 2-5 shows the impedance spectra of the three samples (E, H, & J) measured

in 0.1 M H_2SO_4. All the measurements were carried in the frequency range 10 mHz to 100 kHz with an ac amplitude of 10 mV. As it can be seen from the figure, the MWCNTs show

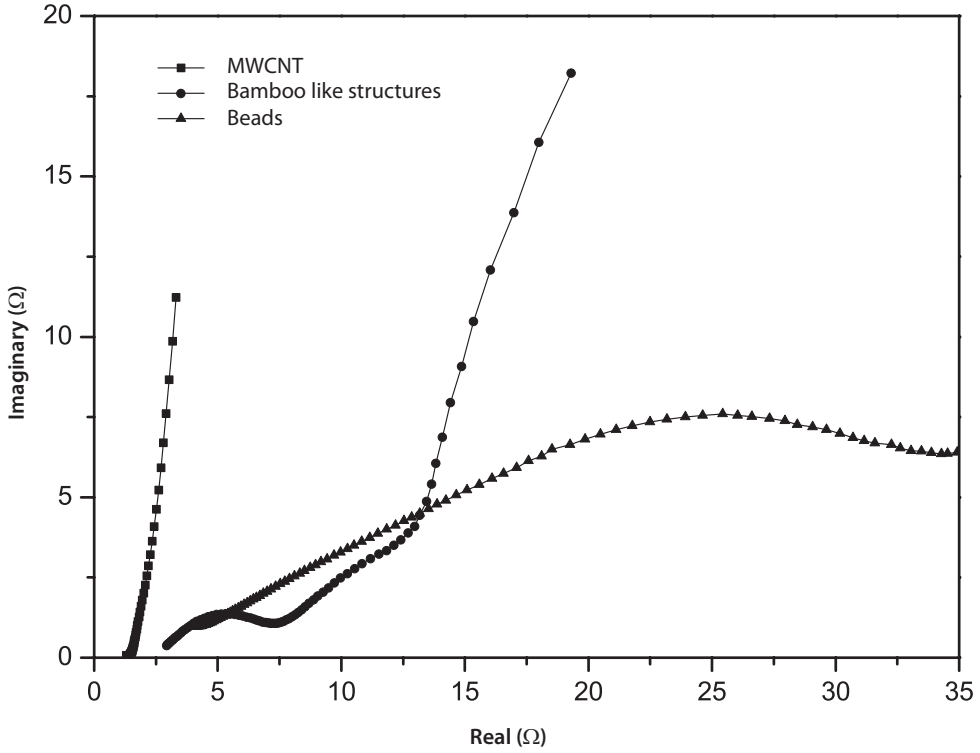

Figure 2-5. Impedance spectra of MWCNT, bamboo like structures, and carbon beads in 0.1 M H_2SO_4. The frequency range was 10 mHz to 100 kHz.

capacitive behavior as it almost goes parallel to the y-axis. The bamboo like structures show a presence of semicircle in the high frequency region, while in the low frequency region, there is a straight line angled at more 45° to the real axis, the behavior can be attributed to the semi-infinite linear diffusion at the porous electrode.

The carbon beads show resistive behavior as compared to MWCNTs and bamboo like structures. The capacitance calculated from the semicircle maxima for each of the sample was 23 F/g (MWCNTs), 11 F/g (bamboo like structures), and 2 F/g (carbon beads). The capacitance values are quite low because of the model dependent nature compared to the values obtained from cyclic voltammetry.

2.4 Conclusions

Different allotropes of carbon including carbon nanotubes, beads, bamboo like structures, have been synthesized using CVD method by varying the metal-hydrocarbon ratio along with growth temperature. The morphology of these nanostructres was observed by SEM. Three representative samples were chosen to understand the relation between structural and electrochemical properties. The MWCNTs due to their unique

structure show largest capacitance values among these allotropes. Thus manipulating the structures of carbon allotropes, it is possible to make high energy storage devices such as supercapacitors.

2.5 References

1. R. Saito, G. Dresselhaus, M. S. Dresselhaus, Knovel, Physical properties of carbon nanotubes, Vol. 4, Imperial college press London, 1998.
2. B. E. Conway, Electrochemical supercapacitors: scientific fundamentals and technological applications, Springer Us, 1999.
3. A. Rinzler, J. Liu, H. Dai, P. Nikolaev, C. Huffman, F. Rodriguez-Macias, P. Boul, A. Lu, D. Heymann, D. Colbert, Applied Physics A: Materials Science & Processing 1998, 67, 29-37.
4. M. Sharon, K. Mukhopadhyay, K. Yase, S. Iijima, Y. Ando, X. Zhao, Carbon 1998, 36, 507-511.
5. J. Zhang, H. Zou, Q. Qing, Y. Yang, Q. Li, Z. Liu, X. Guo, Z. Du, J. Phys. Chem. B 2003, 107, 3712-3718.
6. Y. Saito, T. Yoshikawa, S. Bandow, M. Tomita, T. Hayashi, Physical Review B 1993, 48, 1907-1909.
7. E. Frackowiak, F. Beguin, Carbon 2002, 40, 1775-1787.

CHAPTER 3

Enhanced supercapacitance of multiwalled carbon nanotubes functionalized with hydrous ruthenium oxide.

This chapter reports the pseudocapacitive behavior of multiwalled carbon nanotubes (MWCNTs) functionalized with hydrous ruthenium oxide in 1 M sulfuric acid for supercapacitor applications. The entangled network of nanotubes which forms open mesopores and their chemical stability with a basal geometry makes them suitable for such applications. Oxidative treatment to generate oxygenated functional groups on the tube-ends and along the sidewalls enables facile derivatization by hydrous ruthenium oxide to enhance the inherent capacitance. A specific capacitance of 80 F/g is obtained after ruthenium oxide functionalization, which is significantly greater than that of pristine MWCNTs (30 F/g) in the same medium.

3.1 Introduction

Supercapacitors [1] are energy storage devices, which have attracted considerable interest over the past decade due to their applications in electric vehicles [2] (EVs) and hybrid EV technology. These applications impose rather stringent restrictions on both volumetric/gravimetric power density and RC time that can be accomplished by only specially designed materials. The well known examples include aerogel carbons [3, 4, 5, 6 and 7], conducting polymer based nanocomposites [8, 9, 10 and 11] and activated carbon [12]. For other applications like lightweight electronic fuses, memory back-ups, solar batteries, etc., long life, safety, simplicity of design, cost and the possibility of recharging can be more important. In all the applications listed above, energy storage is achieved across the electrolyte–electrode interface either by Faradaic or non-Faradaic process. Non-Faradaic mechanisms need materials with high specific surface area such as activated carbon, carbon aerogels, etc. since the capacitance predominantly depends on the surface area accessible to the electrolyte ions. On the other hand, Faradaic processes store energy via fast charge (electron) transfer reactions between a solid electrode and the species present in the electrolyte. This basic difference is kept in mind in designing suitable new materials for supercapacitors, irrespective of the nature of applications.

Recently carbon nanotubes [13] have been recognized as a potential electrode material for supercapacitors [14 and 15] because of their unique properties such as mesoporous character, entanglement, chemical stability, low resistivity and the presence of central canal. The central core and the entangled network of CNTs present an open mesoporous structure which not only helps in the transportation of ions but also facilitates the charging of the double layer. Capacitance values ranging from 10 to 35 F/g have been obtained for the carbon nanotubes depending on the microtexture of nanotubes, number of defects, micropore volume and catalyst contamination. Chemical treatment (KOH) for activation has also been carried out to increase the micropore volume to get improved capacitance values [16]. Additional capacitance values up to 170 F/g have been obtained by forming composites of the MWCNTs-conducting polymers such as polypyrrole [17 and 18]. However these materials do not withstand the high cycle life (>100 000) due to the strong propensity of conducting polymers for degradation. More significantly, the degradation aspects may be exacerbated due to the possible electrochemical abuse resulting from possible overcharge and overdischarge during their sustained operation. In this context, transition metal oxides attached on MWCNT are expected to be more useful due to their enhanced stability, provided they are highly conducting.

The supercapacitive behavior of several transition metal oxides such as RuO_2 [1 and 4], IrO_2 [19], NiO_x [20] has already been evaluated. Among these, hydrous ruthenium oxide has been recognized as one of the most promising candidates for electrodes as it can store charges by reversibly accepting and donating protons from an aqueous electrolyte governed by the potential dependent equilibrium as shown in following equation 3.3.

$$RuO_x(OH)_y + \delta H^+ + \delta e^- \rightarrow RuO_x - \delta(OH)_{y+\delta} \qquad 3.3$$

Hydrous ruthenium oxide is a mixed electronic-protonic conductor [21 and 22]. Its electrochemical properties depend on the amount of water incorporated in its structure, and the change of oxidation state (Ru^{4+}/Ru^{3+}) of ruthenium along with this is known to cause the capacitance.

In the present study we report the supercapacitive behavior of ruthenium oxide functionalized multiwalled carbon nanotubes (Ru/MWCNT), for the first time. By using cyclic voltammetry and impedance measurements, we have found that the capacitance of MWCNTs can be increased from 30 to 80 F/g after ruthenium oxide functionalization.

3.2 Experimental

3.2.1 Specimen preparation

The details of the MWCNTs preparation has been discussed elsewhere [23]. These nanotubes were refluxed with 6M HNO3 at 120 °C for 3 h to remove the metal catalyst impurities and generate oxygenated surface functional groups. The oxidized MWCNTs were thoroughly washed with double distilled water (DDW) and dried in an oven at 110 °C.

The oxidized MWCNTs were dispersed in isopropanol and water (1:1 volume) solution by ultrasonic agitation, to which $RuCl_3 \cdot 3H_2O$ was added (1:0.5 MWCNT to Ru wt. ratio) and again ultrasonicated for 1 h. The Ru/MWCNTs mass was filtered and washed thoroughly with DDW to remove the excess chloride ions. The Ru/MWCNT sample was dried in an oven at 110 °C.

3.2.2 Electrode preparation and characterization

The Ru/MWCNTs (3 mg) were dispersed in 10 ml N, N - dimethylformamide (DMF) with the aid of ultrasonic agitation. A drop of this solution was put on the polished surface of glassy carbon electrode (GCE) and dried under IR lamp to evaporate the solvent. A similar procedure was followed to prepare the MWCNT electrode.

All electrochemical measurements were carried in a three-electrode assembly consisting of Ag/AgCl as a reference electrode, Pt foil counter electrode and MWCNT or Ru/MWCNTs pasted on GCE surface as a working electrode in 1 M H_2SO_4 using a computer-controlled potentiostat/galvanostat (Autolab PGSTAT 30 with GPES software) and an impedance analyzer (Autolab PGSTAT 30 with FRA software). Cyclic voltammetry was carried between –1.0 and +0.45 V vs. Ag/AgCl for various scan rates ranging from 1 to 1000 mV/s. Electrochemical impedance measurements were carried out for both MWCNTs and Ru/MWCNTs samples applying an ac signal of 10 mV amplitude over the frequency range 10 mHz to 40 kHz. The surface chemical composition of the samples was determined by FTIR in combination with diffuse reflectance spectroscopy (DRIFTS). Scanning electron microscopy (SEM) studies were performed using Leica Stereoscan 440 model. Thermogravimetric analyses were performed on Perkin–Elmer TGA 7 at a heating rate of 10 °C/min. in an atmosphere of air flowing at 180 ml/min.

3.3 Results and discussion

3.3.1 DRIFT spectra analysis

Figure 3-1 shows the DRIFT spectra of both MWCNTs and Ru/MWCNTs. The immediate distinction between these two spectra is the difference in the peak intensities. The peak intensities of the surface functional groups of MWCNTs are markedly reduced after ruthenium functionalization. The band around 3400 cm^{-1} can be assigned to the O–H stretching vibrations in alcohols [24]. The peaks at 1748 and 2536 cm^{-1} are assigned to the carboxylic groups. The peak at 1056 cm^{-1} can be assigned to C–OH stretching mode. The peaks at 2950, 2920, 2850, 1460, 1335 cm^{-1} can be assigned to the aliphatic C–H stretching. The peaks between 1300 and 1000 cm^{-1} can be assigned to stretching vibrations of C–O single bonds in the ether, epoxide and phenolic structures. The 1500 cm^{-1} can be attributed to the double bond vibrations. Below 800 cm^{-1}, bands can be assigned to the out of plane deformation vibrations of O–H groups present at the edges of the aromatic planes. The carboxylic acid peak intensity is reduced after ruthenium functionalization and thus one can conclude that the –COOH groups are derivatized by RuO_2.

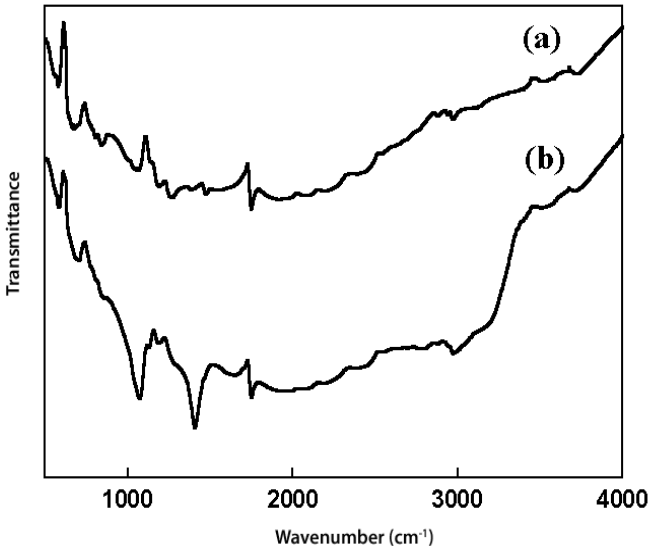

Figure 3-1. DRIFT spectra of: (a) Ru/MWCNT; (b) MWCNT.

3.3.2 Thermogravimetric analysis

Thermogravimetric analysis shows the initial wt. loss around 500 °C for MWCNTs, due to the combustion of carbonaceous fractions[25]. Between 700 and 800 °C MWCNTs undergoes oxidation. For Ru/MWCNTs, the wt. loss around 470 °C is primarily due to the loss of water content from functionalized $RuO_2 \cdot xH_2O$. From the TGA studies, the water

content is estimated as $RuO_2 \cdot 0.5H_2O$.

3.3.3 Scanning electron microscopic studies

Figure 3-2 shows the SEM images of both MWCNTs and Ru/MWCNTs. A randomly entangled network can be seen from the figure. The diameter of MWCNTs is in the range 30–150 Å. The intertubular spaces and central core of CNTs present a

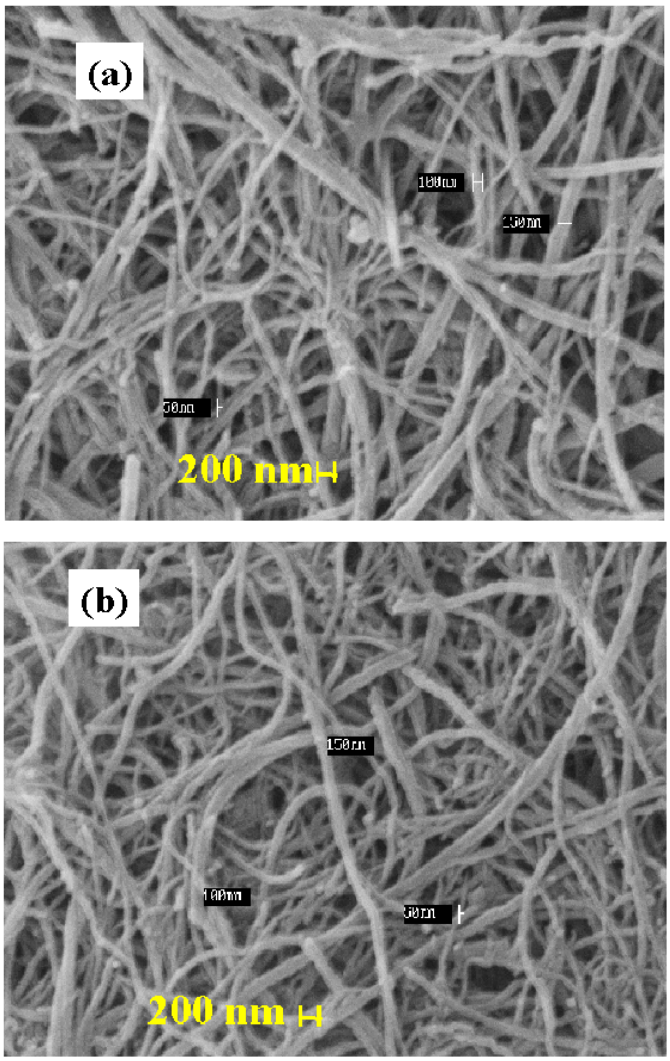

Figure 3-2. Scanning electron microscopic images of: (a) MWCNTs; (b) Ru/MWCNTs.

mesoporous structure which is an important parameter to achieve higher capacitance.

The EDAX results confirmed the deposition of Ru on MWCNTs. The peak around 2.50 kV shows the presence of ruthenium. The ruthenium wt.% deposited on CNTs was 1%.

3.3.4 Cyclic voltammetry studies

Cyclic voltammetry measurements were carried out to characterize the influence of Ru deposition on MWCNTs and also to study the operational parameters like sweep rate, cycling, etc. on the capacitance of Ru/MWCNTs sample.

Figure 3- 3 displays the cyclic voltammograms of MWCNTs in 1M H_2SO_4 at different scan rates. The peaks observed at –0.08 V (anodic) and –0.13 V (cathodic) vs. Ag/AgCl are associated with the oxygen-containing surface functionalities such as carboxylic acids present on the MWCNTs. Another pair of reduction/oxidation waves was observed at the –0.52 and –0.58 V for anodic and cathodic potentials vs. Ag/AgCl respectively. All these peaks reveal the presence of oxygenated functional groups as

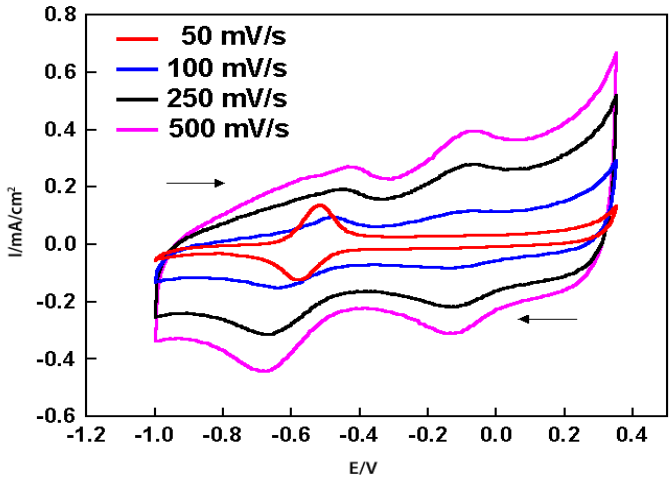

Figure 3-3. Cyclic voltammograms of MWCNT at various scan rates in 1 M H_2SO_4. Arrows indicate the direction of scan.

they show pH dependent behavior. We attributed these peaks to the oxygenated surface functionalities such as quinones, the functional groups that show similar peaks with GCE. The cathodic peak shifts negatively as the scan rate (v) increases whereas the anodic peak shifts positively.

The linear dependency of i_p (peak current) on the $v^{1/2}$ suggests that the MWCNTs film is showing macroelectrode behavior instead of nanoelectrode. This may be due to the high packing density of MWCNTs with average pore size of tens of nm, which is quite smaller than the diffusion layer thickness of the electrolyte leading to the semi-infinte planar diffusion similar to the planar macroelectrode.

The ΔE_p ($\Delta Ep=|E_{pa}-E_{pc}|$, where E_{pa} and E_{pc} are the anodic and cathodic potentials, respectively) value was greater than $0.059/n$ V (where 'n' is the no. of electrons per molecule oxidized or reduced) and increases with v. The pseudocapacitive behavior

associated with these surface functional groups diminishes after continuous cycling due to the irreversibility of the redox reactions. The capacitance value essentially depends on the microtexture of nanotubes, number of defects, micropore volume and the catalyst contamination.

The accumulation of charges in the electrode–electrolyte interface mainly depends on the electrolyte ion accessibility to the sidewalls and central core of the nanotubes. Open tips, the number of defects and the presence of interconnected network enhance the capacitance values. The gravimetric capacitance for MWCNTs was 30 F/g which was measured in the linear region of the voltammogram where the MWCNTs show ideal double-layer capacitive behavior.

Figure 3-4 (a) displays the cyclic voltammogram of Ru deposited MWCNTs. The peaks at 0.11 V (anodic) and 0.07 V (cathodic) potentials vs. Ag/AgCl can be attributed to the ruthenium oxide present on the MWCNTs. The ruthenium wt. deposited on MWCNTs calculated from the peak integration method is 1% that is consistent with the EDAX results. The ruthenium was likely to be deposited as hydrous RuO_2 as the heating temperature was 150 °C, which is quite below the crystallization temperature (300 °C). Disordered form of RuO_2 is supposed to be an essential parameter for improved capacitance.

The peaks that were quite sharp for the first cycle diminished with the number of cycles. A small hump adjacent to the cathodic peak (–0.07 V) was observed which was diminished after 50 times cycling and was emerged into a single cathodic peak. With cycling almost complete diminishing of the anodic peak was observed.

Figure 3-4 (b) shows the cyclic voltammogram of Ru/MWCNTs after 100 cycling. There was no distinct electrochemical couple; the current was virtually independent of the potential applied, indicating the uniform infusion of electrons into a metal band. $RuO_x{\cdot}nH_2O$ undergoes changes in the oxidation states that correspond to Faradaic redox transitions such as Ru^{4+}/Ru^{3+} at the electrode–electrolyte interface.

To determine the number of electroactive cations involved in the redox transitions or rather to evaluate the capacitance, voltammetric charges, q^*, integrated from –1.0 to 0.45 V were used. The specific capacitance was obtained by dividing this quantity by weight of the MWCNT film applied on the working electrode. The specific capacitance obtained for Ru/MWCNTs was 80 F/g, the value greater than the capacitance of MWCNTs alone.

Thus, charge storage in Ru/MWCNTs system involves the contribution from i) charge-transfer across the interface that give rise to redox pseudocapacitance and ii) accumulation of charges across the interface to form double-layer.

The randomly entangled mesoporous network of carbon nanotubes provides the electronic conducting pathways, which allow the diffusion of ions easily to the active surface area of nanosized metal oxide and thus facilitates the Faradaic processes across the interface.

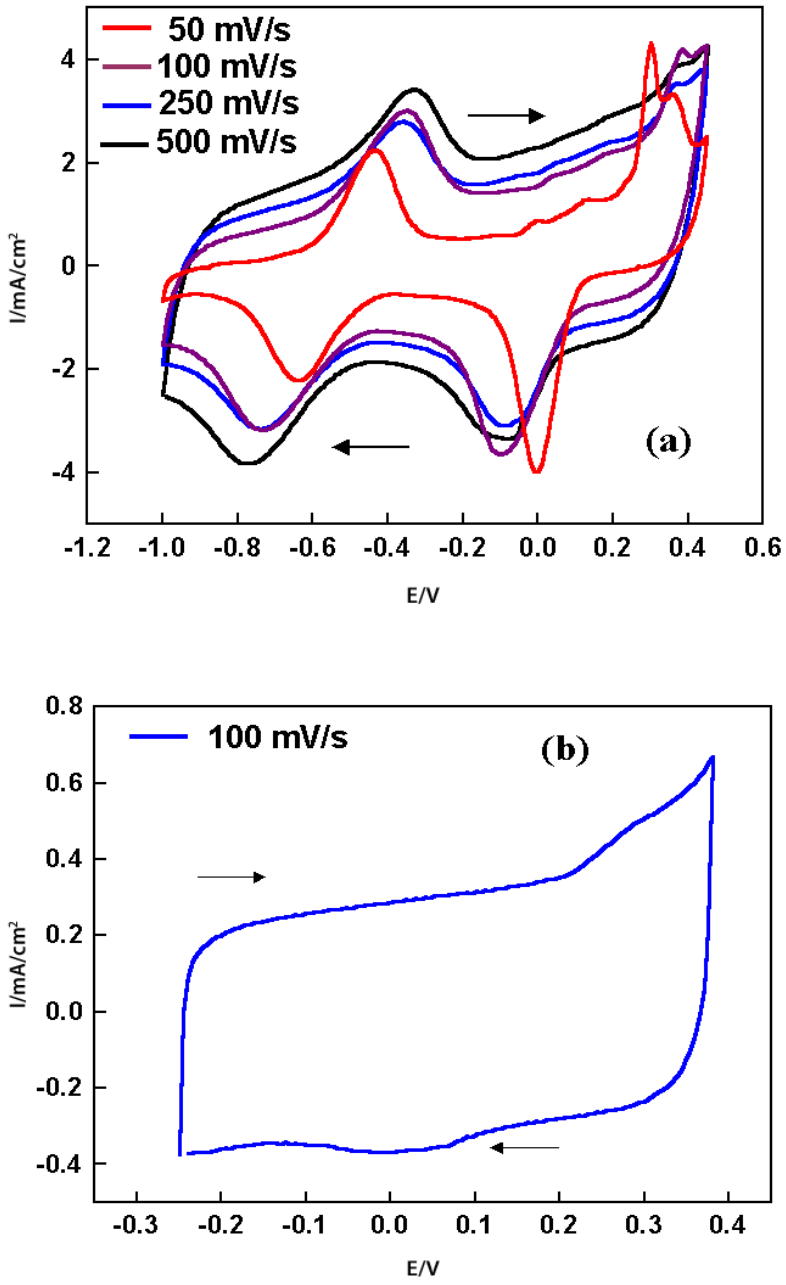

Figure 3-4. (a) Cyclic voltammograms of Ru/MWCNT at various scan rates in 1 M H_2SO_4. The red colored trace corresponds to the first cycle and the other three were obtained after 50 cycles. Arrows indicate the direction of scan. (b) A stable cyclic voltammogram of Ru/MWCNT obtained after 100 cycles at a scan rate of 100 mV/s in 1 M H_2SO_4. Arrows indicate the direction of scan.

3.3.5 Electrochemical impedance spectroscopy (EIS) analysis

Impedance spectroscopy is a valuable tool not only to determine the equivalent series resistance but also to study the interfacial and pseudocapacitance of the electrode structure. In this technique an alternating voltage is applied to the electrode interface, the response is represented by the imaginary component, Z", of the impedance which is the capacitance of the electrode structure given by the equation $Z"=1/j\omega C$.

Figure 3-5 shows complex plane plots of the impedance of both MWCNTs and Ru/MWCNTs in 1 M H_2SO_4. For the convenience of interpretation these plots can be divided in to high and low frequency regions. The frequency at which there is deviation from the semicircle is known as 'knee' frequency, which reflects the maximum frequency at which capacitive behavior is dominant.

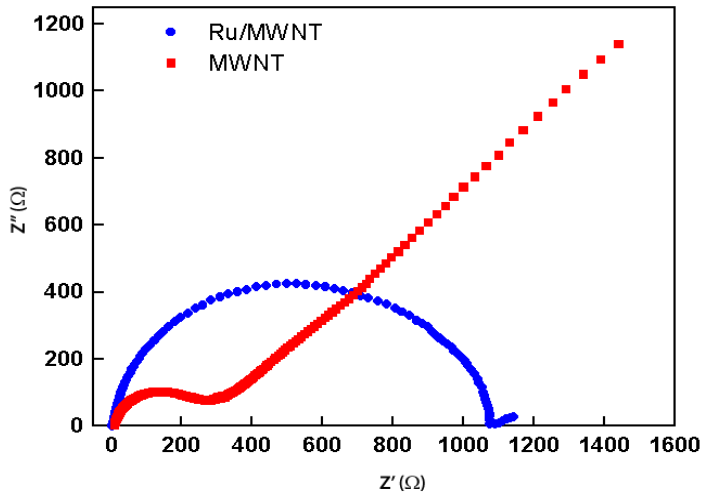

Figure 3-5. Complex plane impedance plots of MWCNT (red) and Ru/MWCNT (blue) in 1 M H_2SO_4

The presence of larger semicircle in the high frequency region for the Ru/MWCNT suggests that there is a charge transfer resistance. For MWCNTs [26], there is small semicircle in the high frequency region while in the low frequency region, there is a straight line angled at more than 45° to the real axis, the behavior that can be attributed to the porous nature of the MWCNTs.

The central hollow core of the nanotubes is accessible for the double layer charging and thus the opened CNTs act as a condenser for the accumulation of the charges. The Ru/MWCNTs show variations from this behavior as it shows the presence of large semicircle. This is due to the presence of Ru on MWCNTs which offers resistance to the diffusion of the electrolyte ions within the pores of the MWCNTs. Although the

model-dependent capacitance obtained from the impedance is considerably lower than the capacitance from voltammetric data, an order of magnitude enhancement in capacitance suggests the positive role played by ruthenium species attachment. Table 3-5 shows various parameters such as solution resistance [R_S (Ω)], faradic resistance [R_{CT} (Ω)] and capacitances of both MWCNT and Ru/MWCNT.

Table 3-5. Impedance parameters obtained after CNLS fitting.

Sample	R_s (Ω)	R_{CT} (Ω)	Capacitance (F)
MWCNT	9.34	266	5.6×10^{-6}
Ru/MWCNT	4.45	1074	7.0×10^{-5}

All the above results are in agreement with the functionalization of MWCNTs with hydrous ruthenium oxide. Since the characterization of functionalized species is a major challenge in CNT chemistry, we can only speculate the details about how ruthenium oxide species is attached to the tubes.

In particular, the sidewall chemistry on the basis of surface reaction of oxygenated functional groups with hydrous ruthenium oxide (RuO·OH) to eliminate water and/or CO_2 forming a covalent bond is perhaps important. The possible derivatization of carboxylic groups by hydrous ruthenium oxide to form Ru–O–C bond on the sidewalls of MWCNTs could be responsible for exhibiting the interesting properties relevant in supercapacitor applications.

3.4 Conclusion

In this work we have shown that the inherent electrochemical capacitance of MWCNTs can be significantly enhanced by hydrous ruthenium oxide functionalization. Oxidative treatment of MWCNTs generates oxygenated functional groups at the defective sites which can be further derivatized by hydrous ruthenium oxide. This ruthenium oxide owing to its pseudocapacitive behavior significantly increases the capacitance of MWCNTs. The long term stability or cycle life of ruthenium oxide as compared to the polymer material has an additional advantage besides enhanced capacitance. Cyclic voltammetry shows cycle dependent behavior and almost constant current against the applied potential with a weakly distinct electrochemical couple indicating uniform infusion of electrons. Impedance analysis shows large charge transfer resistance for Ru/MWCNT.

3.5 References

1. B. E. Conway, Electrochemical Supercapacitors: Scientific Fundamentals and Technological Applications 1999.
2. J. R. Miller, in: S.P. Wolsky, N. Marincic (Eds.), Proc. 11th Intl. Seminar on Primary and Secondary Battery Technologies and Applications, Florida Educational Seminars, Boca, Raton, FL, 1994.
3. J. M. Miller, B. Dunn, T. D. Tran, R. W. Pekala, Journal of the Electrochemical Society 1997, 144.
4. J. M. Miller, B. Dunn, Langmuir 1999, 15, 799-806.
5. H. Probstle, S. Schmitt, J. Frick, J. Power Sources 2002, 105, 87.
6. S. A. Al-Muhtaseb, J. A. Ritter, Advanced Materials 2003, 15, 101-114.
7. S. T. Mayer, R. W. Pekala, J. L. Kaschmitter, Journal of the Electrochemical Society 1993, 140, 446-451.
8. M. Mastragostino, C. Arbizzani, F. Soavi, Solid State Ionics 2002, 148, 493-498.
9. M. Mastragostino, C. Arbizzani, F. Soavi, Journal of Power Sources 2001, 97-98, 812-815.
10. C. Arbizzani, M. Mastragostino, L. Meneghello, R. Paraventi, Advanced Materials 1996, 8, 331-334.
11. S. Ghosh, O. Inganas, Adv. Mater. 1999, 11, 1214-1218.
12. D. Qu, Journal of Power Sources 2002, 109, 403-411.
13. M. S. Dresselhaus, G. Dresselhaus, P. C. Eklund, Science of Fullerenes and Carbon Nanotubes 1996.
14. C. Niu, E. K. Sichel, R. Hoch, D. Moy, H. Tennent, Applied Physics Letters 1997, 70, 1480-1482.
15. E. Frackowiak, F. Béguin, Carbon 2001, 39, 937-950.
16. E. Frackowiak, S. Delpeux, K. Jurewicz, K. Szostak, D. Cazorla-Amoros, F. Béguin, Chemical Physics Letters 2002, 361, 35-41.
17. M. Hughes, M. S. P. Shaffer, A. C. Renouf, C. Singh, G. Z. Chen, D. J. Fray, A. H. Windle, Advanced Materials 2002, 14, 382-385.
18. M. Hughes, G. Z. Chen, M. S. P. Shaffer, D. J. Fray, A. H. Windle, Chemistry of Materials 2002, 14, 1610-1613.
19. C. C. Hu, Y. H. Huang, K. H. Chang, Journal of Power Sources 2002, 108, 117-127.
20. K. W. Nam, K. B. Kim, Journal of the Electrochemical Society 2002, 149.
21. W. Dmowski, T. Egami, K. E. Swider-Lyons, C. T. Love, D. R. Rolison, Journal of Physical Chemistry B 2002, 106, 12677-12683.
22. D. A. McKeown, P. L. Hagans, L. P. L. Carette, A. E. Russell, K. E. Swider, D. R. Rolison, Journal of Physical Chemistry B 1999, 103, 4825-4832.

23. R. Andrews, D. Jacques, A. M. Rao, F. Derbyshire, D. Qian, X. Fan, E. C. Dickey, J. Chen, Chemical Physics Letters 1999, 303, 467-474.

24. J. Chen, M. A. Hamon, H. Hu, Y. Chen, A. M. Rao, P. C. Eklund, R. C. Haddon, Science 1998, 282, 95-98.

25. D. Bom, R. Andrews, D. Jacques, J. Anthony, B. Chen, M. S. Meier, J. P. Selegue, Nano Letters 2002, 2, 615-619.

26. Z. H. Yang, H. Q. Wu, Chemical Physics Letters 2001, 343, 235-240.

CHAPTER 4

Iridium oxide functionalized multi-walled carbon nanotubes for supercapacitor applications.

This chapter shows that the inherent electrochemical capacitance of MWCNTs can be significantly enhanced by Iridium oxide functionalization. Oxidative treatment of MWCNTs generates oxygenated functional groups at the defective sites which can be further derivatized by Iridium oxide. This Iridium oxide owing to its pseudocapacitive behavior significantly increases the capacitance of MWCNTs. Supercapacitor performance was evaluated by cyclic voltammetry and Impedance spectroscopy.

4.1 Introduction

Charge storage in a capacitive mode offers several advantages over conventional batteries such as charging within seconds, long-term cycling stability and almost ten times more power density than batteries [1]. These features are desirable in a wide range of applications. Transition metal oxides are very attractive materials for these applications because of their ability to store the charge by both Faradaic and non-Faradaic mechanisms. As it is described in the earlier chapter, charge storage in capacitors involves two mechanisms: (1) charge is stored electrostatically from the reversible adsorption of electrolyte ions onto the surface of a material. (2) electrolyte ions react with the electroactive material accompanying changes in the composition or phases of the material. This mechanism is common for batteries. In this context, transition metal oxides possess desirable properties: (a) they have moderate electronic conductivity; (b) they exhibit multiple oxidation states (between which electron hoping takes place) that can coexist over a continuos range with no phase changes involving irreversible modifications of three-dimensional structure; and (c) protons can freely intercalate reversibly into the oxide lattice during redox reaction, allowing facile interconversion of $O^{2-} \leftrightarrow OH^{-}$[1]. Many transition metal oxides such as RuO_2[2], MnO_2[3], Co_3O_4[4], and V_2O_5[5] etc. have been explored for supercapacitor applications.

However the commercial applications of the metal oxides have been hindered by their high cost, moderate or poor electronic conductivity resulting in a low power density, narrow operation voltage window, and sluggish Faradaic redox kinetics [6]. One of the strategies to overcome these limitations is to disperse the nanostrctured metal oxides onto a high surface area carbon substrates such as carbon nanotubes. CNTs due to their unique electronic, mechanical and structural properties offer several advantages as a three-dimensional support. The randomly entangled mesoporous network of CNTs provides the electronic conducting pathways which allow the diffusion of ions easily to the active surface area of the nanosized metal oxides and thus facilitates the Faradaic processes across the interface.

In this chapter, the supercapacitor applications of IrO_2 functionalized MWCNTs are explored. The general oxidation reaction for iridium[4.4] can be written as:

$$IrO_2(OH)_6 \leftrightarrow IrO_{(a+\delta)}(OH)_{(a+\delta)} + \delta H^+ + \delta e^- \qquad 4.4$$

The stoichiometry changes from $Ir(OH)_2$ to IrO_2 involving a change of color or reflectivity of the material. The IrO_2 nanoparticles supported on MWCNT network offers a capacitance around 137 F/g.

4.2 Experimental

All the experimental details including the oxidation of MWCNTs and their functionalization with IrO_2, SEM, and electrochemical characterizations are similar to the chapter three. Briefly, oxidized MWCNTs were dispersed in isopropanol (1:1 volume) solution by a probe sonicator for 2 h, to which $IrCl_3.nH_2O$ (Aldrich) was added (0.5 wt%

ratio) and the mixture is again agitated with the aid of probe sonicator for 1 h. The Ir/MWCNTs mass was filtered and washed thoroughly with deionized water to remove excess chloride ions and the sample was dried in an oven at 110 °C. The dried sample was heated in hydrogen atmosphere at 300 - 350 °C for 1 h.

Raman spectroscopy was carried in a backscattering geometry with 514.5 nm excitation from an Ar^+ ion laser using Jobin-Yvon HR800 instrument.

4.3 Results and Discussion

4.3.1 Scanning electron microscopic study

Figure 4-1 display the SEM image of Ir/MWCNTs. The diameter of MWCNTs was in the range of 30-150 Å and they formed randomly oriented mesoporous network.

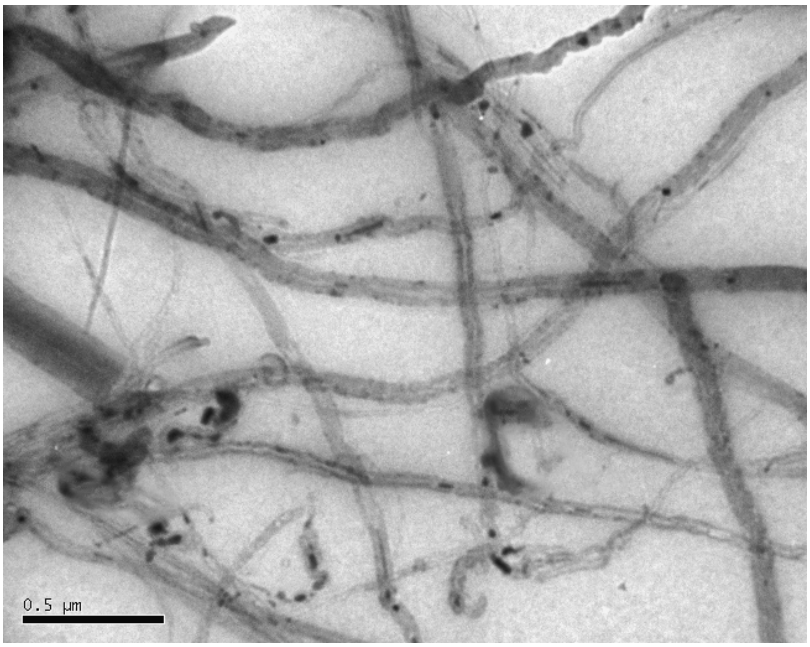

Figure 4-1. SEM image of iridium functionalized MWCNTs.

The entangle network of MWCNTs was functionalized with IrO_2 which can be seen as small lumps around the tube walls as seen from the figure. The presence of Ir on MWCNTs was confirmed by EDAX.

4.3.2 Raman spectroscopy

The structural changes of MWCNTs and Ir/MWCNTs were followed by using Raman spectroscopy performed with an 514.5 nm (Ar^+ ion) laser excitation. Figure 4-2 shows Raman spectra of both MWCNTs and Ir/MWCNTs.

Three distinct peaks can be seen from the spectra- 1) the D-band in the range

of 1300-1400 cm^{-1}; the disorder induced band in graphite lattice that reflects defects in CNTs, 2) the G-band in the range of 1500-1600 cm^{-1}; due to the tangential vibration of carbon atoms, and 3) the D*-band in the range of 2600-2800 cm^{-1}; the second harmonic of D-band [7].

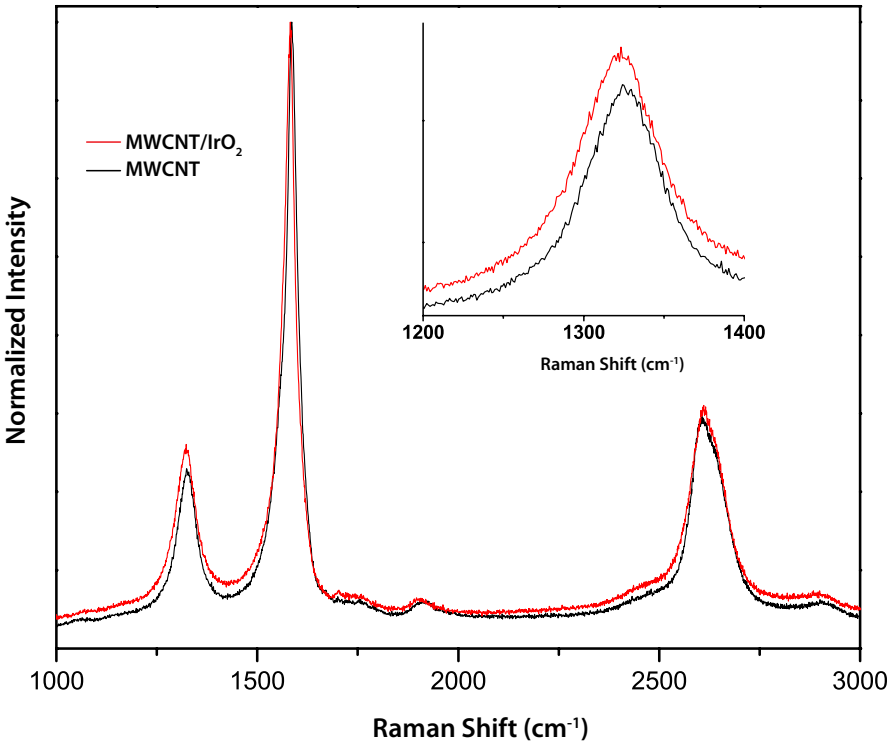

Figure 4-2. Selected portion of Raman spectra of MWCNTs and Ir/MWCNTs recorded with 514.5 nm laser excitation. Inset shows the expanded region of the D band. The spectra were normalized to the G band intensity.

The structural purity of the nanotubes can be estimated qualitatively by calculating the intensity ratio of D and G-bands (I_D/I_G) [7]. As it can be seen from the figure 4-2, the relative intensity of D-band of MWCNTs is increased after functionalization with IrO_2. The oxidative treatment to the CNTs introduces defects in the lattice structure along with the generation of surface oxygenated functionalities, among which carboxylic groups are predominant. It is speculated that IrO_2 linkage in MWCNTs might have involved these surface functional groups as we have seen already in the case of Ru/MWCNTs samples in the earlier chapter. The I_D/I_G ratios calculated for MWCNTs and Ir/MWCNTs were 0.28 and 0.32 respectively; the increased ratio is a clear indication of functionalization.

4.3.3 Cyclic voltammetry studies

Typical voltammograms of Ir/MWCNTs measured in 0.5 M H_2SO_4 using Ag/AgCl as a reference electrode are shown in the figure 4-3. Several distinct features can be seen both on the anodic and cathodic half-cycles. These features are labeled from A_1 to A_4 for

anodic process and C_2 to C_4 for cathodic currents. The current increase at the terminal point of the anodic scan labeled as position A_5 is due to the oxygen evolution reaction. The hydrogen evolution occurred at the potential 0.655 V vs. Ag/AgCl and is labeled as C_0.

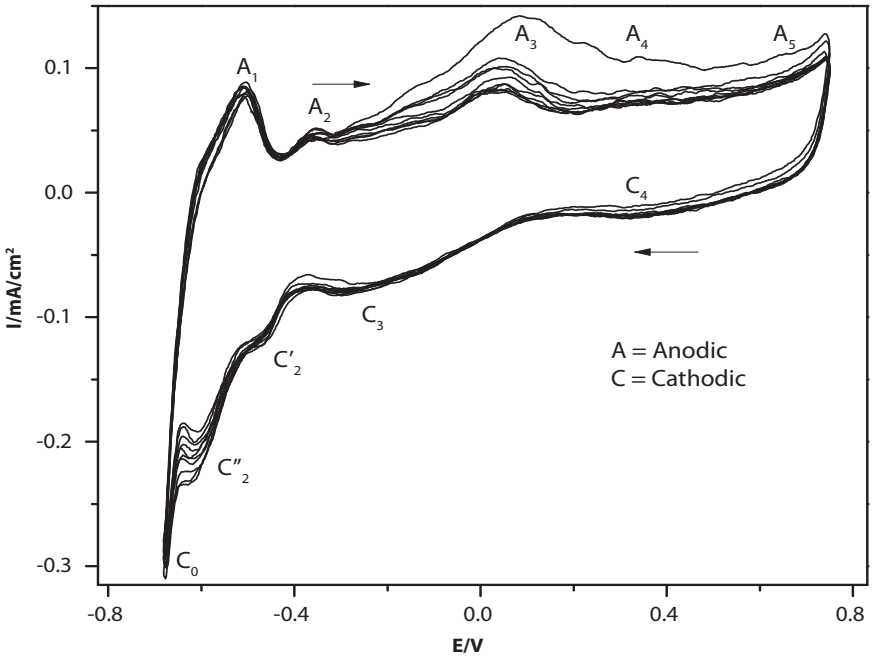

Figure 4-3. Cyclic voltammograms of Ir/MWCNTs in 0.5 M H_2SO_4 recorded at 20 mV/s vs Ag/AgCl. Arrows indicate direction of the voltammograms. Anodic scans are labeled as 'A' while cathodic as 'C'.

Although the basic understanding of the voltammetric behavior of IrO_2 has been derived from that of RuO_2, there are significant differences in CV characteristics of both the systems especially in terms of hydrogen and oxygen evolution reactions [8]. The cathodic scan shows two small peaks C'_2 and C''_2 which represent hydrogen deposition/ionization region. The pair of peaks A_3/C_3 and A_4/C_4 can be attributed to the redox transitions of surface oxyiridium groups, i.e., Ir(VI)/Ir(IV) and Ir(IV)/Ir(III). One of the main requirement for pseudocapacitive behavior is the coexistence of multiple oxidation states between which electron hoping can take place. As it can be seen from the voltammograms, Ir coexists in multiple oxidation states.

Another important parameter for higher pseudocapacitance is the facile electron and proton hoping in hydrous lattice structures, allowing proton intercalation [1]. As it can be seen from the hydrogen deposition/ionization region (C'_2 and C''_2), the hydrogen can interact with the metal oxide structure in a number of ways. Moreover hydrogen can penetrate through the lattice channels and form intercalation structures. The penetration depth increases upon cycling as it is evident from the increase in the anodic and cathodic scan currents shown in the figure 4-3. The randomly entangled

network of carbon nanotubes matrix provides conducting pathways for the electrolyte ions to the active sites of IrO_2. It also contributes to the overall capacitance by forming double-layer across its interface.

The capacitance of Ir/MWCNTs was calculated by integrating the voltammetric charges according to the equation 4.5.

$$q = \frac{1}{\upsilon} \int_{Ec}^{Ea} | i | dE \qquad 4.5$$

where E is the electrode potential, i is the measured current density, v is the scan rate, and E_c and E_a are the cathodic and anodic potential limits, respectively. The capacitance values were obtained by using the potential range -0.65 V to 0.75 V vs Ag/AgCl for all the scans to get comparable values. The prominent contributions from oxygen and hydrogen evolution were subtracted by reducing the voltage limits during cycling, if necessary. The average capacitance calculated for Ir/MWCNTs was 137 F/g.

4.3.4 Electrochemical impedance spectroscopy (EIS) analysis

Figure 4-4 displays the impedance analysis of Ir/MWCNT system in 0.5 M H_2SO_4 for the frequency range 10 mHz to 100 kHz with a 10 mV amplitude ac signal.

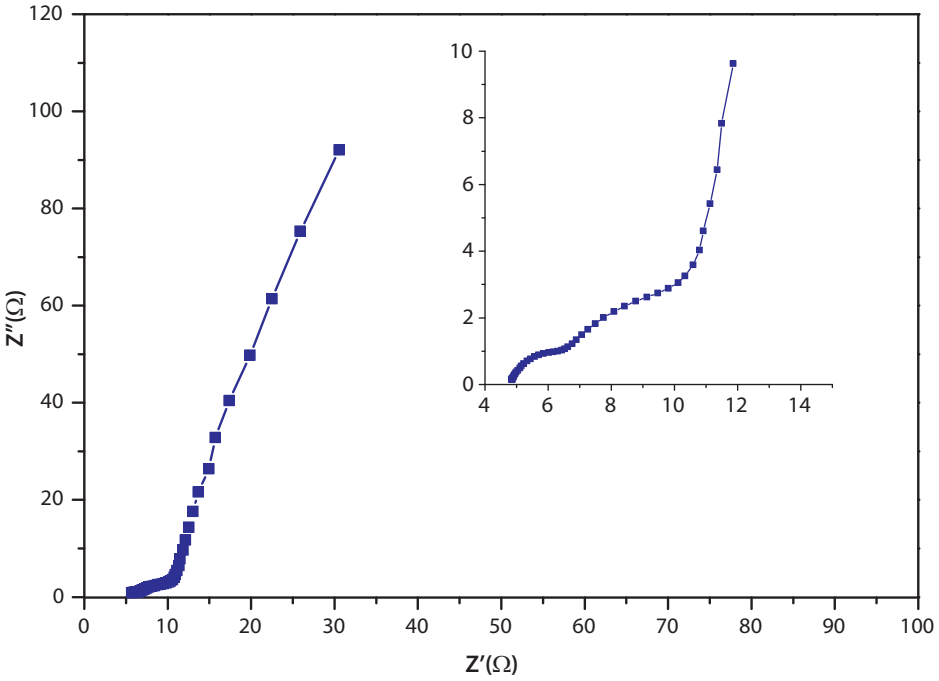

Figure 4-4. Impedance analysis of Ir/MWCNTs sample in 0.5 M H_2SO_4. Inset shows the presence of two semicircles in the higher frequency region.

As it can be seen from the figure 4-4, there are two semicircles in the higher frequency region, a typical of pseudocapacitive system [1, 9]. The lower frequency region reflects the diffusion processes defined by the Warburg impedance if the line exhibits 45° phase angle over a wide range of frequencies [10]. Analysis of impedance can be done by fitting the results with complex non-linear square (CNLS) method and interpreting the results in terms of equivalent circuits as shown in the figure 4-5.

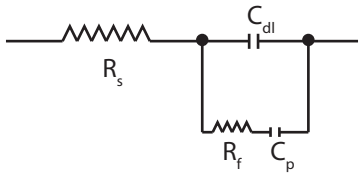

Figure 4-5. Equivalent circuit for a pseudocapacitive system like Ir/MW-CNT

The pseudocapacitive system like Ir/MWCNTs involves capacitance contribution from redox processes from surface active species and from intercalation processes into the oxide lattice. The equivalent circuit for this system involved three elements: the double-layer capacitance, C_{dl}, a Faradaic resistance, R_F, corresponding to the reciprocal of the potential-dependent charge transfer rate, and a pseudocapacitance, C_p, associated with the Ox and Red species in a redox reactions. Thus, the presence of two semicircles in Ir/MWCNTs denotes the contribution from redox capacitance or Faradaic capacitance and intercalation capacitance. The MWCNTs provide mesoporous support matrix to the nanosized metal oxide particles, the behavior reflected in the lower frequency region.

4.4 Conclusion

Transition metal oxides such as RuO_2, IrO_2 are the attractive materials for the energy storage devices such as supercapacitors owing to their ability to store the charge by involving Faradaic, non-Faradaic and intercalation mechanisms. However realization of their full potential is hindered by their poor electronic conductivity and sluggish redox kinetics. These limitation can be overcome by dispersing nanosized metal oxides within the three dimensional network of carbon nanotubes which provides an electronic conducting pathway for the electrolyte ions to the active sites of the metal oxides. The MWCNTs were functionalized with IrO_2 and their electrochemical properties were explored to understand the charge storage mechanism. The charge storage in this system involved contributions from Faradaic, non-Faradaic and intercalation mechanisms. The capacitance for Ir/MWCNTs was calculated to be 137 F/g using cyclic voltammetry.

4.5 References

1. B. Conway, Electrochemical supercapacitors: scientific fundamentals and technological applications, Springer Us, 1999.
2. G. Arabale, D. Wagh, M. Kulkarni, I. Mulla, S. Vernekar, K. Vijayamohanan, A. Rao, Chemical Physics Letters 2003, 376, 207-213.
3. K. Rajendra Prasad, N. Miura, Electrochemistry Communications 2004, 6, 1004-1008.
4. Y. Shan, L. Gao, Materials Chemistry and Physics 2007, 103, 206-210.
5. H. Lee, J. Goodenough, Journal of Solid State Chemistry 1999, 148, 81-84.
6. P. Simon, Y. Gogotsi, Nature Materials 2008, 7, 845-854.
7. M. Dresselhaus, G. Dresselhaus, A. Jorio, A. Souza Filho, R. Saito, Carbon 2002, 40, 2043-2061.
8. (a) T. Hepel, F. H. Pollak, W. E. O'Grady, Journal of The Electrochemical Society 1985, 132, 2385-2390; (b) C. C. Hu, Y. H. Huang, K. H. Chang, Journal of Power Sources 2002, 108, 117-127.
9. A. Bard, L. Faulkner, Electrochemical methods: fundamentals and applications, Wiley New York, 1980.
10. E. Barsoukov, J. Macdonald, Impedance spectroscopy: theory, experiment, and applications, John Wiley and Sons, 2005.

CHAPTER 5

All solid-state carbon nanotubes-polybenzimidazole supercapacitor.

This chapter describes the fabrication of all Solid-State Supercapacitor prototypes that can operate at elevated temperatures (150-180 °C). The challenge was to identify the suitable polymer electrolyte membrane and couple it with carbon nanotubes. To make the nanotubes area accessible which is generally strongly hydrophobic, it was necessary to functionalize them in a unique way to facilitate the proton transport. The single-walled carbon nanotubes were functionalized with primary amine groups and coupled with H_3PO_4 doped polybenzimidazole membrane. Supercapacitor performance was evaluated by cyclic voltammetry and Impedance spectroscopy.

5.1 Introduction

There is currently a great interest in the development of thin, flexible, and lightweight energy storage devices such as supercapacitors and batteries, to fulfill the demands of modern technologies [1]. The fabrication of new integrated hybrid devices [2] is not only essential for high energy storage but also to meet the stringent shape and space requirements [3]. This chapter describes the fabrication of all solid-state supercapacitor prototype using CNTs and a solid polymer electrolyte- polybenzimidazole, that can operate at elevated temperatures (~150 °C).

Polybenzimidazole (PBI) is a high-performance polymer which has recently emerged as an alternative to Nafion in fuel cells because of its better thermal, mechanical, and chemical properties [4]. Films of PBI, when doped with strong acids such as phosphoric or sulfuric acid form a single phase polymer electrolyte system that conducts proton [5]. The proton conductivity of PBI depends on the level of acid doping as well as temperature. Being basic in nature ($pk_a \approx 6$), PBI can enhance the solubility of the acid in the polymer, allowing for doping levels of up to 50 wt% without any adverse effects on the polymer properties [6]. Phosphoric acid is a very good proton conductor characterized by a very small Debye length and an amphoteric nature [7]. When doped in PBI, a phosphoric acid molecule protonates the benzimidazole ring. The proton conduction mechanism involves the formation of chain-like hydrogen bond network between acid proton and nitrogen of imidazole ring [8].

To construct solid-state supercapacitor, PBI membranes doped with phosphoric acid were used as an electrolyte. SWCNTs were used as supercapacitor electrodes. To make the CNT area accessible, which is generally hydrophobic, they were functionalized with primary amine groups. These amine groups not only make the CNTs hydrophilic [9] but also form an adduct with the phosphoric acid molecules doped in PBI, thus acting as a bridge to facilitate the proton transfer.

5.2 Experimental

5.2.1 PBI membrane preparation

PBI was synthesized by polycondensation reaction of diaminobenzidine and isophthalic acid at 200 °C [10]. The obtained polymer was washed with base and subsequently dried in an oven at 100 °C. A PBI membrane with an inherent viscosity 1.2 dl g^{-1} in conc. H_2SO_4 was used to prepare the membranes by solution cast method. A 3% PBI solution in N, N-dimethylacetamide (DMAc) was solution cast in a petri dish and kept in a vacuum oven at 90 °C for 24 h maintaining dry conditions. The films were peeled-off by immersing in water. The resulting film was treated with water at 60 °C for a week to remove residual DMAc. The film was then dried at 100 °C under vacuum for two days. The film was then immersed in 88% H_3PO_4 for 72 h for doping and then dried in a vacuum at 100 °C for two days. The amount of phosphoric acid uptake was ~14 moles per repeat unit of PBI. The thickness of the film was 100 μm. The films were cut into required dimensions for making supercapacitor assembly.

5.2.2 Functionalization of SWCNTs

SWCNTs were obtained from Prof. Apparao M. Rao, Clemson University. The 25 mg of SWCNTs were refluxed in H_2SO_4/HNO_3(v/v 3:1) at 80 °C for 3 h to create surface oxygenated functionalities. The SWCNTs were then treated with $SOCl_2$ at 90 °C for 2 h to form acid chlorides. Finally they were treated with ethylene diamine (EDA) at 55 °C to form primary amines. Figure 5-1 shows the schematic illustration of the SWCNT functionalization.

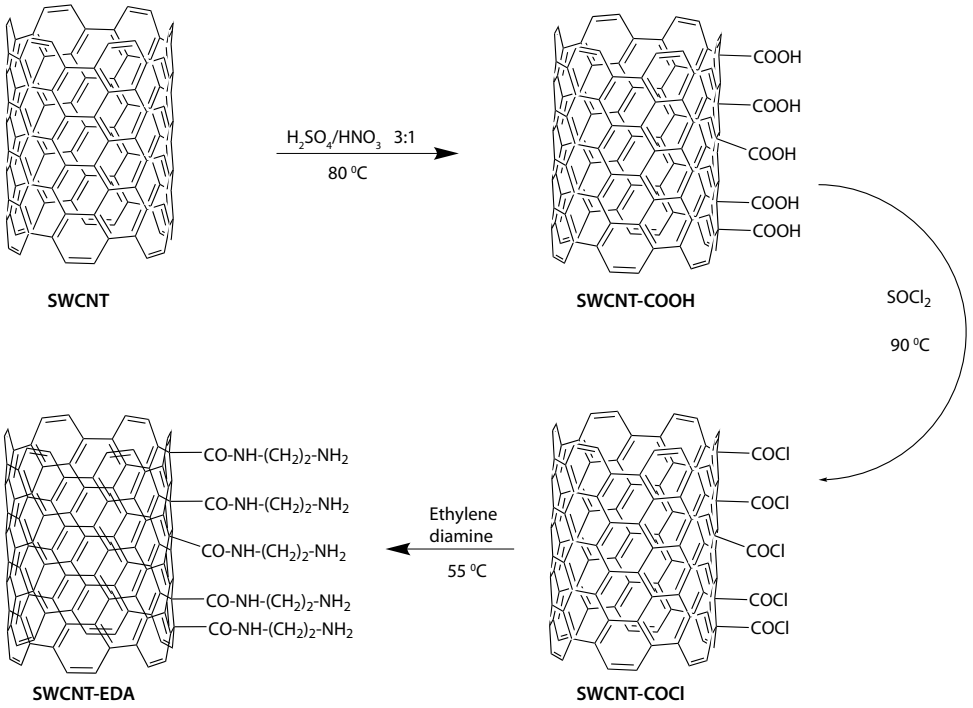

Figure 5-1. Schematic illustration of SWCNT functionalization to introduce primary amine functionality.

The reaction mixture was filtered through PTFE membrane (47 mm, 0.2 μ) and washed several times with methanol. The sample was dried in a vacuum oven at 60 °C. The CNTs in the form of buckypaper were peeled-off and cut into required dimensions.

5.2.3 Fabrication of supercapacitor

The amine functionalized SWCNT (SWCNT-EDA) films were cut into 1 cm^2 sizes. The H_3PO_4 doped PBI was cut into small pieces of size ~1.2 cm^2. To fabricate the supercapacitor assembly, the ~1.2 cm^2 PBI film (H_3PO_4 doped) was sandwiched between two SWCNT-EDA mats (1 cm^2) by hot pressing at 85 °C at a compaction load of 0.05 tones cm^{-1} for 4-5 min to establish a good contact between electrodes and membrane.

5.2.4 Characterization

The FTIR spectra were recorded on a Perkin-Elmer 16 PC FTIR spectrophotometer. The samples were measured by making KBr pellets as well as in

film form. All the electrochemical measurements were carried out in a Swagelok cell using computer-controlled potentiostat/galvanostat (Autolab PGSTAT 30 with GPES software). All the values were recorded with reference to the open circuit potential. A silver wire was used as a quasireference electrode for cyclic voltammetry measurements. Impedance measurements were carried out by using an ac signal of 10 mV amplitude over the frequency range 10 mHz to 100 kHz.

5.3 Results and Discussion

Figure 5-2 shows the schematic representation of the all solid-state supercapacitor concept.

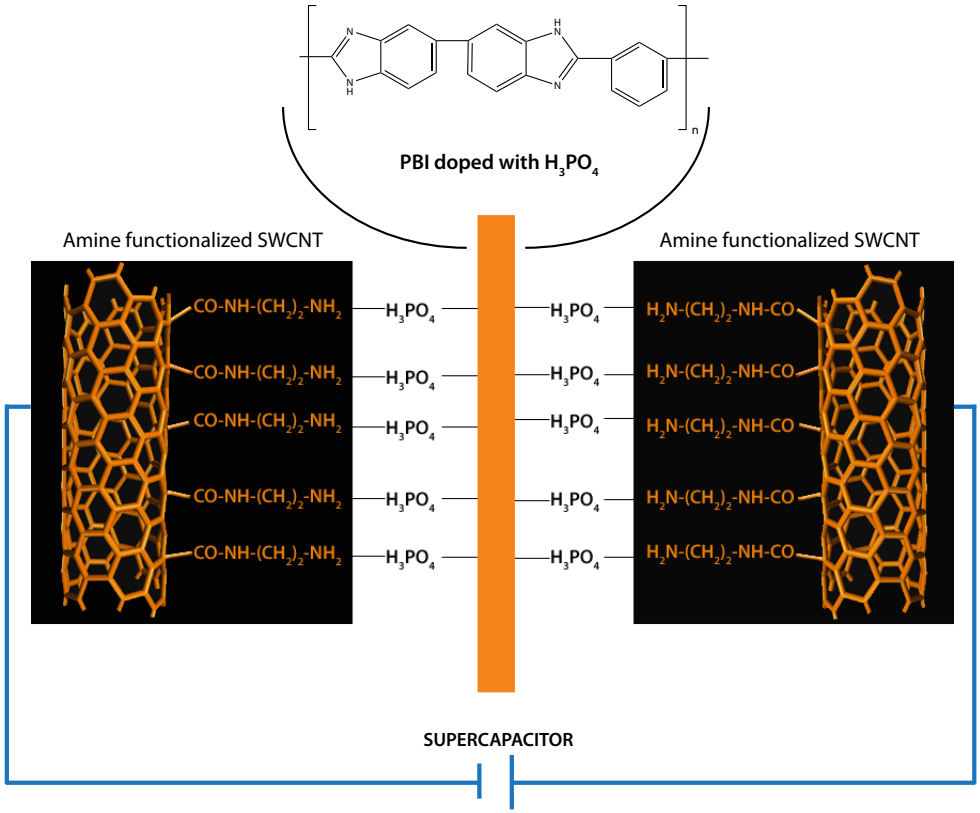

Figure 5-2. Schematic representation of the all solid-state supercapacitor using SWCNT-EDA as electrodes and phosphoric acid doped PBI as polymer electrolyte.

5.3.1 FTIR analysis

The surface chemical changes of SWCNTs after functionalization were followed by FTIR spectroscopy. Figure 5-3 shows the FTIR spectra of SWCNTs and amine functionalized SWCNTs. Acid treatment creates a number of functional groups on the CNTs such as α-diketone, ketone, phenolic, carboxylic, carbinol, hydroquinoid, lactone

of which the carboxylic groups are predominant [11]. These carboxylic groups can be further derivatized to create different functionalities.

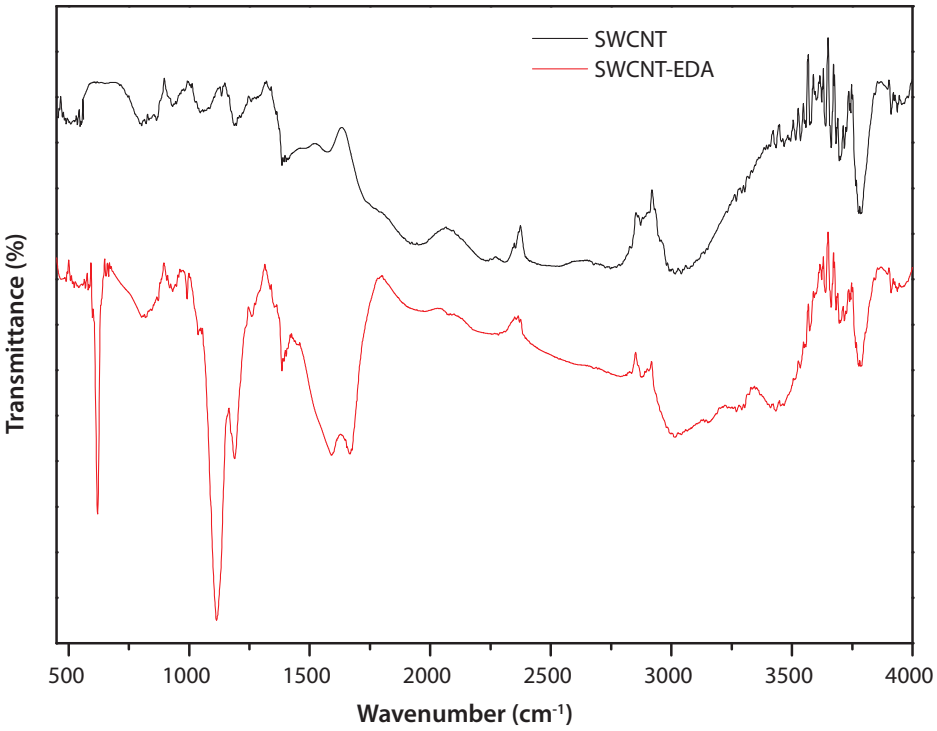

Figure 5-3. FTIR spectra of SWCNT and SWCNT-EDA. The surface functionalities can be conveniently followed by FTIR analysis.

The carboxylic groups were further derivatized to primary amines through amide linkage as seen in the figure 5-1. The FTIR spectrum of SWCNT-EDA (figure 5-3) shows peak at 1120 cm^{-1}, 1636 cm^{-1}, and 2933 cm^{-1}, which can be assigned to stretching vibrations of C-O single bonds and C-H bonds respectively. The broad band at 3400 cm^{-1} can be assigned to O-H stretching vibrations in alcohols. The peaks at 2950, 2920, 2850, 1460, and 1335 cm^{-1} are assigned to the aliphatic C-H stretching. The peaks at 3862 cm^{-1}, 3765 cm^{-1}, 2924 and 2049 cm^{-1} are attributed to N-H stretching and C-H stretching respectively. The peaks at 3865 cm^{-1}, 2345 cm^{-1}, 1028 cm^{-1}, 1667 cm^{-1}, and 818 cm^{-1} indicate N-H stretching , C-H, C=O, and C-N stretching respectively [12].

Introduction of amine functionalities changes the hydrophobic nature of SWCNTs to more accessible hydrophilic surface because of which the electrolyte ion or the cation can reach more active sites of SWCNTs resulting in the capacitance improvement. Also the amine functionalities can act as a sort of bridge between CNTs and polymer electrolyte membrane by forming bonds with unbound phosphoric acid of the membrane. The conduction of proton in PBI membrane happens through the formation linear chain-like hydrogen bond network that involves the participation of

NH.....N bonds of imidazole group [13]. The amine functionalities of SWCNTs simply extends this network and can facilitate the proton transport to the interiors of SWCNTs surface which otherwise difficult to achieve with unfunctionalized SWCNTs owing to their hydrophobic nature.

5.3.2 Cyclic voltammetry

Figure 5-4 shows the cyclic voltammograms of SWCNT-EDA/PBI-H_3PO_4 assembly, recorded at different temperatures.

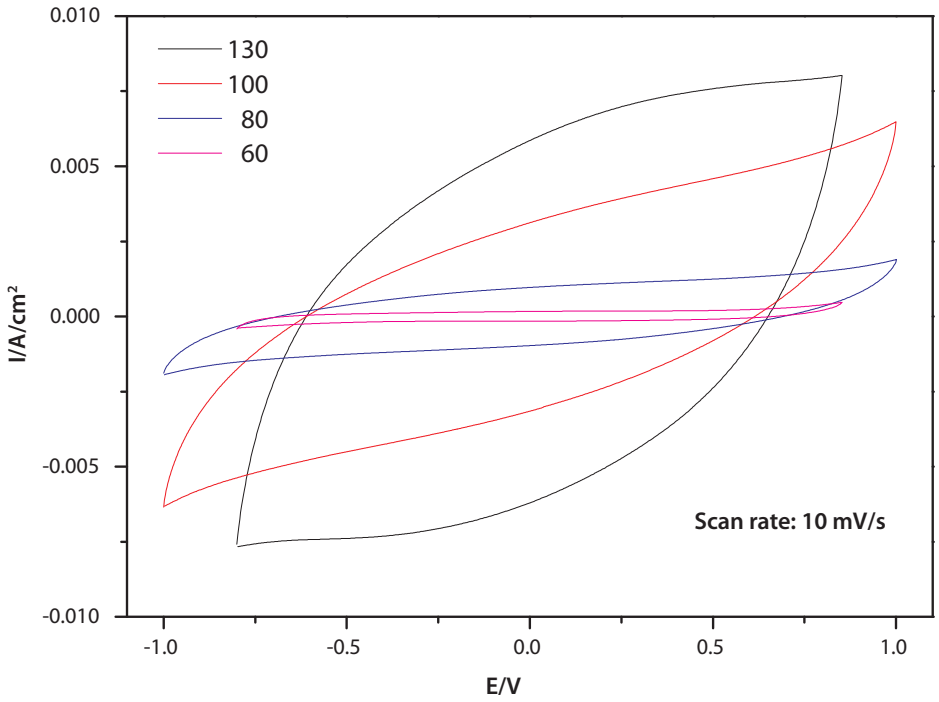

Figure 5-4. Cyclic voltammograms of SWCNT-EDA/PBI-H_3PO_4 supercapacitor assembly recorded at different temperatures: 60, 80, 100, and 130 °C. The proton conductivity of phosphoric acid doped PBI increases with temperature and subsequently that reflects in the capacitance value.

The capacitance was measured in the linear region of voltammograms. As it can be seen from the figure, the capacitance is dependent on temperature. The proton conductivity of acid doped PBI increases with increase in temperature [14] and acid-uptake [15]. However higher doping levels of acid affects the mechanical integrity of the film at higher temperature. Two processes contribute to the proton transport; diffusion of phosphate moieties and the rapid proton exchange between the phosphates acting as proton solvents. The ratio between the diffusion and hopping contribution to the proton transport was found to increase with the phosphoric acid content as well as temperature [16]. Figure 5-5 shows the proton conductivity of H_3PO_4 doped PBI at various temperatures. As it is evident from the figure, the acid doped membrane shows higher proton conductivity with the increase in temperature. This behavior is reflected

in the capacitance which also shows high value at higher temperature. At very higher temperature, the mechanical properties of PBI show degradation. To maintain the

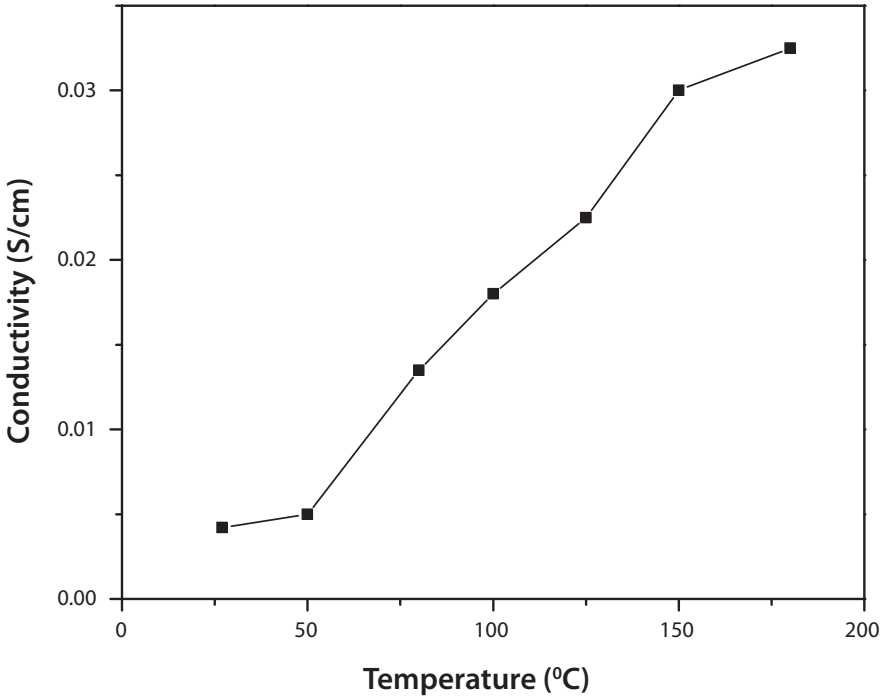

Figure 5-5. Proton conductivity of H_3PO_4 doped PBI, measured at different temperatures.

structural integrity of the polymer films, we carried the capacitance measurements up to 130-140 °C. The capacitance values obtained at different temperatures are summarized in Table 5-6.

Table 5-6. Capacitance values for SWCNT-EDA/PBI-H_3PO_4 measured at different temperatures.

Temperature (°C)	Capacitance (F/g)
60	8
80	12
100	23
130-140	32-39

5.3.3 Impedance analysis

Figure 5-6 shows the impedance spectra of SWCNT-EDA/PBI-H_3PO_4 supercapacitor assembly measured with an ac signal of 10 mV amplitude. As we have already seen, the proton conductivity increases with increase in temperature and at 130 °C, the sample shows higher capacitance. The impedance spectra corroborate this fact and they too show the similar trend. As already discussed, the bound and

unbound phosphoric acid molecule participate in the proton conduction. The bound acid molecules and acidic anions contribute to the proton conductivity via a mechanism called Grotthus mechanism while the conduction by unbound $H_2PO_4^-$ ions involve vehicle mechanism as well as Grotthus mechanism [7]. Hydrogen bonding plays important role

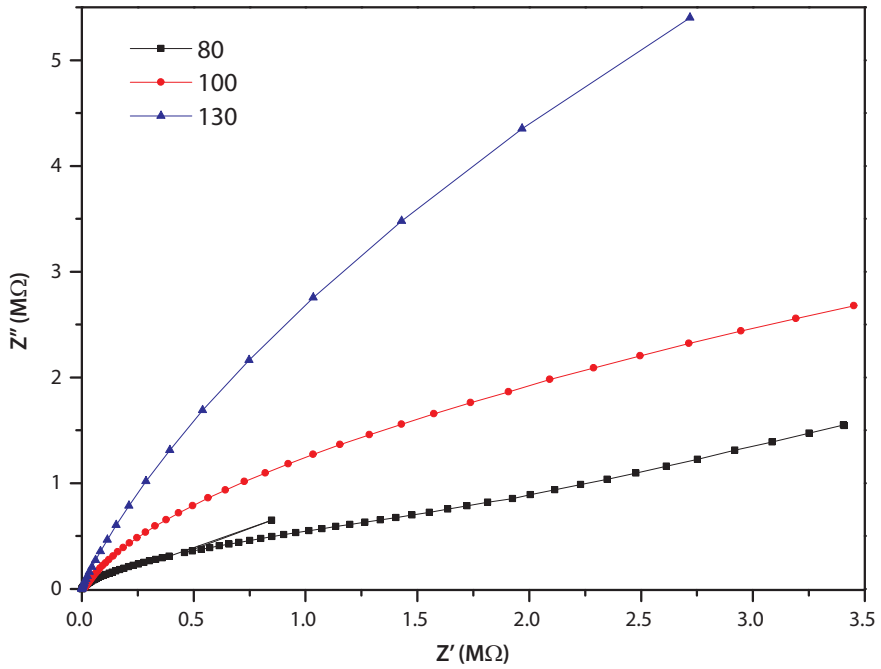

Figure 5-6. Impedance spectra of SWCNT-EDA/PBI-H_3PO_4 assembly at different temperatures: 80, 100, 130 °C. There was no measurable signal for the sample at 60 °C.

in both the mechanisms.

The rate of proton transfer between various species has been described as: H_3PO_4 to H_2O > H_3PO_4 to $H_2PO_4^-$ > N-H^+ to H_2PO_4 > N-H^+ to H_2O > N-H^+ to N-H [7]. At higher acid doping level, all acid molecules are believed to donate a proton to the unprotonated N-site and to be bounded to the polymer matrix. In order to make use of unbounded acid molecules, we created amine functionalities on SWCNTs expecting them to participate in the conduction via the same mechanism.

To counter check, we also made a supercapacitor assembly of SWCNTs (without any functionalization) and PBI-H_3PO_4 and measured its capacitance by CV and impedance spectroscopy (data not shown here), where it showed a highest capacitance in the range of 9-13 F/g at 130 °C, clearly indicating the importance of functionalization.

In order to check the participation of primary amine groups in the conduction mechanism, we peeled-off the SWCNT-EDA mats from the supercapacitor assembly after CV and impedance measurements. These mats were analyzed by FTIR spectroscopy to follow the surface chemical changes. Figure 5-7 shows the FTIR spectra of SWCNT-EDA before and after the electrochemical measurements. It seems that primary amine groups

on SWCNTs indeed involved in the formation of conduction pathway as evident from their spectral modifications due to uptake of phosphoric acid. The spectral domains, particularly in the regions 2000-3500 cm^{-1}, 800-1300 cm^{-1} are obscured by the absorption due to hydrogen bonding and vibrations of hydrogen phosphate groups, respectively.

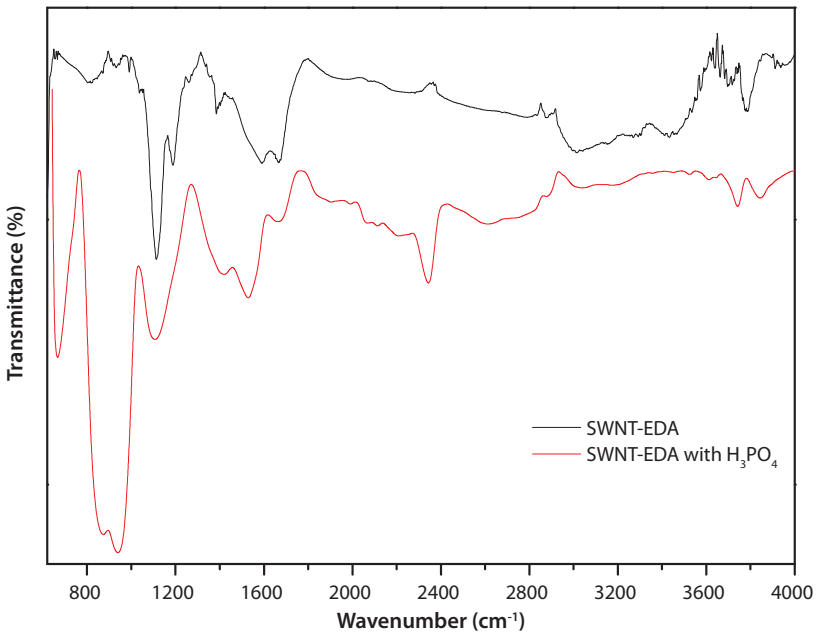

Figure 5-7. FTIR spectra of SWCNT-EDA and that of SWCNT-EDA; peeled-off from the supercapacitor assembly (SWCNT-EDA with H_3PO_4)

The absorptions at 870 {$\nu_s[P(OH)_2]$}, 986 {$\nu_{as}[P(OH)_2]$}, 1075 [$\nu_s(PO_2)$], 1120 [ν_{as}(PO2)] and 1173 cm^{-1}, [$\nu_{as}(PO_2)$] are all compatible with the presence of $H_2PO_4^-$. The formation of $H_2PO_4^-$ is speculated to be due to the protonation of nitrogen on SWCNT-EDA.

The high frequency region (2000-3500 cm^{-1}) shows the reduction in the peak intensities of free NH groups due to the masking by ν(OH) of H_3PO_4 or its anions. The broadness of the peaks in the lower frequency side in this region shows the formation of strong hydrogen bonds between NH groups, $H_2PO_4^-$ ions and H_3PO_4.

A shoulder to broadband at 2400 cm^{-1} can be attributed to the stretching vibrations of NH^+. The binding of H_3PO_4 increases the peak intensities of 1309, 1461, 1567, and 1630 cm^{-1}.

The presence of peak at 3625 cm^{-1} is attributed to the stretching vibration of water; that is associated with H_3PO_4 molecule and it can also contribute to its ionization, with concomitant formation of oxonium ions. It also indicates the low level doping of H_3PO_4. Thus, it is evident from FTIR analysis that amine functionalities of SWCNTs indeed participates in the conduction mechanism and thus helps to achieve maximum capacitance by forming a sort of bridge between SWCNT and PBI membrane. Oxidative treatment and further derivatization of CNTs usually makes them hydrophilic rendering

solubility in general solvents. With the broad knowledge of organic chemistry, one can manipulate the physical and chemical properties of CNTs.

5.4 Conclusions

A fabrication of all solid-state supercapacitor using amine functionalized CNTs and an acid doped PBI as a solid electrolyte membrane is described. The prototype can operate at higher temperature (100-150 °C) owing to the excellent thermal and mechanical properties of SWCNTs and PBI. The amine functionalization of SWCNTs makes the CNT surface more accessible to the cation for the formation of double-layer. The device offers excellent mechanical stability and is useful for the applications that require stringent shape and size constraints.

5.5 References

1. V. Pushparaj, M. Shaijumon, A. Kumar, S. Murugesan, L. Ci, R. Vajtai, R. Linhardt, O. Nalamasu, P. Ajayan, Proceedings of the National Academy of Sciences 2007, 104, 13574.
2. M. Kaempgen, C. Chan, J. Ma, Y. Cui, G. Gruner, Nano Lett 2009, 9, 1872-1876.
3. L. Hu, J. Choi, Y. Yang, S. Jeong, F. La Mantia, L. Cui, Y. Cui, Proceedings of the National Academy of Sciences 2009, 106, 21490.
4. J. Wainright, J. Wang, R. Savinell, M. Litt, H. Moaddel, C. Rogers, Proc. Electrochem. Soc 1994, 94, 255.
5. R. Bouchet, E. Siebert, Solid State Ionics 1999, 118, 287-299.
6. X. Glipa, B. Bonnet, B. Mula, D. J. Jones, J. Rozière, Journal of Materials Chemistry 1999, 9, 3045-3049.
7. K. Kreuer, S. Paddison, E. Spohr, M. Schuster, Chem. Rev 2004, 104, 4637-4678.
8. H. Pu, W. Meyer, G. Wegner, Journal of Polymer Science Part B: Polymer Physics 2002, 40, 663-669.
9. Y. Sun, K. Fu, Y. Lin, W. Huang, Acc. Chem. Res 2002, 35, 1096-1104.
10. Y. Saegusa, M. Horikiri, S. Nakamura, Macromolecular Chemistry and Physics 1997, 198, 619-625.
11. T. Ramanathan, F. Fisher, R. Ruoff, L. Brinson, Chem. Mater 2005, 17, 1290-1295.
12. G. Vukovic, A. Marinkovic, M. Colic, M. Ristic, R. Aleksic, A. Peric-Grujic, P. Uskokovic, Chemical Engineering Journal 2009.
13. R. He, Q. Li, G. Xiao, N. J. Bjerrum, Journal of Membrane Science 2003, 226, 169-184.
14. L. Qingfeng, H. Hjuler, N. Bjerrum, Journal of Applied Electrochemistry 2001, 31, 773-779.
15. P. Staiti, M. Minutoli, Journal of Power Sources 2001, 94, 9-13.
16. R. He, Q. Li, A. Bach, J. Jensen, N. Bjerrum, Journal of Membrane Science 2006, 277, 38-45.

CHAPTER 6

Energy storage applications of carbon nanotubes-PAN composites.

This chapter describes the supercapacitor applications of single-walled carbon nanotubes- polyacrylonitrile composites. The composite was characterized by TGA, IR and XRD. Impedance spectroscopy was done to measure the energy storage.

6.1 Introduction

The performance of an electrochemical capacitor is based on the charge accumulation from an electrolyte solution through electrostatic attraction by polarized electrodes [1]. The capacitance has a linear relationship with the electrode surface area. The surface area of an electrode can be manipulated by controlling the pore size distribution of the electrode material. In this context, allotropes of carbon are efficient materials for supercapacitor applications because of the richness of the variety of methods to control their pore size distribution [2]. Carbonization of polymers is one of the efficient way to produce high surface area electrode materials.

This chapter describes the synthesis of carbon/carbon composite using SWCNTs as a support matrix for carbonized polyacrylonitrile. SWCNTs forms mesoporous network of randomly entangled nanotubes which provides electronically conducting pathways and also improves mechanical properties of the composite. Polyacrylonitrile was selected because of its high carbonization yield with high residual nitrogen content [3], which can be a source of pseudocapacitance effects.

6.2 Experimental

SWCNTs (obtained from Clemson University) (15 wt%) were mixed with polyacrylonitrile (PAN, Aldrich) in an excess of acetone with the aid of a bath sonication to obtain slurry. Films of SWCNT/PAN were made by solution cast method by evaporating the solvent at 100 °C in a vacuum oven. The carbon/carbon composites were formed by carbonization of the SWCNT/PAN films at 700-800 °C in an inert atmosphere of nitrogen. The carbonized films obtained were compact and rigid with no apparent defects indicating strong bonding between SWCNTs and carbon matrix. The films were characterized by FTIR, XRD to follow the structural changes. The BET surface area was determined by N_2 adsorption-desorption method at 77 K using Quanta chrome NOVA-1200 adsorption unit. The self-standing films were used as electrodes without any binder. All the electrochemical measurements were carried in 0.1 M H_2SO_4 using Autolab (PG 30 with GPES) and impedance analyzer (with FRA software).

6.3 Results and Discussion

6.3.1 FTIR analysis

The structural changes in the film after carbonization were followed by FTIR and XRD. Figure 6-1 shows the FTIR spectra of PAN and SWCNT-PAN carbonized at 700 °C. The carbonization of PAN involves many process such as chain scission, chain breakdown, by-products evolution or cross-linking depending on heat treatment history [4]. The main scission products released during carbonization are HCN, NH_3, and nitrogen. Various amounts of water, carbon monoxide, and CO_2 are also formed. Small quantities of H_2 and CH_4 are also formed.

The original functional groups of PAN molecules (CH_3 and nitrile) appear in the

spectra. Along with these several new transition structures were formed, such as ketones, aldehydes, and carboxylic acid etc [5]. The peak at 1540 cm^{-1} is attributed to the C=C

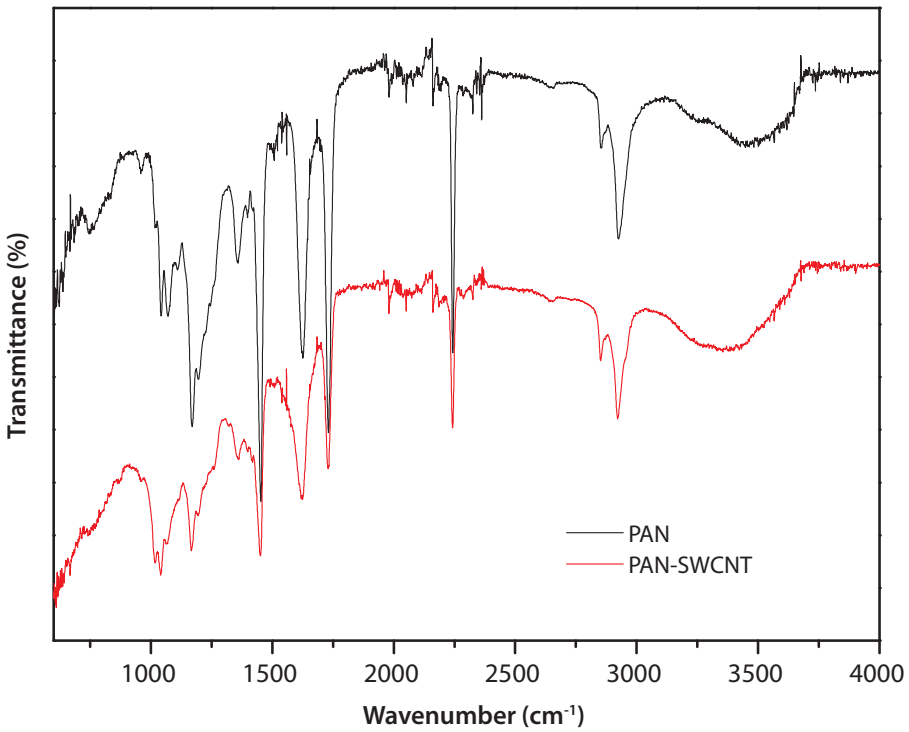

Figure 6-1. FTIR spectra of carbonized samples of PAN and SWCNT/PAN. The carbonization temperature was 700 °C

group. The nitrile group peak shows peak around 2226 cm^{-1} which usually disappears when heated above 750-800 °C. The peak around 1021 cm^{-1} attributed to the C-N bonding. The broad band around 3442 cm^{-1} is attributed to the N-H bonding. The peak around 1735 cm^{-1} is attributed to the aldehydic group. Aldehydic peak disappears when heated above 800 °C. The carbonization does not convert all the polymer into carbon due to the existence of other compounds. The presence of heteroatoms such as nitrogen is useful in the supercapacitor performance as they can contribute to the capacitance value through pseudocapacitance effects [3].

6.3.2 BET surface area

The BET surface area of the SWCNT/PAN sample was 481 m^2/g with an average pore diameter 7.3 nm. Generally the capacitance increases with the increase in the surface area. However the electrochemical response of porous materials is complex and it is difficult to separate the capacitance contribution from each factor individually. The surface area of SWCNTs alone was 398 m^2/g. Although the addition of PAN did not increase the surface area dramatically, nonetheless it provides extra surface area for the

electrolyte ion with it own unique pore structure.

6.3.3 XRD analysis

Figure 6-2 shows the XRD of SWCNT/PAN carbonized at 700 °C. The sample shows amorphous nature.

As we have seen in the FTIR analysis, the complete carbonization of PAN is

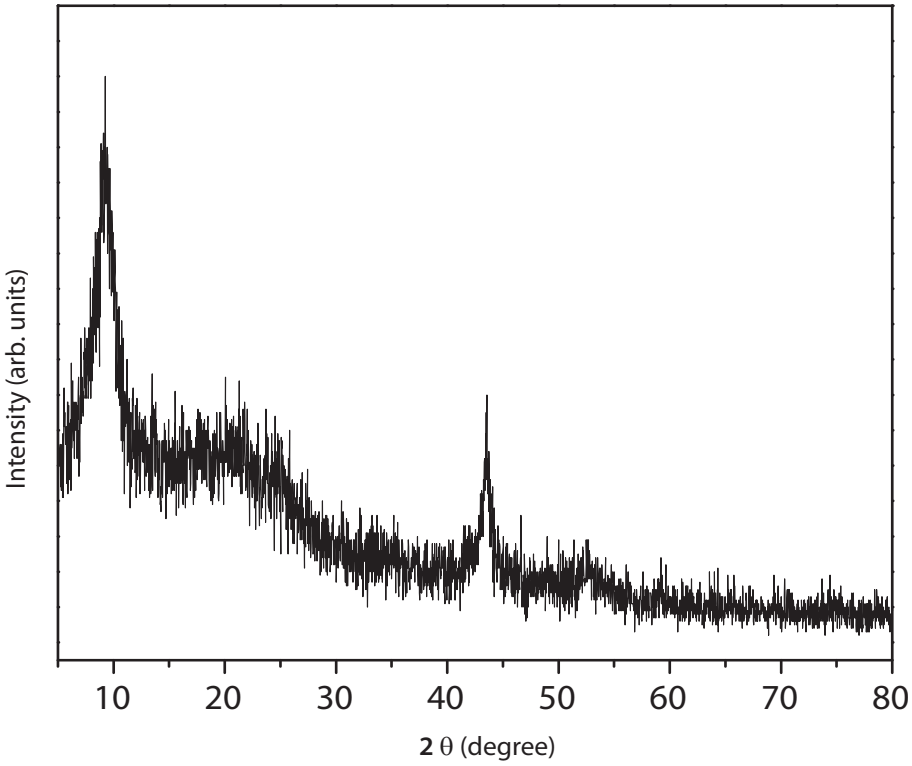

Figure 6-2. XRD of SWCNT/PAN carbonized film. The carbonization was carried at 700 °C.

not possible at 700-800 °C owing to the presence of other groups and they still contain residual nitrogen in the carbon matrix.

6.3.4 Cyclic voltammetry

The cyclic voltammetry of SWCNT/PAN was carried in 0.1 M H_2SO_4 using Ag/AgCl as a reference electrode. The carbonized films of SWCNT/PAN were composite used as a working electrode as such without any binder.

Figure 6-3 shows the cyclic voltammograms of SWCNT/PAN composite recorded at a scan rate of 5 mV/s. At lower scan rates (5-10 mv/s), the voltammograms show a typical "box-like" shape expected for an ideal supercapacitor. The lower scan rates typically allow the electrolyte ions to cover maximum surface area of the electrode allowing maximum charge accumulation at the interface, which usually reflects in the

capacitance values. The capacitance calculated was 142 F/g. The capacitance of SWCNTs alone was in the range of 26 - 32 F/g. The carbonized PAN serves as a support matrix providing extra surface area to the electrolyte ion. The presence of heteroatom- nitrogen in the carbonized matrix of PAN also contributes to the overall capacitance value of the

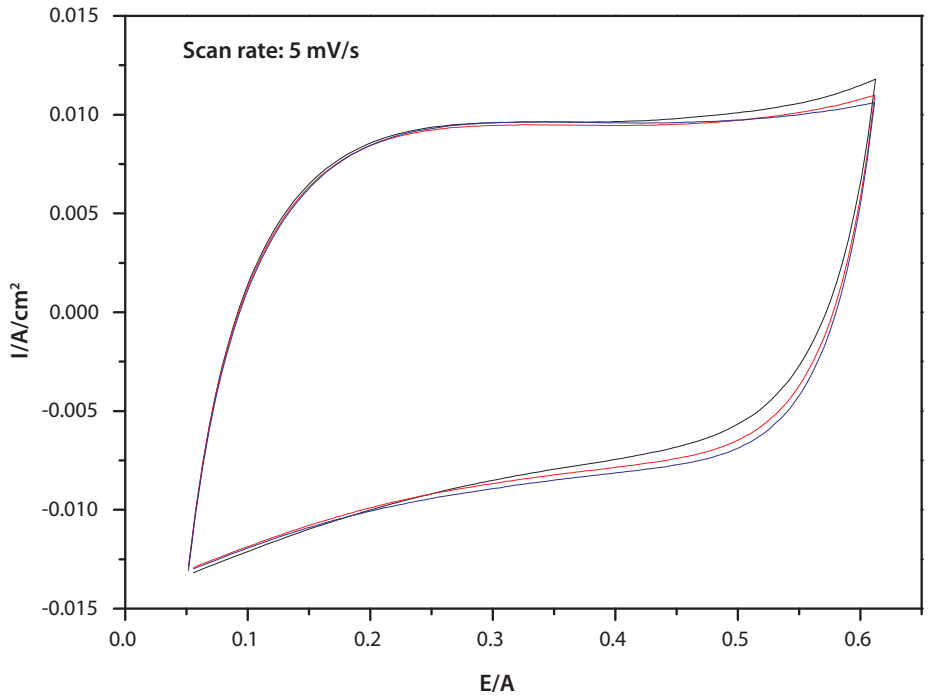

Figure 6-3. Cyclic voltammograms of SWCNT/PAN composite in 0.1 M H_2SO_4 at a scan rate of 5 mV/s vs. Ag/AgCl. The voltammograms show a typical "box-like" shape of an ideal capacitor.

system as it has been also observed for activated carbons with nitrogen functionality. It has been shown that carbon materials derived from quinoline show capacitance variation with the variation in the content of nitrogen. The PAN sample carbonized at 700 °C show higher content of residual nitrogen as we have already seen from FTIR analysis.

The different charge transfer reactions involving nitrogen functionalities are shown in the following equations [6.6 and 6.7]:

$$>C{=}NH + 2\ e^- + 2H^+ \leftrightarrow CH\text{-}NH_2 \qquad 6.6$$

$$>CH\text{-}NHOH + 2\ e^- + 2\ H^+ \leftrightarrow CH\text{-}NH_2 + H_2O \qquad 6.7$$

where >C stands for carbon network.

Thus, the composites of carbonized PAN and CNTs can be as electrode materials used in the supercapacitor devices owing to their superior capacitance, chemical stability [7], and the ability to form a double-layer in both aqueous and non-aqueous electrolytes [8]. The presence of nitrogen in the carbonized matrix improves the capacitance.

6.3.5 Impedance spectroscopy

Figure 6-4 shows the impedance spectrum of SWCNT/PAN composite recorded in 0.1 M H_2SO_4 in the frequency range of 10 mHz to 100 kHz with an amplitude of 10 mV.

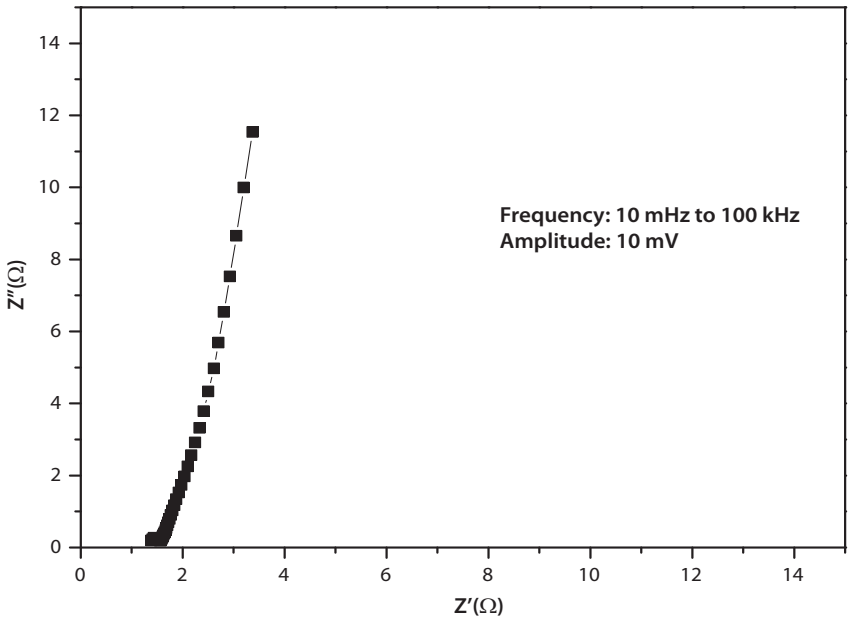

Figure 6-4. Impedance spectroscopy of SWCNT/PAN in 0.1 m H_2SO_4. Frequency range was 10 mHz to 100 kHz with an amplitude of 10 mV.

The impedance plot shows the value of R_s (solution resistance or initial resistance) below 1.5 ohms which reflects a low value of equivalent series resistance of the cell. The plot shows linearity; almost parallel to the imaginary axis, indicates a good capacitive behavior without diffusion limitations. The shorter time constant indicates the rapid dynamics of charge propagation. The power calculations ($P = V^2/4R_s$) reveals the applicability of this composite for high power capacitors.

6.4 Conclusions

The carbon/carbon composites have been prepared by one-step carbonization of SWCNT/PAN blends. The composite exhibits high capacitance properties owing to the pore structures and the pseudocapacitive properties of nitrogen functionality of carbonized PAN. The CNTs offers good mechanical support and provides electronically conducting pathways for the electrolyte ions to the active sites. The capacitance values (142 F/g) show the applicability of this composites in high power capacitors.

6.5 References

1. B. Conway, Electrochemical supercapacitors: scientific fundamentals and technological applications, Springer Us, 1999.
2. E. Frackowiak, F. Beguin, Carbon 2001, 39, 937-950.
3. E. Frackowiak, G. Lota, J. Machnikowski, C. Vix-Guterl, F. Béguin, Electrochimica Acta 2006, 51, 2209-2214.
4. M. M. Coleman, R. J. Petcavich, J Polym Sci Polym Phys Ed 1978, 16, 821-832.
5. M. Herrera, M. Wilhelm, G. Matuschek, A. Kettrup, Journal of Analytical and Applied Pyrolysis 2001, 58-59, 173-188.
6. J. Grimshaw, Electrochemical reactions and mechanisms in organic chemistry, Elsevier Science Ltd, 2000.
7. T. Liu, T. V. Sreekumar, S. Kumar, R. H. Hauge, R. E. Smalley, Carbon 2003, 41, 2440-2442.
8. E. J. Ra, E. Raymundo-Piñero, Y. H. Lee, F. Béguin, Carbon 2009, 47, 2984-2992.

PART B

| High-Performance Composites |

CHAPTER 7

Chirality dependent functionalization of carbon nanotubes with polybenzimidazole-terphthalate copolymer.

Carbon nanotubes were functionalized with a variant of polybenzimidazole polymer that selectively attaches to semiconducting carbon nanotubes which is reflected in their optical function. Nanotubes enhance the optical signal of polymer in the UV-Visible region and bleach it in the NIR region. Raman spectroscopy shows the selective functionalization of semiconducting nanotubes. The composite can be used in photovoltaic applications as well as in the separation of semiconducting CNTs from metallic one.

7.1 Introduction

Single-walled carbon nanotubes (SWCNTs) are unique nanomaterials with remarkable mechanical, electrical, thermal, and chemical properties [1]. However manipulation of these unique properties and consequently realization of their applications is hindered by their poor solubility and dispersibility because of strong van der Waals interactions. Moreover all known growth methods of SWCNTs produce ensemble samples of SWCNTs with different chiralities that show altogether different physical properties. Thus, solubilizing and separating SWCNTs into desired chiral configurations remains one of the most challenging task in the realization of their commercial applications. Various strategies have been proposed to disperse SWCNTs with typical conformations, that involve use of surfactants [2], aromatic compounds [3] and DNA [4]. One of the promising approach is to wrap them up in a shell of polymer. The conjugated polymers preferentially wrap nanotubes with less variation in their mean diameter, thus leading to the enrichment of specific nanotube chirality [5]. Apart from separation, composites of polymer and CNTs are useful in many applications such as photovoltaic cells, sensors, and flexible-display technologies.

This chapter describes the use of a variant of polybenzimidazole (PBI) polymer to disperse SWCNTs selectively into distinct species. PBI is one of the high-performance polymer characterized by high thermal, physical, and chemical stabilities, owing to its rigid structure [6]. Unlike other highly thermostable polymers, it is soluble in common organic solvents [7]. Recently it has been emerged as a most promising alternative to Nafion as a polymer electrolyte membrane in fuel cells. This has prompted the synthesis of different analogues of PBI with modified properties. In this chapter, we have used such an analogue called polybenzimidazole-ter-phthlate (PBI-TPH) to selectively disperse SWCNTs into distinct chiralities. Apart from solubilizing CNTs, this polymer-CNTs

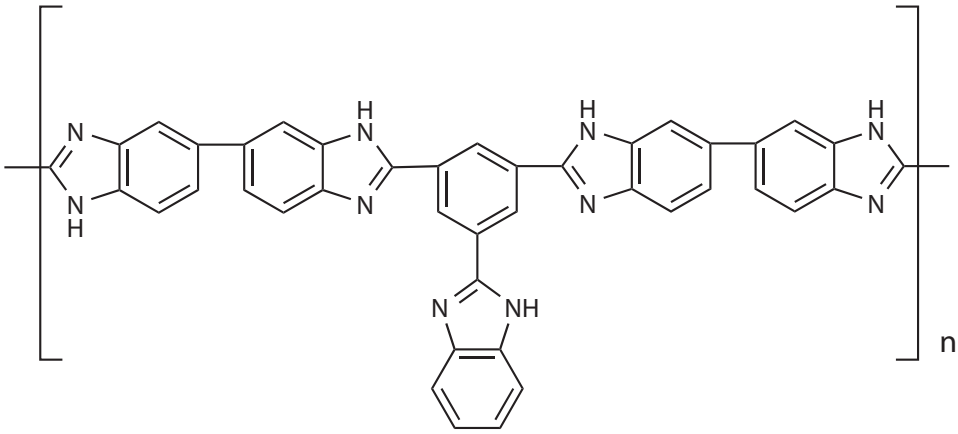

Figure 7-1. Structure of polybenzimidazole-ter-phthalate (PBI-TPH) used to disperse SWCNTs selectively.

nanoarchitecture shows unique optical and structural properties, which are explored by different characterization techniques.

7.2 Experimental

The synthesis of PBI-TPH has been described elsewhere [8] and not discussed here as it is not relevant to this thesis. The inherent viscosity of the polymer was determined in dimethylacetamide (DMAc, 0.5 g/dL) at 30 °C in a constant temperature water bath and was found to be $[\eta_i]$ = 0.97 dL/g.

The purified SWCNTs (HiPCo) were purchased from Carbon Nanotechnologies, Inc., and used as received. All the reagents, including DMAc (Aldrich), were used as received.

The polymer-SWCNTs composites were formed by mixing 5 mg of SWCNTs in 10 ml of DMAc containing 20 mg of PBI-TPH. The mixture was sonicated using a probe-type sonicator for 15 min followed by centrifugation at 15000 x g. The supernatant was used to cast the films. The films were dried in an oven at 110 °C overnight. The traces of residual solvent were removed by immersing the films in boiling water for 6 h.

The UV-vis-near IR spectra were measured by Jasco V-570 spectrophotometer. The FTIR spectra were recorded using Perkin-Elmer 16 PC FTIR spectrophotometer. Glass transition temperatures were measured using DSC Q-10 (TA) instrument. All the DSC measurements were taken in nitrogen atmosphere (flow rate- 20 ml/min) in the temperature range of 50-450 °C. The photoluminescence measurements were taken using Perkin-Elmer LS 55 spectrophotometer. The Raman spectra were recorded using micro Raman spectrometer (Horiba JY LabRAM HR 800) with an excitation wavelength 632.8 nm from a He-Ne laser.

7.3 Results and Discussion

7.3.1 UV-vis-NIR spectra

Optical spectroscopy is one of the efficient way to check the extent of monodispersion of SWCNTs with respect to electronic type, diameter, length and chiral handedness. Figure 7-2 shows the UV-vis-NIR spectra of the supernatant portions (after centrifugation) of PBI-TPH and SWCNT-PBI-TPH.

The lower wavelength peak; ~280 nm for PBI-TPH is due to $\pi \rightarrow \pi^*$ transition of the imidazole moiety and longer wavelength peaks; ~350 nm and ~410 nm are due to n $\rightarrow \pi^*$ transition [9]. At longer wavelengths, the PBI-TPH spectrum shows a very long tail which becomes prominent as the concentration of the solution increases. This feature indicates the aggregation of polymer chains due to the overlapping of polymer coils at higher concentration [9].

The UV-vis-NIR spectrum of supernatant portion of SWCNT-PBI-TPH clearly shows the changes especially in the vis-NIR region indicating effective dispersion of the SWCNTs in the mixture. The peaks are more defined, sharpened, and blue-shifted compared to polymer indicating the existence of individual SWCNTs due to the well dispersion. The absorption feature is enhanced in the UV-vis region (figure 7-3) which

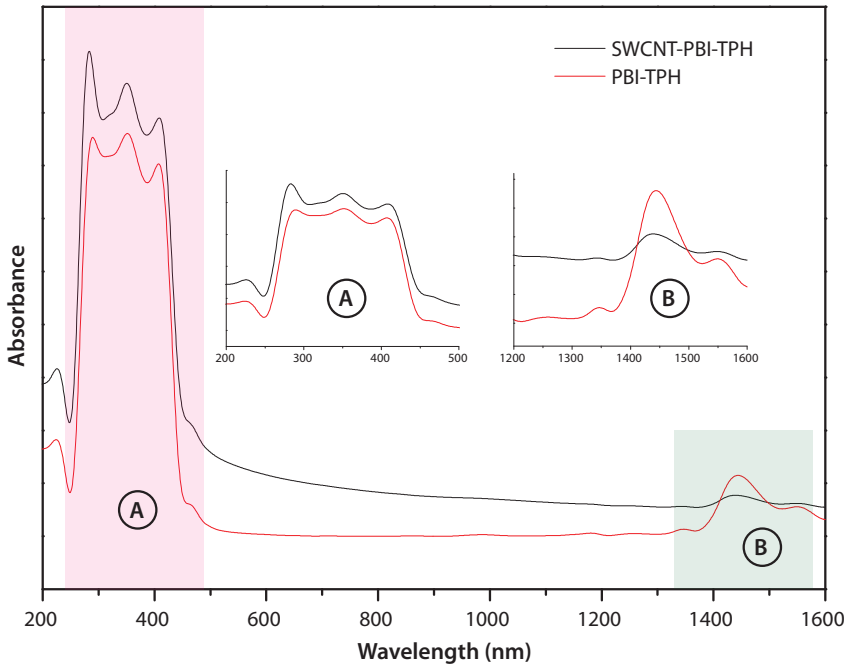

Figure 7-2. UV-vis-NIR spectra of PBI-TPH and SWCNT-PBI-TPH in DMAc (supernatant portions after centrifugation). The insets A and B show the magnified spectra in the UV-vis and NIR regions respectively.

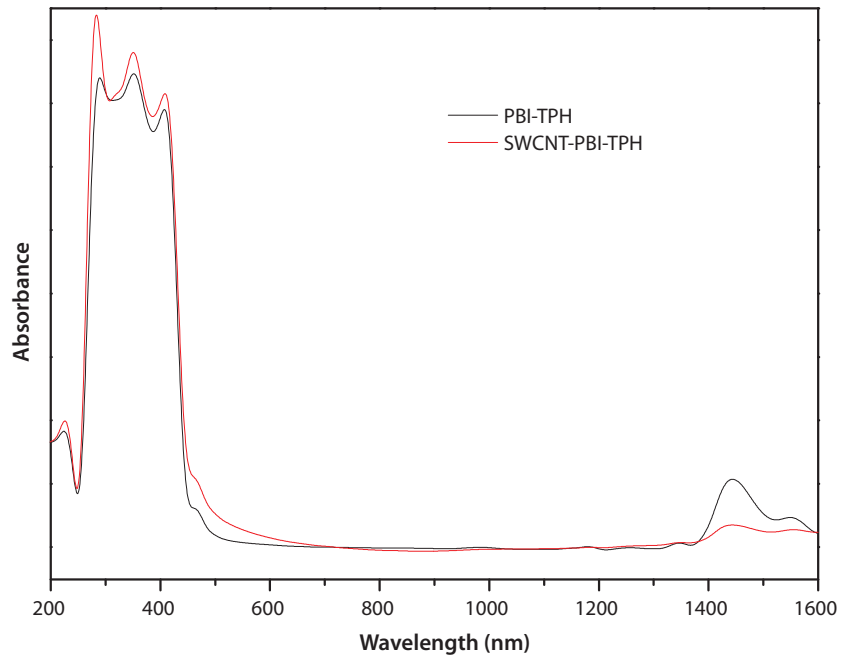

Figure 7-3. Normalized UV-vis-NIR spectra of PBI-TPH and SWCNT-PBI-TPH in DMAc (supernatant portions) after baseline correction.

can be attributed to the metallic fraction of the SWCNTs. The profound suppression of the absorption peak in the NIR region (~ 1400 nm) can be attributed to the semiconducting fraction (S_{11}) of the SWCNTs [10]. It is evident that PBI-TPH not only plays a major role in the dispersion of SWCNTs but also selectively enriches nanotubes of different (n, m) chiralities. The strong absorption features of PBI-TPH polymer makes it difficult to analyze the chirality-specific enrichment of nanotubes from the UV-vis-NIR spectra alone.

7.3.2 Fluorescence spectroscopy

Fluorescence spectroscopy is a very useful technique to measure the effectiveness of the polymer as a dispersing agent for carbon nanotubes [11]. The interaction between the polymer and carbon nanotubes depends on the different chiral configurations of the nanotubes as well as on the structure of polymer. The metallic nanotubes quench fluorescence signal by providing efficient non-radiative decay pathways to the photo-excited carriers in a nanotubes bundle. Thus the fluorescence efficiency of nanotubes strongly depends on the degree of dispersion and isolation of individual semiconducting carbon nanotubes [12].

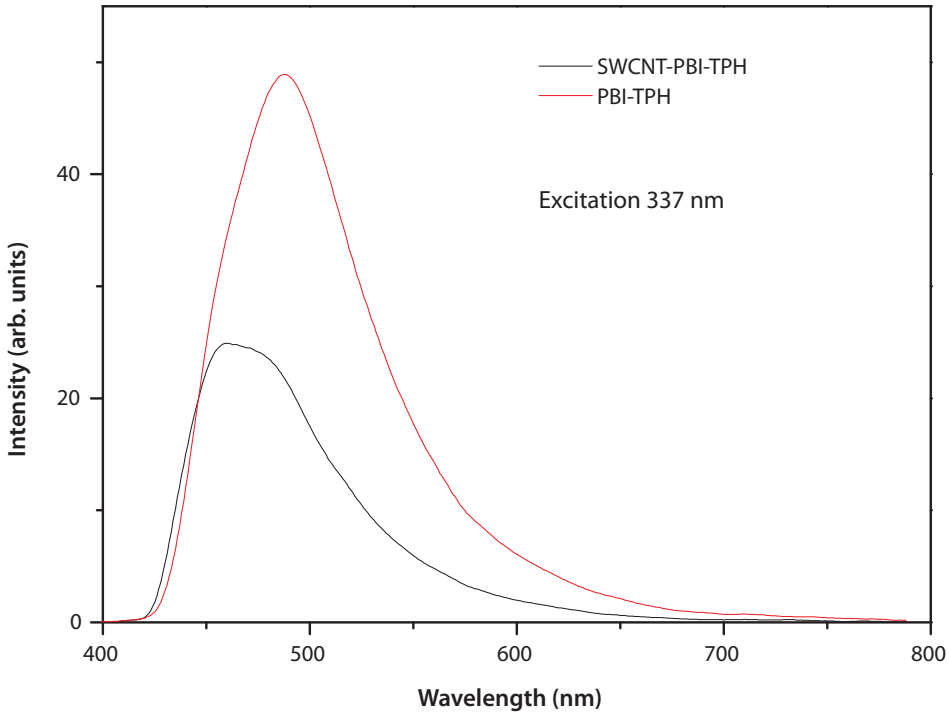

Figure 7-4. Photoluminescence spectra of supernatant allots of PBI-TPH and SWCNT-PBI-TPH in DMAc. The excitation signal was at 337 nm.

Figure 7-4 shows the photoluminescence spectra of supernatant fractions of

PBI-TPH and SWCNT-PBI-TPH in DMAc solution. The major fluorescence emission of polymers with imidazole moieties has been assigned to the emission from the excited ^1L_b state [9]. The emission spectrum of PBI-TPH show a strong peak at ~450 nm which can be assigned to the 0-0 and 0-1 transitions from the excited ^1L_b state in the benzimidazole ring of PBI-TPH [9]. It has been also shown that the presence of broad emission at higher wavelength and isoemissive point attributes the formation of excimer complex between the excited state and ground state molecules [9].

The photoluminescence spectrum of SWCNT-PBI-TPH show the quenching of the fluorescence signal of the polymer which can be attributed to the efficient energy transfer between PBI-TPH and carbon nanotubes. This suggests that polymer aggregates are in intimate contact with the nanotube sidewalls through strong π-π interactions [13]. The aromatic moieties of the polymer organize themselves around the graphene sidewalls to form a wrapping sheath through π-π interactions and thus prevent nanotube aggregation [13]. This interaction also provides an efficient pathway for the energy transfer between polymer and nanotubes where nanotubes act as energy sinkers resulting in the quenching of fluorescence signal. Figure 7-5 shows the photoluminescence spectra of PBI-TPH and SWCNT-PBI-TPH recorded at different excitation wavelengths.

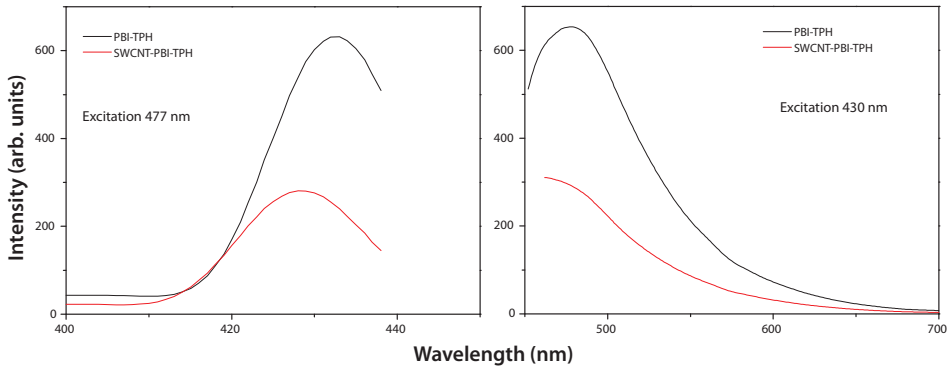

Figure 7-5. Fluorescence spectra of supernatant fractions of PBI-TPH and SWCNT-PBI-TPH in DMAc solution measured at different excitation wavelengths to understand the interaction between polymer and nanotubes.

It is evident from these spectra that nanotubes effectively quench fluorescence signal of the polymer through π-π interactions. The dependency of the fluorescence emission of polymer solution upon the excitation wavelength indicates the presence of energetically different aggregated species in the ground state [9]. Each of these species has it's own characteristic absorption and emission maxima and hence, at each different excitation wavelength, a different species is excited with its own characteristic emission.

The extent of wrapping of organic moieties along the nanotube axis varies for different diameter nanotubes; smaller diameter nanotubes being wrapped efficiently resulting in the enrichment of selective chirality [13]. The selective de-bundling of carbon nanotubes by polymer is analogous to the isolation mechanism induced by surfactant.

7.3.3 DSC analysis

Glass transition temperature, T_g is one of the important characteristics of the polymer and it provides useful information about the additives. Figure 7-6 shows the DSC thermograms of PBI-TPH and SWCNT-PBI-TPH films recorded in nitrogen atmosphere at a heating rate of 20 °C min^{-1}.

Polybenzimidazole and its structural analogues generally show high glass

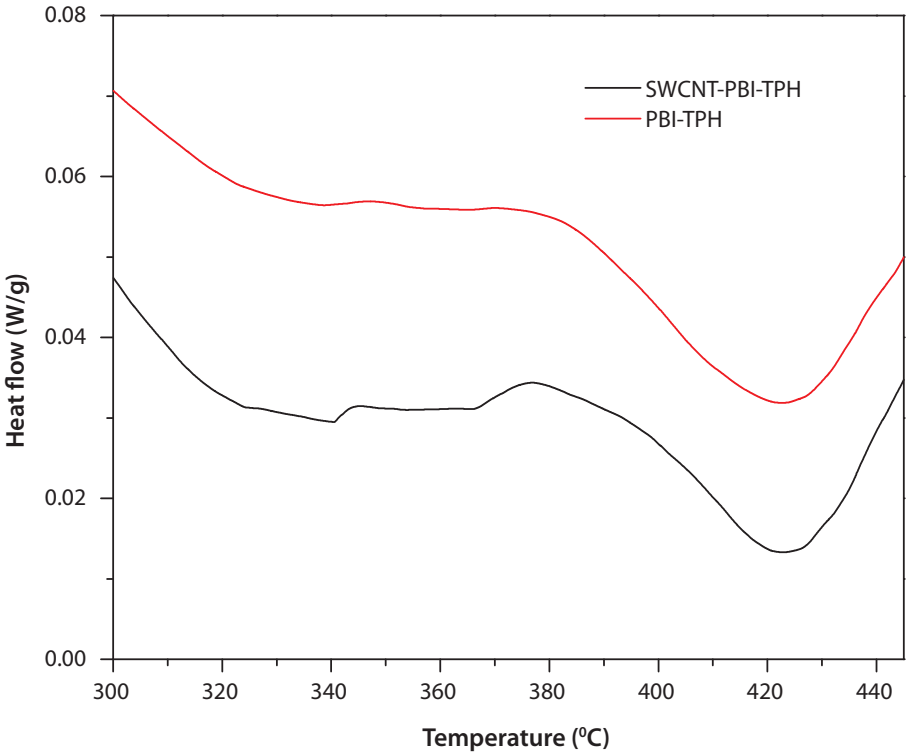

Figure 7-6. DSC thermograms of PBI-TPH and SWCNT-PBI-TPH recorded in nitrogen atmosphere with a heating rate 20 °C/min.

transition temperature owing to their rigid structure [6]. Incorporation of flexible functional groups in the side chain of the polymer with imidazole moieties usually associated with the decrease in the T_g temperature. As it can seen from the figure, the glass transition temperature for PBI-TPH is around 420 °C, a lower value than that of commercial PBI due to structural modifications.

The glass transition temperature of SWCNT-PBI-TPH is slightly higher (~424 °C) than that of polymer indicating that the addition of carbon nanotubes increases the crystallinity of the polymer. Carbon nanotubes act as a nucleating agents for crystallization to facilitate the crystallization process. Absence of any larger shifts in the values of glass transition temperature indicates that addition of SWCNTs does not disturb the polymer backbone and the interactions are of π-π type.

7.3.4 FTIR analysis

The FTIR spectra of PBI-TPH and SWCNT-PBI-TPH were recorded on the 20 μm thick films. Before the FTIR measurements, all the samples were soaked in hot water and dried at 150 °C for two days in a vacuum oven to remove any traces of solvent which is confirmed by the absence of C-H stretching at 2940 cm^{-1} for DMAc.

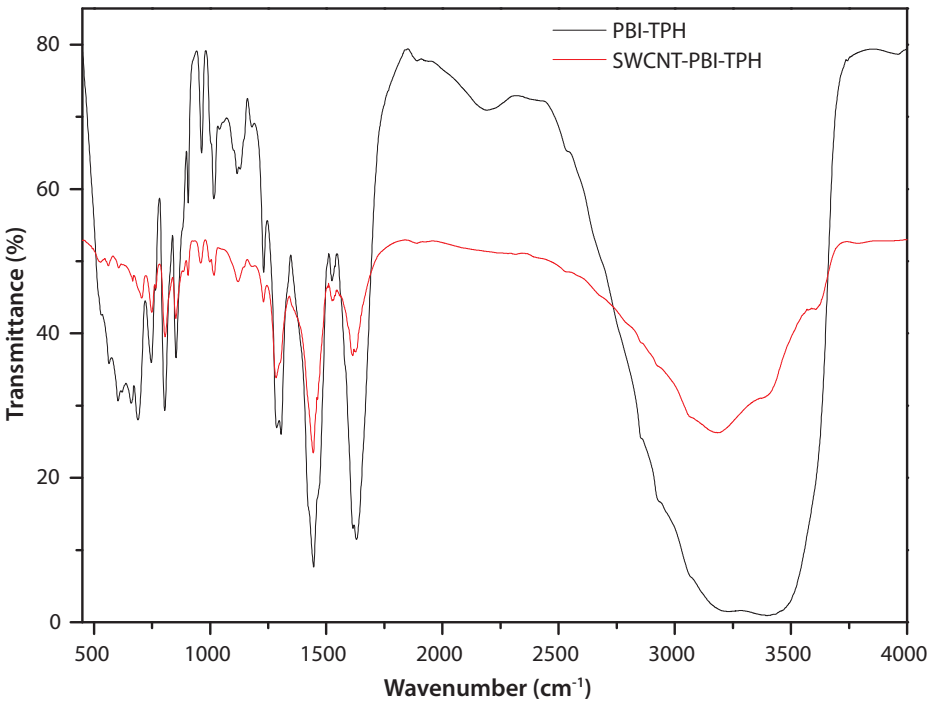

Figure 7-7. FTIR spectra of PBI-TPH and SWCNT-PBI-TPH. Addition of nanotubes shows masking of the major functional groups of polymer without any structural modifications of the polymer backbone.

Figure 7-7 shows the FTIR spectra of PBI-TPH and SWCNT-PBI-TPH. PBI-TPH shows peaks at 3415 and 3145 cm^{-1} that can be attributed to the free non-hydrogen bonded N-H stretching and self-associated N-H stretching, respectively [8].

The presence of benzimidazole group was confirmed by several characteristics bands at 1445 cm^{-1} (in plane deformation of benzimidazole) 1288 cm^{-1} (breathing mode of the imidazole ring) and peaks at 1625 cm^{-1}, 1596 cm^{-1}, and 1177 cm^{-1} for C=N stretching [8].

Figure 7-8 shows magnified FTIR spectra of PBI-TPH and SWCNT-PBI-TPH samples. Addition of carbon nanotubes results in the masking of prominent functional groups of polymer. As it can be seen from the figure 7-8, the presence of carbon nanotubes reduces the peak intensity of imidazole moieties of the polymer backbone especially in the 3000 to 3500 cm^{-1} region and 1200 to 1400 cm^{-1} region indicating the interaction

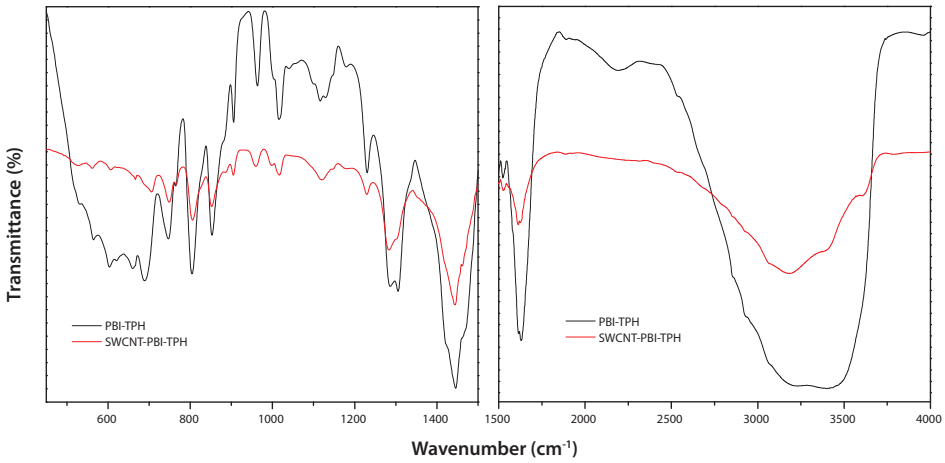

Figure 7-8. Magnified portions of FTIR spectra of PBI-TPH and SWCNT-PBI-TPH films to understand the structural interactions between polymer and nanotubes.

between aromatic organic moieties and carbon nanotubes core.

As we have already seen from the optical spectroscopy and DSC analysis, the interaction between polymer and nanotubes is believed to be π-π interaction.

7.3.5 Raman analysis

The interaction between polymer and carbon nanotubes can be conveniently studied by Raman spectroscopy. It also provides the useful information in terms of the extent of defects generated at the nanotubes ends as well as along the sidewall. The radial breathing mode (RBM) region can be conveniently used to identify the different chiralities of SWCNTs.

Figure 7-9 shows the Raman spectra of SWCNT (as received) and SWCNT-PBI-TPH (supernatant fraction) samples excited at 633 nm of wavelength. The spectra were normalized to the G-band around 1580 cm^{-1} for the sake of comparison. The spectra can be divided into four regions- 1)RBM region in the range of 150-350 cm^{-1} which is a diameter dependent; 2) the D-band in the range of 1300-1400 cm^{-1}; the disorder induced band in graphite lattice that reflects defects in CNTs, 3) the G-band in the range of 1500-1600 cm^{-1}; due to the tangential vibration of carbon atoms, and 4) the D*-band in the range of 2600-2800 cm^{-1}; the second harmonic of D-band [14].

The structural purity of the nanotubes can be estimated qualitatively by calculating the intensity ratio of D and G-bands (I_D/I_G) [14]. As it can seen from the figure 7-9, there is a significant change in the I_D/I_G ratio of SWCNT-PBI-TPH sample indicating less defects are generated and SWCNTs remain intact; in fact the wrapping of polymer along the nanotube axis efficiently enriches nanotubes with less defects.

The extent of wrapping of polymer sheath along the nanotube axis depends on the diameter of the nanotubes which can be clearly seen from the RBM region of the

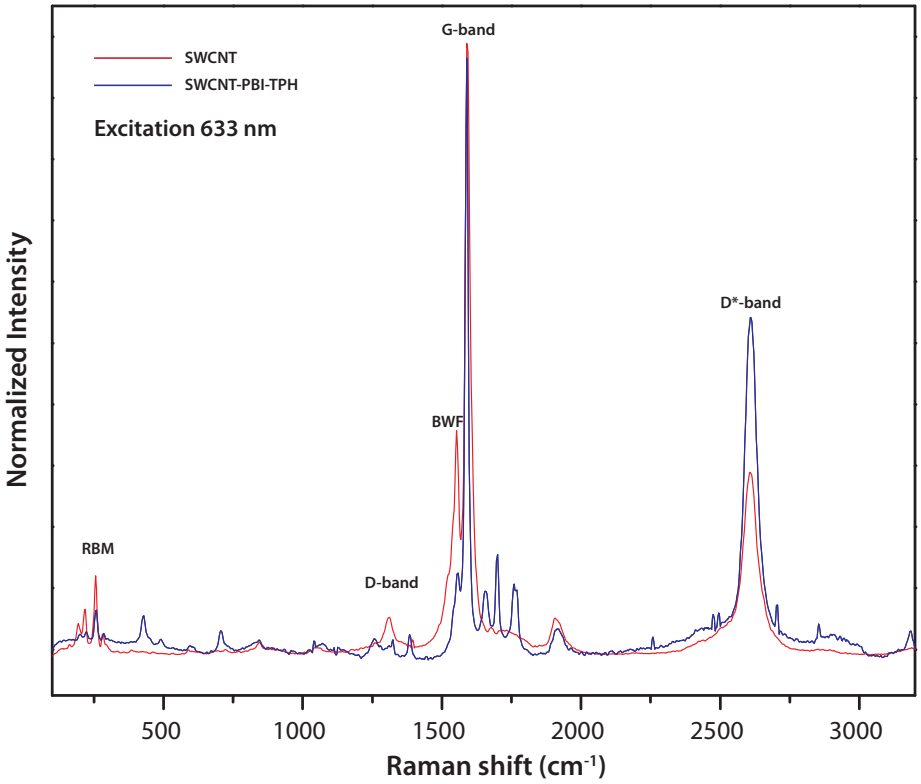

Figure 7-9. Raman spectra of SWCNT and SWCNT-PBI-TPH. The excitation wavelength was 633 nm which equally irradiates metallic as well as semiconducting fractions.

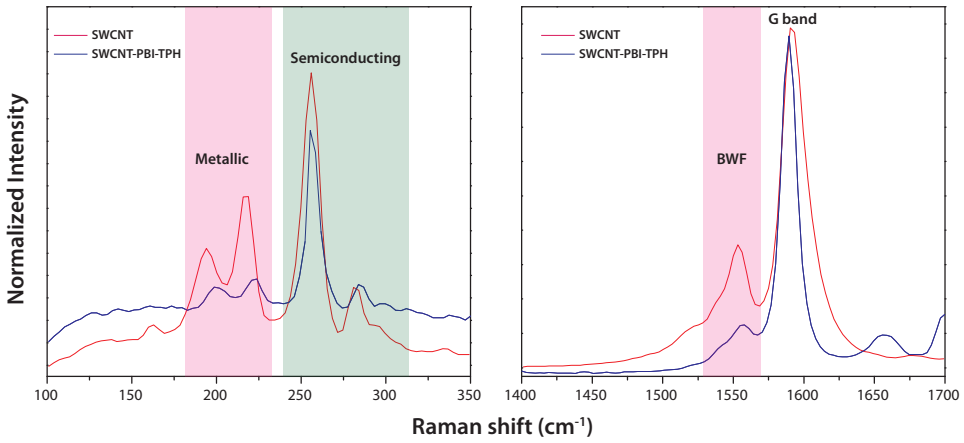

Figure 7-10. Magnified Raman spectra of SWCNT and SWCNT-PBI-TPH showing RBM and G band regions. The RBM region clearly shows the selective enrichment of semiconducting carbon nanotubes.

spectra. Figure 7-10 shows the magnified portions of RBM region and G-band region. The reduction in the peak intensity of larger diameter nanotubes around 193 cm^{-1} and 218 cm^{-1} (metallic fractions) after polymer wrapping essentially shows the enrichment of smaller diameter nanotubes. The intensity decrease can be attributed to the off-resonance effect caused by strong physisorption of polymer along the sidewalls of nanotubes. The polymer selectively wraps around smaller diameter carbon nanotubes; thus enriching the semiconducting fraction as there is no significant change in the peak intensity of 257 cm^{-1} and 282 cm^{-1} as shown in the figure 7-10.

The G-band feature can be deconvoluted into six components- one metallic, one metallic BWF, and four semiconducting components [14]. Abundant information regarding the polymer and nanotube interactions can be extracted from these components. The metallic BWF component was drastically reduced after polymer wrapping. The changes in the metallic component in the G-band can be attributed to the donation/withdrawal of electrons to metallic carbon nanotubes from polymer. The presence of aromatic moieties in the polymer backbone usually enhances the π-stacking interactions between the hexagons in the backbone and nanotubes.

7.4 Conclusions

PBI-TPH polymer has been found as a good dispersant for SWCNTs owing to the π-π interactions between the polymer and nanotubes as evident from the optical spectroscopy. The DSC and FTIR analysis suggests the structure of SWCNTs remains intact without defects after polymer wrapping. The Raman spectroscopy provided the strongest evidence of selective enrichment of smaller diameter nanotubes, thus providing a complementary method to separate nanotubes of different electronic types. A better understanding of polymer - nanotube interaction can lead to the manipulation of electronic properties of nanotubes through the separation of metallic and semiconducting carbon nanotubes.

7.5 References

1. R. Saito, G. Dresselhaus, M. S. Dresselhaus, Knovel, Physical properties of carbon nanotubes, Vol. 4, Imperial college press London, 1998.
2. V. C. Moore, M. S. Strano, E. H. Haroz, R. H. Hauge, R. E. Smalley, J. Schmidt, Y. Talmon, Nano Letters 2003, 3, 1379-1382.
3. A. Nish, J. Y. Hwang, J. Doig, R. J. Nicholas, Nature Nanotechnology 2007, 2, 640-646.
4. M. Zheng, A. Jagota, E. D. Semke, B. A. Diner, R. S. McLean, S. R. Lustig, R. E. Richardson, N. G. Tassi, Nature Materials 2003, 2, 338-342.
5. A. Nish, J. Y. Hwang, J. Doig, R. J. Nicholas, Nature Nanotechnology 2007, 2, 640-646.
6. D. Tomlin, A. Fratini, M. Hunsaker, W. Wade Adams, Polymer 2000, 41, 9003-9010.
7. M. B. Gieselman, J. R. Reynolds, Macromolecules 1992, 25, 4832-4834.
8. M. Kulkarni, R. Potrekar, R. Kulkarni, S. Vernekar, Journal of Applied Polymer Science 2010, 117, 3282-3292.
9. A. Sannigrahi, D. Arunbabu, R. M. Sankar, T. Jana, Macromolecules 2007, 40, 2844-2851.
10. S. M. Bachilo, M. S. Strano, C. Kittrell, R. H. Hauge, R. E. Smalley, R. B. Weisman, Science 2002, 298, 2361.
11. A. Star, J. F. Stoddart, D. Steuerman, M. Diehl, A. Boukai, E. W. Wong, X. Yang, S. W. Chung, H. Choi, J. R. Heath, Angewandte Chemie International Edition 2001, 40, 1721-1725.
12. M. J. O'connell, S. M. Bachilo, C. B. Huffman, V. C. Moore, M. S. Strano, E. H. Haroz, K. L. Rialon, P. J. Boul, W. H. Noon, C. Kittrell, Science 2002, 297, 593.
13. A. Nish, J. Y. Hwang, J. Doig, R. J. Nicholas, Nature Nanotechnology 2007, 2, 640-646.
14. M. Dresselhaus, G. Dresselhaus, A. Jorio, A. Souza Filho, R. Saito, Carbon 2002, 40, 2043-2061.

CHAPTER 8

Solubilizing carbon nanotubes with long-chain polyimides.

Implementation of real-world application of carbon nanotubes is difficult partly because of the lack of universal solvent for them. This chapter describes the solubilities of single-walled carbon nanotubes when wrapped through Pi-conjugation with a polyimide chain synthesized from cardanol- a major constituent of Cashew Nut Shell Liquid. The composites were soluble in aprotic polar solvents such as NMP, DMAc as well as in less polar solvents such as chloroform and THF. The presence of pendant pentadecyl chain into the polymer back bone leads to an increased solubility. The composite was characterized by DSC, TGA, DMA, and XRD.

8.1 Introduction

Single-walled carbon nanotubes (SWCNTs) are unique nanostructures having remarkable electrical, mechanical, thermal, and chemical resistance properties [1]. They are the wonder materials of the modern technology and science. A wide range of applications in diverse areas such as transistors [2], logic gates [3], interconnects [4], conductive films [5], filed emission sources [6], scanning probes [7], infrared emitters [8], sensors [9], mechanical reinforcement [10], energy storage devices [11] and catalytic supports [12], etc. have been envisioned for nanotubes. However, implementation of real-world applications of carbon nanotubes is difficult because of the lack of universal solvent, thus hampering the manipulations of their many excellent properties. Solubilizing and purifying SWCNTs is one of the most challenging hurdle in their investigation and applications.

Moreover, synthesis of SWCNTs usually yields the batches that very widely in diameter leading to different chiral configurations that show either semiconducting or fully metallic behavior. A monodispersity with respect to electronic type, diameter, length and chiral handedness is required for their implementation in diverse applications. Recently there have been several efforts to solubilize and isolate SWCNTs using surfactant molecules [13], biomolecules [14], pyrene [14], and porphyrin derivatives [16]. Many polymers have also been reported to disperse SWCNTs in water or organic solvents [17]. An ideal dispersant for nanotubes should exhibit scalability, compatibility with SWCNTs with different diameters and lengths, should be nondestructive- able to preserve or enhance the intrinsic properties of nanotubes, and most importantly it should be affordable. In this context, aromatic polymers show remarkable efficiency in the dispersion of certain nanotube species with a high degree of selectivity owing to their ability to form unique interactions with nanotubes through wrapping [18].

This chapter describes the solubilization and isolation of SWCNTs with the help of polyimide chain that imparts solubility of nanotubes not only in aprotic polar solvents such as NMP, DMAc but also in less polar solvents such as chloroform and THF. Polyimide is an important class of high-performance polymers which show excellent

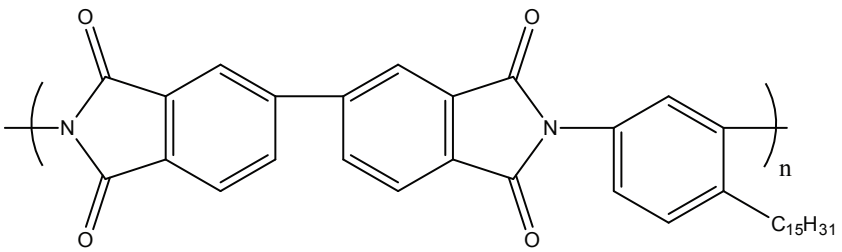

Figure 8-1. Monomer of 3, 3', 4, 4'- biphenyltetracarboxylic dianhydried (BPDA); a class of aromatic polyimide used to solubilize carbon nanotubes in different organic solvents.

chemical and thermal stabilities [19]. The polyimide- 3, 3', 4, 4'- biphenyltetracarboxylic dianhydried (BPDA), used to solubilize nanotubes was synthesized from cardanol- a

major constituent of cashew nut shell liquid (CSNL) [20]. The naturally abundant CSNL not only serves as an cheapest source of raw material but also introduces a pendant pentadecyl chain into the polymer backbone rendering the otherwise chemically resistant polymer soluble in wide variety of organic solvents. This pentadecyl chain also helps in solubilizing carbon nanotubes through effective wrapping along the nanotube axis facilitating the interaction of aromatic moieties of polymer and nanotubes through Pi-conjugation. The SWCNT-BPDA composite was characterized by optical spectroscopy, DSC, TGA, XRD, DMA, and Raman spectroscopy.

8.2 Experimental

The synthesis characterization of BPDA polymer has been described elsewhere [20]. The purified SWCNTs (HiPCo) were purchased from Carbon Nanotechnologies, Inc., and used as received. All the organic solvents, including DMAc (Aldrich), NMP (Aldrich), chloroform and tetrahydrofuran (THF) (Loba Chemie) were vacuum distilled before use.

The polymer-SWCNTs composites were formed by mixing 2 wt% of SWCNTs in 10 ml each of DMAc, NMP, $CHCl_3$, and THF containing 20 mg of BPDA. The mixture was sonicated using a probe-type sonicator for 15 min followed by centrifugation at 15000 x g. The supernatant was used to cast the films. The films were dried in an oven at 110 °C overnight.

The Vis-near IR spectra were measured by Jasco V-570 spectrophotometer. Glass transition temperatures were measured using DSC Q-10 (TA) instrument. All the DSC measurements were taken in nitrogen atmosphere (flow rate- 20 ml/min) in the temperature range of 50-450 °C. The Raman spectra were recorded using micro Raman spectrometer (Horiba JY LabRAM HR 800) with an excitation wavelength 632.8 nm from a He-Ne laser. Thermogravimetric analysis (TGA) was performed on Perkin-Elmer TGA-7 analyzer at a heating rate of 10 °C/min in nitrogen atmosphere. Dynamic mechanical analysis (DMA) was performed using Rheometrics Dynamic Mechanical Analyzer IIIE, in the tensile mode. The dynamic responses were tested in the temperature range of 25 - 300 °C at a frequency of 10 rad/s, and 0.02% strain in the auto-strain mode. XRD measurements were performed using Rigaku model Dmax 2500 X-ray diffractometer with Cu K_α radiation of wavelength 1.54 Å and energy 8.05 keV. Surface morphologies were studied by atomic force microscopy (AFM) with a nanoscope IIIa controller by Digital Instruments, Santa Barbara, CA. Hyperchem was used to perform molecular mechanics simulations using MM3 force field.

8.3 Results and Discussion

8.3.1 Vis-NIR spectra

Figure 8-2 shows the Vis-NIR spectra of supernatant fractions of SWCNT-BPDA sample in DMAc, NMP, $CHCl_3$ and THF solvents. The supernatant fractions clearly show the well resolved absorption bands, characteristic of the dispersed nanotubes, in

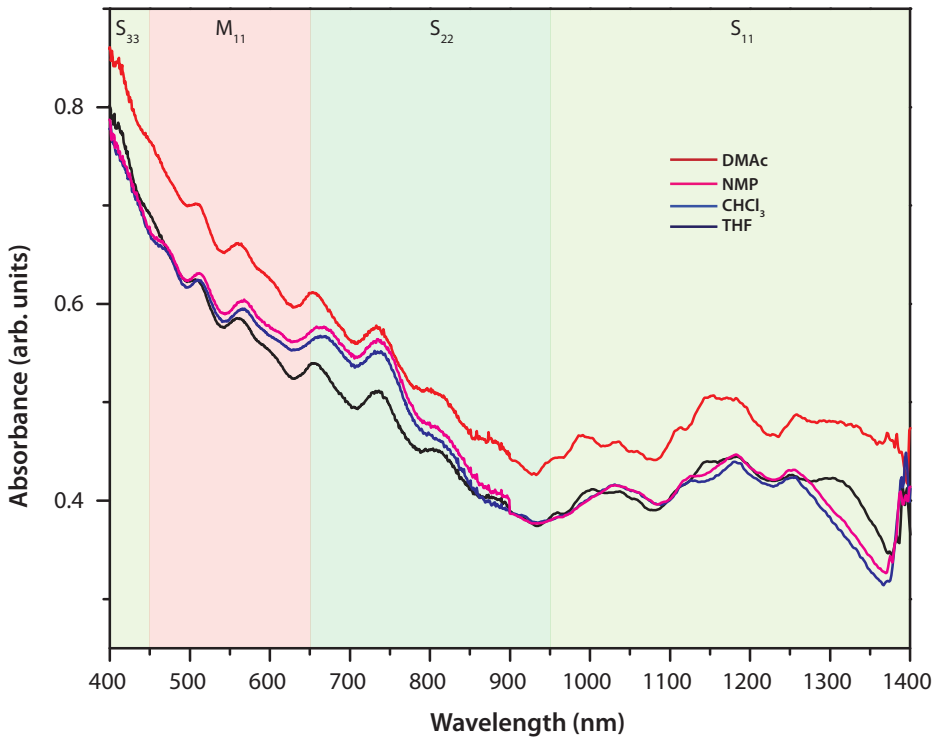

Figure 8-2. Absorbance spectra of supernatant fraction of SWCNT-BPDA in different solvents-DMAc, NMP, $CHCl_3$, and THF. Note: M_{11} = first-order optical transitions for metallic SWCNTs; S_{11}, S_{22} and S_{33} = first-order, second-order and third-order optical transitions for semiconducting SWCNTs respectively.

the 400-1400 nm region, implying effective dispersion of SWCNTs not only in aprotic polar solvents like DMAc and NMP but also in less polar solvents like chloroform and THF. The absorption of the semiconducting nanotubes in the near IR region shows the first transition, from the first valence to the first conduction band, $V_1 \rightarrow C_1$ (S_{11}) [21]. The metallic carbon nanotubes do not have a bandgap, but they have a dispersed van Hove singularity. The metallic nanotubes show absorption at the smaller wavelengths; i.e. in the blue to UV region (M_{11}) [22]. At intermediate levels of wavelengths which quite overlap in the visible region, semiconducting nanotubes absorb where second valence (V_2) to second conductive level (C_2) energy band transitions occur (S_{22}) [23].

It seems that a change in the solvent polarity affects the photo absorption of nanotubes with more polar solvent, nanotubes exhibit blue shift. It can be speculated that the long pentadecyl chain of BPDA helps in effective wrapping around the nanotube axis inducing the alignment of rigid aromatic moieties of the polymer backbone along the nanotube surface in order to maximize the interaction between π-bonds.

The wrapping of polymer along the nanotube surface is more prominent in the smaller diameter nanotubes as they are more reactive which results in the slight enrichment of semiconducting nanotubes. The polarity of a solvent (DMAc and NMP)

also seems to help in the dispersion of carbon nanotubes. A film was cast from the supernatant allot of SWCNT-BPDA in DMAc and was used for further analysis.

8.3.2 AFM

The extent of individual dissolution of the SWCNTs was further confirmed by

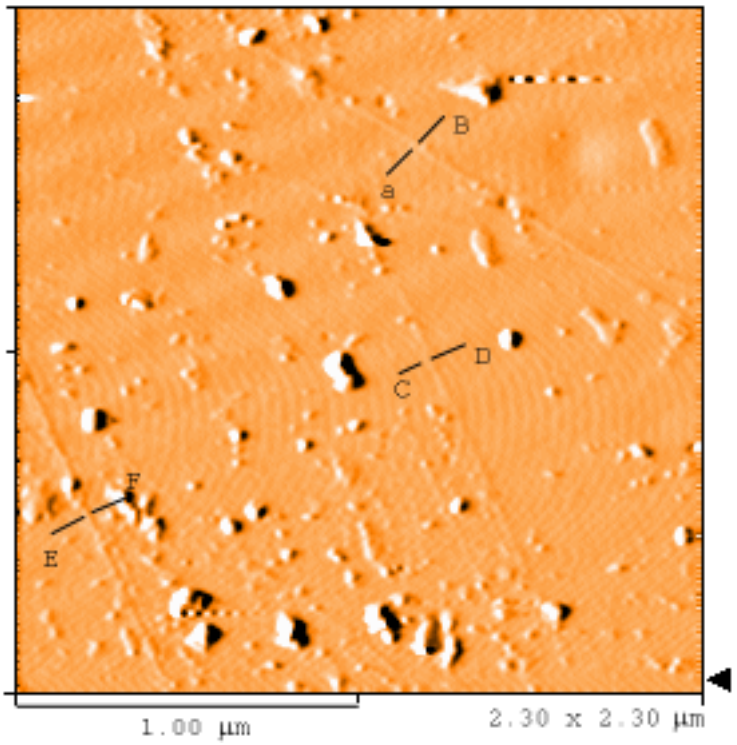

Figure 8-3. Typical AFM image of supernatant solution of SWCNT-BPDA in DMAc taken after it was cast and dried on Si wafer, and the height profiles of nanotubes at three different locations were measured.

atomic force microscopy. Few drops of supernatant solution of SWCNT-BPDA in DMAc were cast and dried on Si wafer.

Figure 8-3 shows a typical AFM image of SWCNT-BPDA supernatant in DMAc. The top heights of the nanotubes measured at different points were 2.0-2.4 nm indicating the individually dispersed nanotubes wrapped in the polymer matrix.

8.3.3 DSC analysis

BPDA belongs to polyimide family- a class of high-performance polymers which shows excellent thermo-oxidative stability, chemical resistance and mechanical strength [20]. Analogues of polyimides are generally insoluble in organic solvents and exhibit high glass transition temperatures which imposes serious processing difficulties, thus hampering their implementation in various applications [23]. However, BPDA inherits

a long pentadecyl chain in its backbone from cardanol through the synthetic route. This pentadecyl chain lowers the glass transition temperature of the polymer by weakening its intermolecular interactions bringing more disorderedness to the backbone [20].

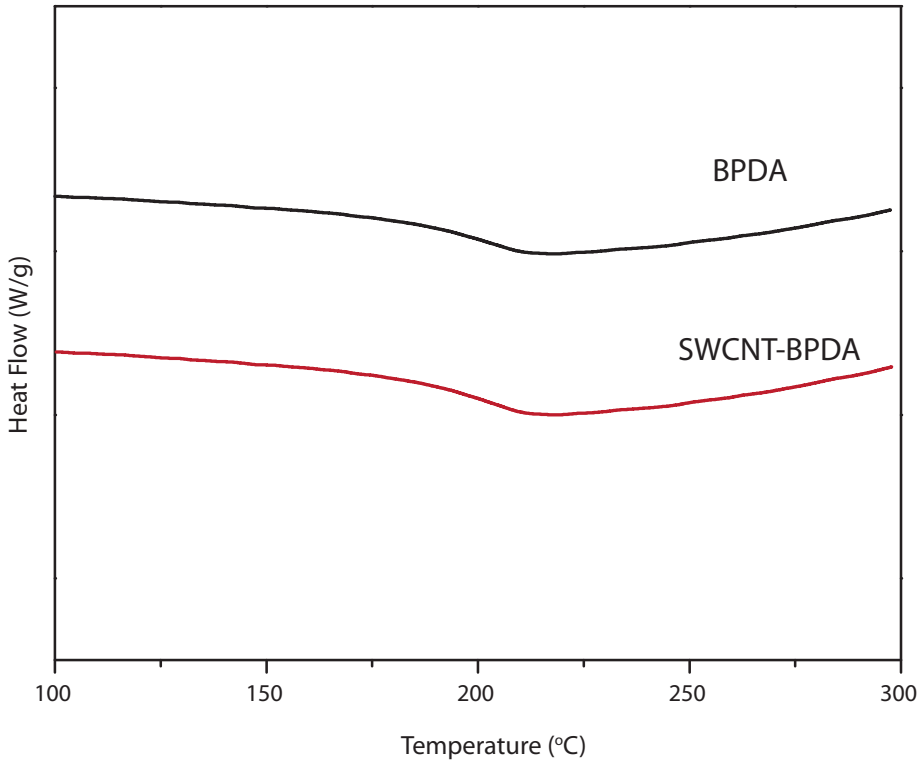

Figure 8-4. DSC thermograms of BPDA and SWCNT-BPDA (supernatant of DMAc) recorded in nitrogen atmosphere at a heating rate of 10 °C/min.

Figure 8-4 shows the DSC thermograms of BPDA polymer and SWCNT-BPDA film that was cast from the supernatant fraction of DMAc solution. As it can be seen from the figure, the glass transition temperature of BPDA is around 210 °C; a much lower value than those of polyimides analogues. This lowering of T_g value can be attributed to the increase in free volume due to pendant pentadecyl chain.

The DSC curve of SWCNT-BPDA doesn't show any significant difference from that of BPDA except a slight upshift in the glass transition temperature value. The addition of nanotubes to the polymer backbone increases its crystallinity without damaging its structural intactness. The pentadecyl chain forms wrapping sheath along the nanotubes sidewalls thus exposing the aromatic moieties of polymer to the graphene lattice to form π-stacking interactions. These π-π interactions induces solubilization and isolation of nanotubes [23].

8.3.4 TGA analysis

Figure 8-5 shows the thermogravimetric analysis of SWCNT-BPDA (DMAc

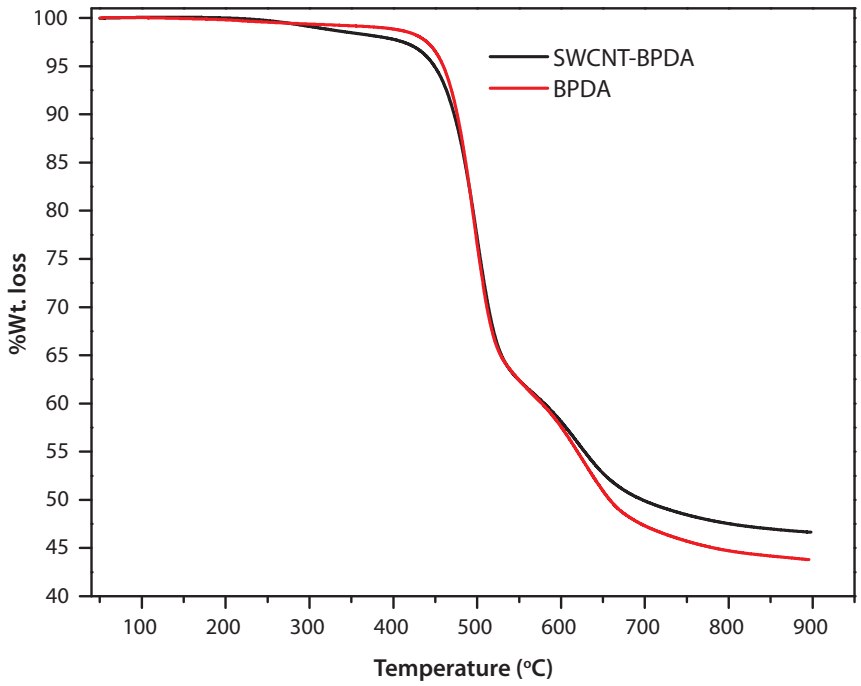

Figure 8-5. Thermogravimetric curves of SWCNT-BPDA and BPDA measured at a heating rate of 10 °C/min in nitrogen atmosphere.

supernatant) and BPDA recorded at a heating rate of 10 °C/min in nitrogen atmosphere. BPDA show excellent thermal stability upto 450-480 °C in nitrogen atmosphere. However, it shows two-stage weight loss; first one around 500 °C and the second one was around 620 °C. The first stage weight loss was due to the decomposition of pendant alkyl groups while the second stage was due to the structural decomposition of polyimide backbone. The addition of carbon nanotubes to the polymer backbone results in slightly more weight loss during initial decomposition around 450 °C. The first weight loss due to the loss of pentadecyl chain is preserved in the SWCNT-BPDA composite. However, the SWCNT-BPDA show much less weight loss in the second stage, most possibly preserving the polymer backbone. The pentadecyl chain is believed to wrap around carbon nanotubes and align the aromatic moieties of the polymer backbone along the graphene lattice, forming strong π-π interactions.

8.3.5 XRD

Figure 8-6 shows the XRD spectra of SWCNT-BPDA and BPDA samples. The polymer has a semi-crystalline nature which is reflected in the peaks at the lower angles. The BPDA polymer is believed to form stack-like structure arranged in a helical fashion [20]. This structural aspect shows XRD peaks in the lower angle region. This feature is

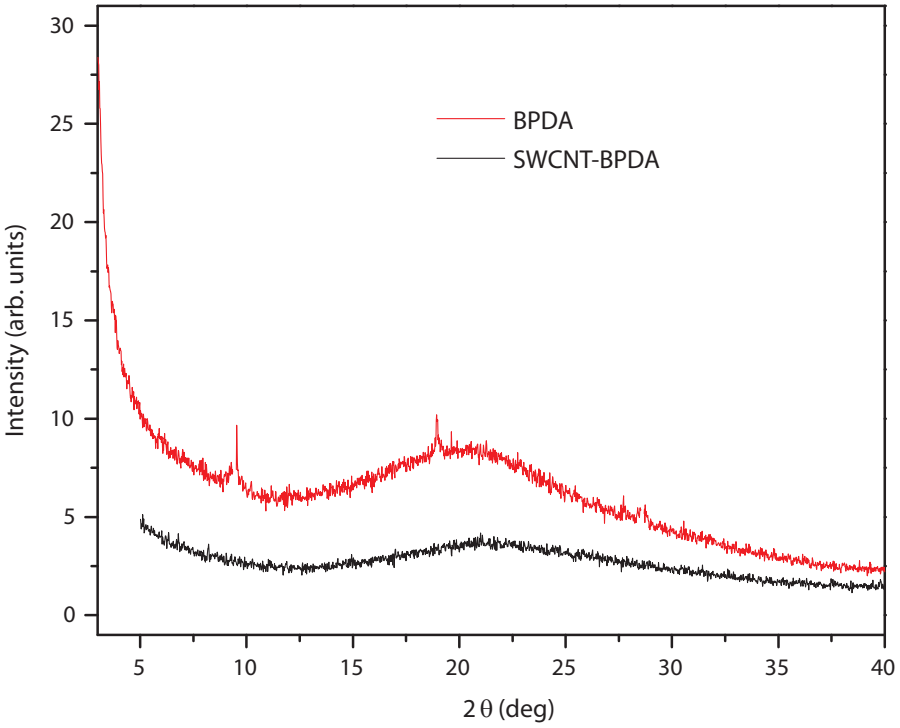

Figure 8-6. XRD spectra of BPDA and SWCNT-BPDA samples. The addition of carbon nanotubes to the polymer backbone doesn't introduce any structural changes.

believed to improve pretilt angle, making such polyimides potentially useful as films for alignment layers in the liquid crystal display devices.

The addition of carbon nanotubes to the polymer backbone does not significantly alter the crystallinity or structural parameters of the polymer. Hence, the interaction is believed to be happened in a non-covalent way through π-π interactions.

8.3.6 Dynamic mechanical analysis (DMA)

DMA measures the mechanical properties of materials as a function of time, temperature, and frequency. The technique is useful in the determination of various parameters such as T_g of a highly cross-linked polymer, modulus under variety of conditions, creep experiments, and stress-strain measurements [24].

Figure 8-7 shows the storage modulus of SWCNT-BPDA and BPDA measured at different temperatures. The storage modulus is quite same for both the samples around and slightly above the glass transition temperature. But at lower temperature, the storage modulus of SWCNT-BPDA increased drastically. The increase in the dynamic modulus can be ascribed to the high aspect ratio of carbon nanotubes and also to the strong π-π interaction between the aromatic moieties of the polymer backbone and graphitic sidewalls of the nanotubes [25]. As we have already seen this π-stacking interaction is

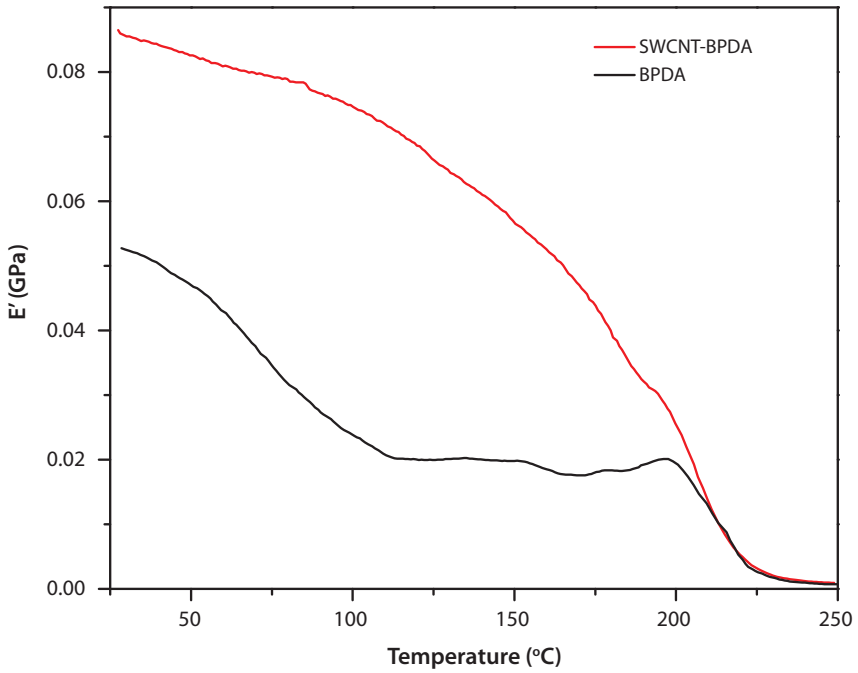

Figure 8-7. Storage modulus of SWCNT-BPDA and BPDA. Addition of carbon nanotubes to the polymer backbone enhances their mechanical properties.

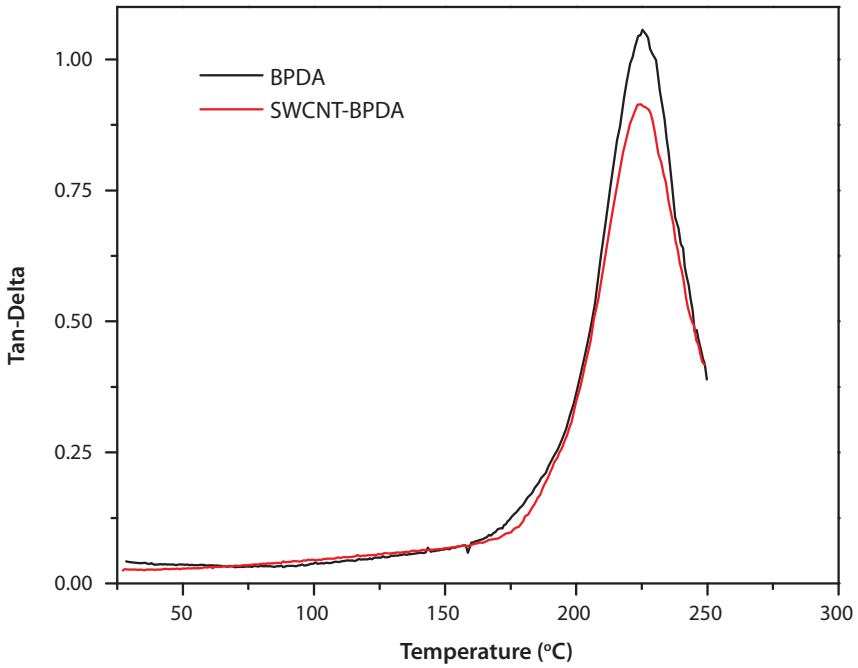

Figure 8-8. Tan δ (phase angle) vs temperature plot for SWCNT-BPDA and BPDA. There is no change in the Tg value of composite.

the main reason for the solubilization and isolation of carbon nanotubes in a variety of organic solvents. The polymer matrix efficiently transfers load to the carbon nanotubes network, which have unique mechanical properties, resulting in the mechanical reinforcement [26].

The storage modulus of BPDA polymer show transition around 110 °C which can be ascribed to the changes in the confirmations of polymer chains.

Figure 8-8 shows the phase angle variation with respect to temperature for SWCNT-BPDA and BPDA samples. The reduction in the tan δ peak intensity of SWCNT-BPDA indicates the increase in the crystallinity of the BPDA polymer matrix which is quite consistent with the DSC results.

8.3.7 Raman spectroscopy

The interactions between polymer and carbon nanotubes were followed by Raman spectroscopy. Figure 8-9 shows the Raman spectra of SWCNT (as received) and

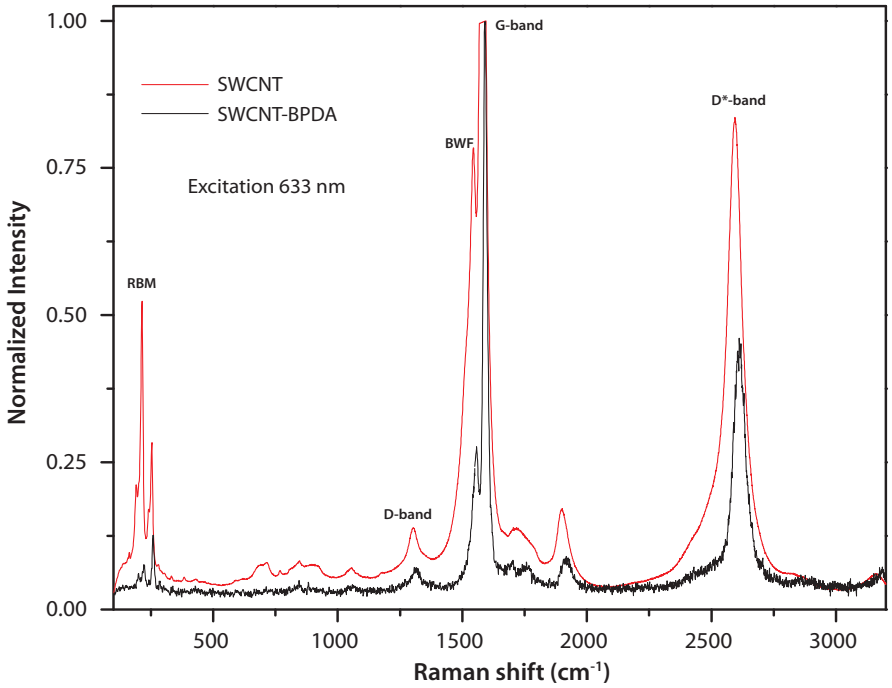

Figure 8-9. Raman spectra of SWCNT-BPDA and SWCNT recorded with a excitation wavelength 633 nm. The spectra are normalized to the G-band intensity.

SWCNT-BPDA (supernatant fraction of DMAc) samples excited at 633 nm of wavelength. The spectra were normalized to the G-band around 1580 cm^{-1} for the sake of comparison. The spectra can be divided into four regions- 1) RBM region in the range of 150-350 cm^{-1} which is a diameter dependent; 2) the D-band in the range of 1300-1400 cm^{-1}; the disorder induced band in graphite lattice that reflects defects in CNTs, 3) the G-band in

the range of 1500-1600 cm^{-1}; due to the tangential vibration of carbon atoms, and 4) the D*-band in the range of 2600-2800 cm^{-1}; the second harmonic of D-band [27].

The structural purity of the nanotubes can be estimated qualitatively by calculating the intensity ratio of D and G-bands (I_D/I_G) [27]. There is a significant change in the I_D/I_G ratio of SWCNT-BPDA sample indicating less defects are generated and the nanotubes retain their structural intactness.

The interaction between the nanotubes and polymer usually results in the upshifting of the peaks. It has been reported that π-π interactions can cause considerable upshift in the RBM region [28]. As it can be seen from the figure 8-9, the RBM peaks of SWCNT-BPDA are upshifted reflecting the homogeneous dispersion of SWCNTs.

The wrapping of the SWCNTs by polymer is also evident from the shift in the D*-band position. The effect of stress or strain on the nanotubes by the surrounding atmosphere induces upshift in the peak position of D* band. Figure 8-9 shows a considerable upshift in the D*-band which can be attributed to a small hydrostatic compression force on the SWCNTs.

The reduction in the peak intensities of metallic nanotubes at ~193 cm^{-1} and ~218 cm^{-1} shows that the wrapping of polymer through π-π interactions selectively enriches smaller diameter semiconducting carbon nanotubes.

8.4 Conclusions

BPDA- a polymer with a pentadecyl chain, has been found to act as a good dispersant for the solubilization and isolation of carbon nanotubes in a aprotic polar as well as less polar organic solvents. Optical spectroscopy and AFM were used to study the degree of solubilization. The organic moieties in the polymer backbone form strong π-π interactions with the graphene sidewalls of the nanotubes. Thermal analysis including TGA and DSC showed improved thermal and chemical stabilities of polymer after nanotubes addition. DMA showed the excellent mechanical reinforcement of the polymer film by nanotubes through π-π interactions. Raman spectroscopy provided strong evidence of the enrichment of semiconducting carbon nanotubes with smaller diameters.

8.5 References

1. R. Saito, G. Dresselhaus, M. S. Dresselhaus, Knovel, Physical properties of carbon nanotubes, Vol. 4, Imperial college press London, 1998.
2. R. Martel, T. Schmidt, H. Shea, T. Hertel, P. Avouris, Applied Physics Letters 1998, 73, 2447.
3. V. Derycke, R. Martel, J. Appenzeller, P. Avouris, Nano Letters 2001, 1, 453-456.
4. F. Kreupl, A. P. Graham, G. Duesberg, W. Steinhögl, M. Liebau, E. Unger, W. Hönlein, Microelectronic Engineering 2002, 64, 399-408.
5. Z. Wu, Z. Chen, X. Du, J. M. Logan, J. Sippel, M. Nikolou, K. Kamaras, J. R. Reynolds, D. B. Tanner, A. F. Hebard, Science 2004, 305, 1273.
6. S. Fan, M. G. Chapline, N. R. Franklin, T. W. Tombler, A. M. Cassell, H. Dai, Science 1999, 283, 512.
7. H. Dai, J. H. Hafner, A. G. Rinzler, D. T. Colbert, R. E. Smalley, 1996.
8. M. Freitag, J. Chen, J. Tersoff, J. C. Tsang, Q. Fu, J. Liu, P. Avouris, Physical review letters 2004, 93, 76803.
9. J. Kong, M. G. Chapline, H. Dai, Advanced Materials 2001, 13, 1384-1386.
10. J. N. Coleman, U. Khan, Y. K. Gun'ko, Advanced Materials 2006, 18, 689-706.
11. G. Che, B. B. Lakshmi, E. R. Fisher, C. R. Martin, Nature 1998, 393, 346-349.
12. N. Rajalakshmi, H. Ryu, M. Shaijumon, S. Ramaprabhu, Journal of power sources 2005, 140, 250-257.
13. V. C. Moore, M. S. Strano, E. H. Haroz, R. H. Hauge, R. E. Smalley, J. Schmidt, Y. Talmon, Nano Letters 2003, 3, 1379-1382.
14. E. Katz, I. Willner, ChemPhysChem 2004, 5, 1084-1104.
15. W. Z. Yuan, J. Z. Sun, Y. Dong, M. Häussler, F. Yang, H. P. Xu, A. Qin, J. W. Y. Lam, Q. Zheng, B. Z. Tang, Macromolecules 2006, 39, 8011-8020.
16. V. Georgakilas, K. Kordatos, M. Prato, D. M. Guldi, M. Holzinger, A. Hirsch, J. Am. Chem. Soc 2002, 124, 760-761.
17. M. Islam, E. Rojas, D. Bergey, A. Johnson, A. Yodh, Nano Letters 2003, 3, 269-273.
18. A. Nish, J. Y. Hwang, J. Doig, R. J. Nicholas, Nature Nanotechnology 2007, 2, 640-646.
19. D. J. Liaw, F. C. Chang, M. Leung, M. Y. Chou, K. Muellen, Macromolecules 2005, 38, 4024-4029.
20. N. V. Sadavarte, M. R. Halhalli, C. Avadhani, P. P. Wadgaonkar, European Polymer Journal 2009, 45, 582-589.
21. S. M. Bachilo, M. S. Strano, C. Kittrell, R. H. Hauge, R. E. Smalley, R. B. Weisman, Science 2002, 298, 2361.
22. M. S. Strano, C. A. Dyke, M. L. Usrey, P. W. Barone, M. J. Allen, H. Shan, C. Kittrell,

R. H. Hauge, J. M. Tour, R. E. Smalley, Science 2003, 301, 1519.

23. B. Li, T. He, M. Ding, Polymer 1999, 40, 789-794.
24. Z. Jin, K. Pramoda, G. Xu, S. H. Goh, Chemical Physics Letters 2001, 337, 43-47.
25. M. Moniruzzaman, K. I. Winey, Macromolecules 2006, 39, 5194-5205.
26. D. Qian, E. C. Dickey, R. Andrews, T. Rantell, Applied Physics Letters 2000, 76, 2868.
27. M. Dresselhaus, G. Dresselhaus, A. Jorio, A. Souza Filho, R. Saito, Carbon 2002, 40, 2043-2061.
28. M. Okamoto, T. Fujigaya, N. Nakashima, Advanced Functional Materials 2008, 18, 1776-1782.

CHAPTER 9

Carbon nanotubes- Polyvinylidene fluoride (PVDF) composites: Structural, mechanical and electrical characterization.

A matrix composite prepared by blending polyvinylidene fluoride with very small amounts of multiwalled carbon nanotubes (1-6%) shows enhanced thermal stability along with a more than 100 % increase in modulus above the glass transition temperature. The addition of small amount of carbon nanotubes dramatically alters the structural, mechanical and electronic properties by modifying the polymer interface. The composite was characterized by dynamic mechanical analysis, differential scanning calorimetry, X-ray diffraction, impedance measurements, DC conductivity, and scanning electron microscopy.

9.1 Introduction

Recent research in carbon nanotube (CNT) based composites has led to an intense interest in the science of dispersing large aspect ratio nanotubes (length/ diameter >1000) with a view to optimizing electrical, thermal and mechanical properties of the composite [1, 2]. Previously, carbon fibers have been widely used as reinforcing elements in polymers and other matrices for several applications. CNTs are known to possess a higher aspect ratio, excellent mechanical properties and lower density relative to the corresponding properties in carbon fibers. For example, the tensile strength and modulus of CNT are of the order of 11 - 200 GPa and 270 GPa – 1 TPa, respectively [3], and their amazing actuation properties have been also been demonstrated recently [4].

However, they have limited elastic compliance and hence processing them in a polymeric matrix would facilitate their applications as actuators over large areas. Consequently, many polymers have been tested for realizing CNT-based composites during the last few years. For example, electrical and optical properties of single walled carbon nanotubes/poly (3-octylthiophene) composites were studied by Kymakis and coworkers [4]. They have reported that as the nanotubes concentration increases from 0 to 20 wt%, the conductivity of the cast films increases by 5 orders of magnitude. Electrospinned composites of polyurethane [5], polyaniline/poly (ethylene oxide) [6] and polyvinylidene fluoride have all shown improved electrical conductivity. Electrospinning has been used as a method for the preparation of CNT composites for polyethylene [7] and polysulphones [8]. Rheological study of polycarbonate multiwalled carbon nanotubes composites were carried out by Potschke et al [11], where, the viscosity was found to increase above a percolation limit of 2% along with a concomitant increase in the storage modulus. This interesting observation was explained on the basis of a very high aspect ratio of the carbon nanotubes [9]. Recently a remarkable in situ preparation of Nylon-CNT composites showed that the morphology and properties can be altered by tailoring the CNT-polymer interfacial interactions [10]. Thus, the preparation and characterization of these polymer matrix composites offer unprecedented opportunity to create new hybrid materials combining the elegant flexibility and light weight of polymers with unique actuation behavior of CNTs [4].

Electroactive polymers are especially significant for making CNT composites due to their unique capabilities and the actuator response of the composite can be separately tuned both by the medium and by the dimensions of CNTs, and there is always a possibility of observing synergistic effects. Polyvinylidene fluoride (PVDF) is one of the most studied polymers because of its special characteristics like high dielectric strength, smaller values of relative permittivity, wide dynamic range for actuation and transduction, and an acoustic compliance close to that of water leading to many potential applications in piezoelectric and pyroelectric devices. Among all the polymeric materials investigated, PVDF exhibits the largest piezoelectric and pyroelectric coefficients [1-4] and consequently it has many applications in non-linear optics and microwave transducers. Further it is also a biocompatible polymer since it is non-rejectable in human tissues. Its excellent elastic compliance can offset the poor elastic compliance of CNT and in return, CNT can alleviate many processing difficulties

of PVDF arising due to their poor electromechanical coupling and relatively weak force generation capability.

The preparation and characterization of PVDF-CNT composite has been described previously by few researchers . In the one studied by Nicole Levi and coworkers [5], both SWCNT and MWCNT blended with PVDF showed significant enhancement in the β-polymorph phase formation (which is piezoelectric) for most loadings. Solution-cast composites exhibited superior mechanical transduction over pure polymer, which was attributed to the changes in crystallinity. It is not clear if the well dispersed structurally random CNT network within the fluoropolymer matrix had enhanced the bulk modulus or if they had contributed to enhanced thermal stability along with polymer microstructural modification.

This chapter describes the preparation of PVDF-MWCNT composites in varying ratios in order to correlate their mechanical and electrical behavior. We observed a dramatic increase in the thermal stabilities when some of these samples were heated to various temperatures which is indeed important for actuator applications in order to understand their fatigue and failure behavior under cycling. This prompted us to carry out a systematic investigation of PVDF-MWCNT composites especially for their mechanical and thermal behavior over a range of compositions; much above the known electrical percolation threshold (0.1 wt%). The composites were characterized by TGA, DSC, DMA, SEM, and impedance spectroscopy. The results obtained unambiguously demonstrate the enhancement of thermal stability due to the effective interactions of MWCNTs with the fluoropolymer matrix.

9.2 Experimental

PVDF (grade Solef 1008) supplied by Solvay (Belgium) was used for the present study. The molecular weight (M_w) of PVDF was 100×10^3 and M_w/M_n is 2.5. The details of the MWCNTs preparation have been discussed elsewhere [8]. Briefly, a mixture of xylene and ferrocene in 1:0.75 atomic ratio was injected into a quartz tube furnace at 675 °C to yield arrays of MWCNTs.

The melt compounding of PVDF-MWCNT composites was carried out in a DSM microcompounder (210 °C, 100 rpm for 5 min). The composites were prepared by varying the wt. ratios of MWCNTs from one to six. The following discussion pertains to the samples of PVDF with 1 wt% of MWCNTs (PVDF-MWCNT-1) and PVDF with 6 wt% of MWCNTs (PVDF-MWCNT-6) as they serve the best examples of the effects produced by varying amounts of CNTs. The films used for XRD and mechanical analyses were prepared by compression molding at a temperature of 200 °C using a Carver press model F-15181.

A Rigaku x-ray diffractometer (model Dmax 2500) with Cu K_α radiation of wavelength 1.54 Å and energy 8.05 keV was used for the structural characterization of the polymer matrix.

Dynamic mechanical properties of the compression-molded composite films were determined using a Rheometrics Dynamic Mechanical Analyzer (model IIIE) in the tensile mode. The dynamic responses were tested in a temperature range from -100 to 150 °C at a frequency of 10 rad/s with 0.02% strain in the auto strain mode.

Perkin Elmer DSC-2 was used for non-isothermal and isothermal crystallization studies. The samples were heated and cooled at 10 °C/min and the melting and crystallization parameters were determined from the heating and cooling scans respectively, in nitrogen environment at a flow rate of 20 cc/min. Perkin Elmer TGA-7 was used to study the temperature-weight loss characteristics of the composites in a nitrogen atmosphere.

The dispersion of the carbon nanotubes in the polymer matrix was observed from the fractured surface of the composites using SEM model Leica stereoscan 440. Volume resistivities of the composites were studied using four probes. Impedance measurements were performed with a computer controlled Potentiostat/Galvanostat (Autolab PGSTAT 30 with GPES software) and an impedance analyzer (Autolab PGSTAT 30 with FRA software) using a swagelok cell in the frequency range of 100 kHz to 0.01 Hz by perturbing the cell with an ac signal of 10 mV amplitude.

9.3 Results and Discussion

9.3.1 SEM

The dispersion of carbon nanotubes throughout the polymer matrix was observed from the fractured surface of the composites. Figure 9-1 shows the SEM image

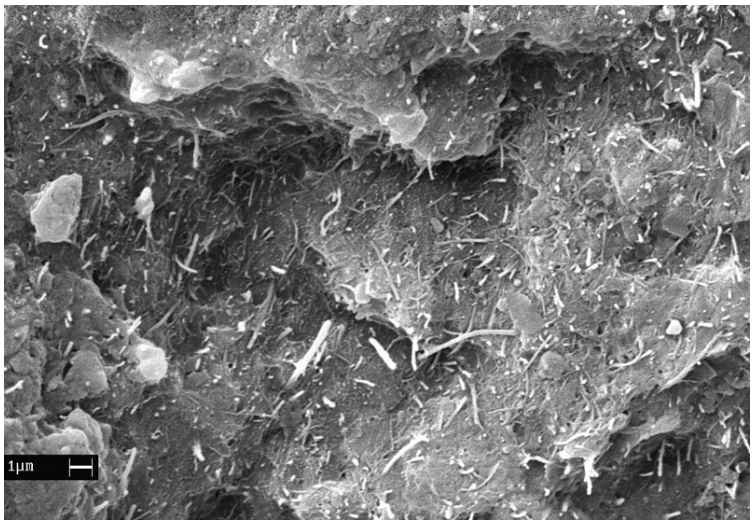

Figure 9-1. SEM image of a fractured surface of PVDF-MWCNT-6 sample.

of a fractured surface of PVDF-MWCNT-6 sample. The dispersion of the CNTs across the volume of the sample can be clearly observed from the image. It seems that carbon

nanotubes are uniformly distributed without agglomeration throughout the polymer matrix without any specific orientation. MWCNTs form a slightly interconnected network in the polymer matrix as can be seen from SEM image. The uniform distribution of CNTs is the key parameter for the mechanical reinforcement, structural, thermal, and electrical properties of the polymer composite. The SEM image of PVDF-MWCNT-1 didn't show any specific distribution pattern (image not shown here).

9.3.2 XRD

The phase structure of PVDF and its nanocomposite films was studied using XRD. Figure 9-2 shows the XRD spectra of PVDF, PVDF-MWCNT-1, and PVDF-MWCNT-6 samples. PVDF is a semicrystalline polymer, where ordered regions of monomer units (crystallites) are surrounded by an amorphous sea of scrambled, spaghetti-like structure [ref]. It also shows polymorphism, i.e. it can exist in four major crystalline forms namely;

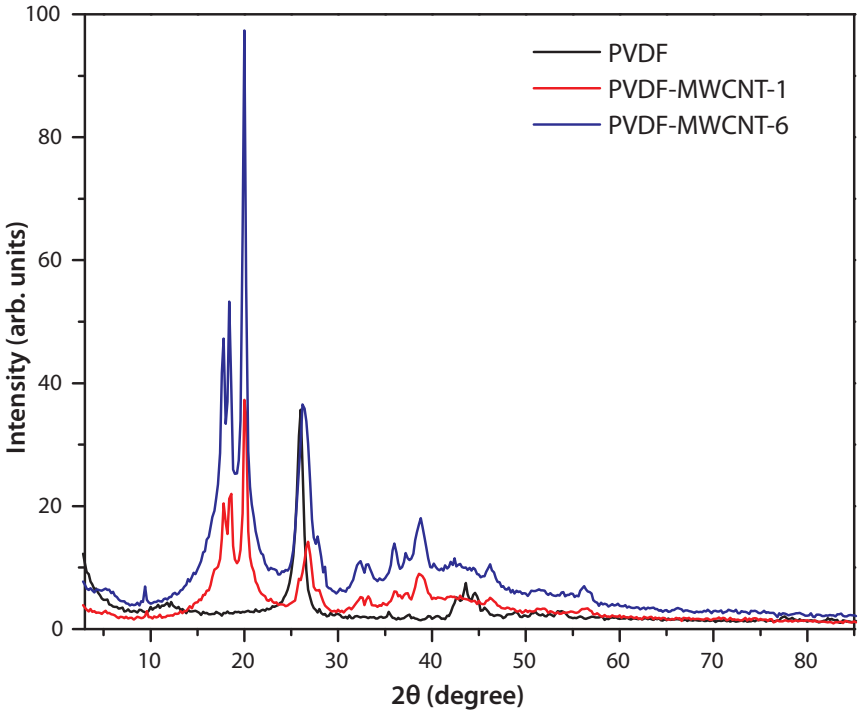

Figure 9-2. XRD spectra of PVDF, PVDF-MWCNT-1, and PVDF-MWCNT-6 samples. PVDF shows α-phase of crystalline form. Addition of CNT enhances the crystallinity of the polymer.

α, *β*, γ, and δ forms depending on the confirmations of chains and their orientation around the chain axis as well as relative directions of adjacent chains [12]. Among these, *β* form shows piezoelectric properties. The degree of crystallinity as well as the orientation of the crystallites can be controlled by various processing techniques.

PVDF and its nanocomposite films were prepared by melt compounding method in which PVDF is annealed and slowly cooled down from the melt. This process usually leads to the formation of α-phase as it is kinetically favored process. As it can be seen from the

figure 9-2, the 2θ peaks at 17.3° (020), 18.15° (110), 26.8° (021), and 38.8° (002), indeed show the presence of α-phase [10]. Addition of MWCNT to the polymer network seems to increase the crystallinity of the polymer as demonstrated by the enhancement in the peak intensities of α-polymorph.

9.3.3 TGA

Figure 9-3 shows a comparison of the thermogravimetric analysis (TGA) data recorded in air at a heating rate of 10 °C/min, suggesting the common aspects of the decomposition patterns of PVDF, PVDF-MWCNT-1, and PVDF-MWCNT-6 samples. The

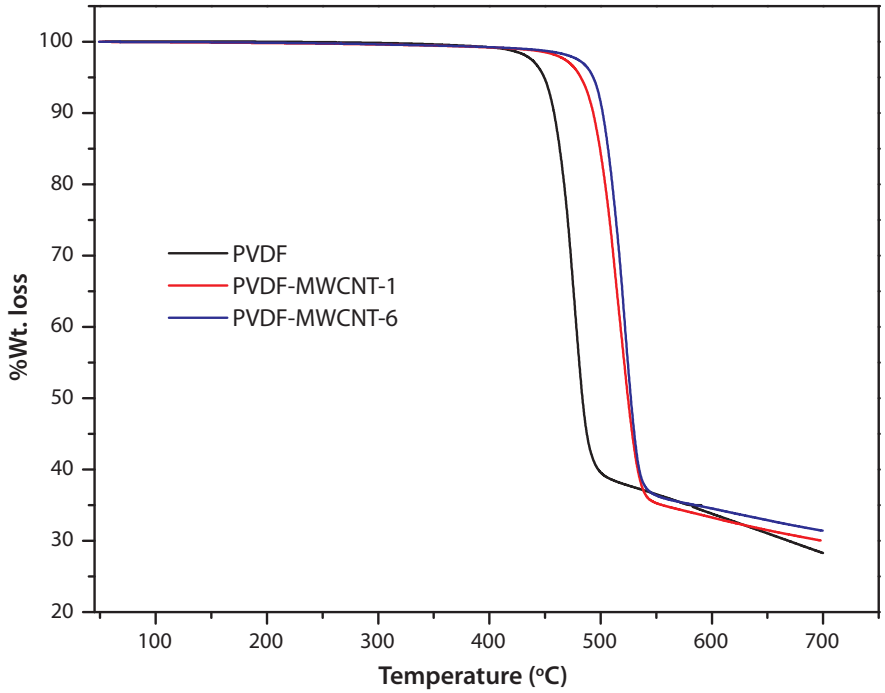

Figure 9-3. TGA curves of PVDF, PVDF-MWCNT-1, and PVDF-MWCNT-6 samples measured in air atmosphere at a heating rate of 10 °C/min.

wt. loss at 500 °C is mainly due to the decomposition of the polymer matrix followed by MWCNT structural disintegration. Interestingly, PVDF-MWCNT-6 sample is more resistant to thermal degradation indicating better thermal stability which can attributed to the uniform distribution of the MWCNTs throughout the polymer matrix.

9.3.4 DSC

Differential scanning calorimetry (DSC) analysis provides support to the conclusions drawn from XRD analysis. The information extracted from DSC thermograms is represented in the bar chart format in the figure 9-4.

As can be seen from the above table, the melting and crystallization temperature

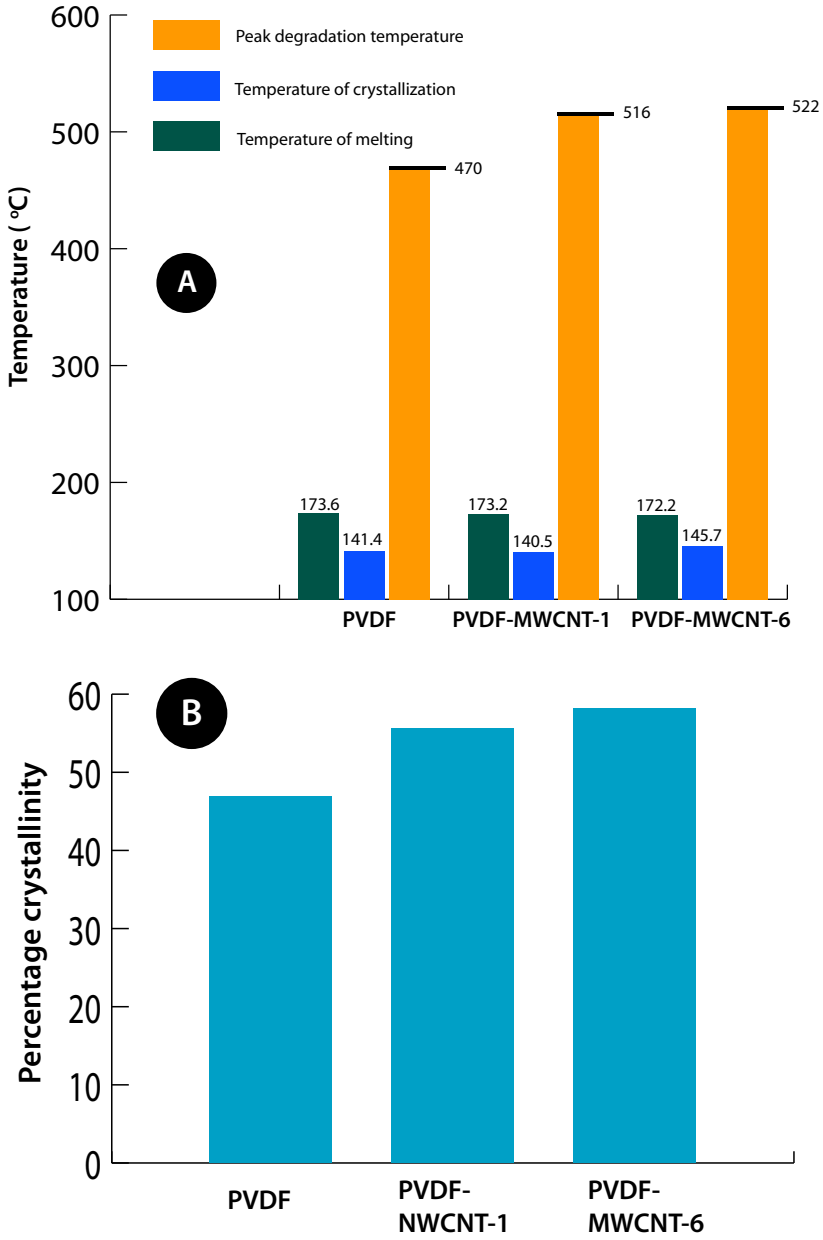

Figure 9-4. Thermal properties of PVDF and its nanocomposites calculated from DSC thermograms. **(A)** Bar chart showing temperatures for various processes such as degradation, crystallization, and melting of all samples. **(B)** Bar chart showing the degree of crystallinity of all samples

almost remains the same within an error of ± 1°C. The crystallinity of the sample increases with CNT content. This implies that CNT acts as nucleating sites for PVDF. Similarly the degradation peak temperature also increases with CNT content. The remnant after charring increases to approximately 35% from 20% implying that CNT forms cross-linked structures with in the material. Addition of CNT increases the crystallinity of the polymer and is becoming monophase. All this features are attributed to the uniformly

distributed network of carbon nanotubes within the polymer matrix.

9.3.5 DMA

Dynamic mechanical analyzer in the tensile mode is a very powerful

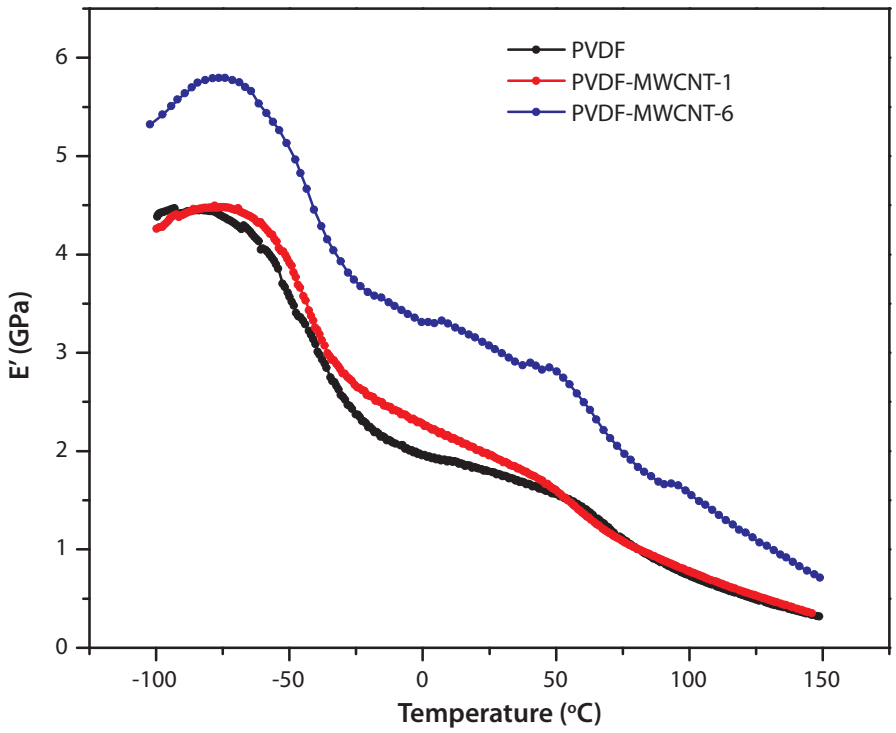

Figure 9-5. Storage modulus vs temperature plots of PVDF and its nanocomposites measured by dynamic mechanical analyzer.

characterization tool for analyzing polymer composites since it enables the quantitative comparison of many parameters associated with the behavior of composites under variable stress. Figure 9-5 shows the storage modulus of PVDF and its nanocomposites at different temperatures. As it can seen from the figure, PVDF-MWCNT-6 nanocomposite shows more than considerable increase in modulus above the glass transition temperature. The glass transition temperature of PVDF is -35 °C. In comparison, the increase in the modulus of PVDF/1% CNT is relatively less (of the order of 30%) at –100 °C. This increase in the dynamic modulus could be ascribed to the uniform dispersion of MWCNTs and to their high aspect ratios [13].

Figure 9-6 shows the measurement of tan δ (phase angle) vs temperature for all the samples. As it can be seen from the above figure, T_g decreases from –38.6 °C to –40.75 °C and –42.62 °C for 1% and 6% MWCNTs loadings respectively. The height of the tan δ peak decreases on the addition of CNT, implying the increase in crystallinity of PVDF matrix. This also confirms the DSC results of increase in crystallinity. Three transitions are observed in the case of the composites as compared to the two transitions at –38 °C,

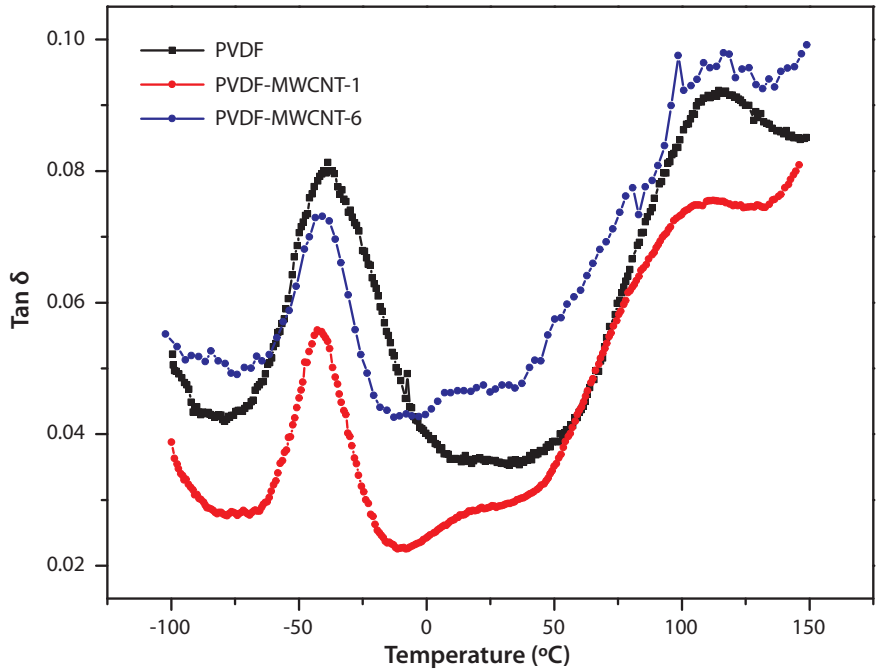

Figure 9-6. Phase angle (tan δ) vs temperature plots of PVDF and its nanocomposites. Addition of CNTs increases crystallinity of the polymer as shown by the changes in the intensity of tan δ peak.

and 100 °C in the case of pristine polymer, which could be attributed to the changes in the conformation of polymer chains. More specifically, due to the presence of constrained amorphous fraction, an additional peak at ~20 °C occurs as a shoulder in the case of pristine polymer.

Addition of carbon nanotubes to the polymer matrix thus induces mechanical reinforcement, and increased thermal stability. The nanotubes are uniformly dispersed throughout the polymer matrix as the van der Waals forces between these two interfaces help in transferring the load efficiently from polymer matrix to the CNT network [14].

9.3.6 Impedance spectroscopy

Figure 9-7 shows the impedance spectra of MWCNT and PVDF-MWCNT-6 samples in the frequency range of 100 kHz to 0.01 Hz. The impedance of PVDF-MWCNT-1 generated too much of noise due to the insulating behavior and is not shown here.

At lower frequencies, the value of the real part of resistance (Z') of the PVDF-MWCNT-6 composite tends to increase with increasing the time of extent of reaction. This experimental finding can be attributed to the modification induced by nanotubes bundles with different aspect ratios occurring during the cure reaction, as discussed below. It is interesting to note that as the nanotubes concentration increases (>5%), the impedance modulus tends to display a frequency independent behavior suggesting the presence of an ohmic material that must possess a very well connected 3D nanotubes

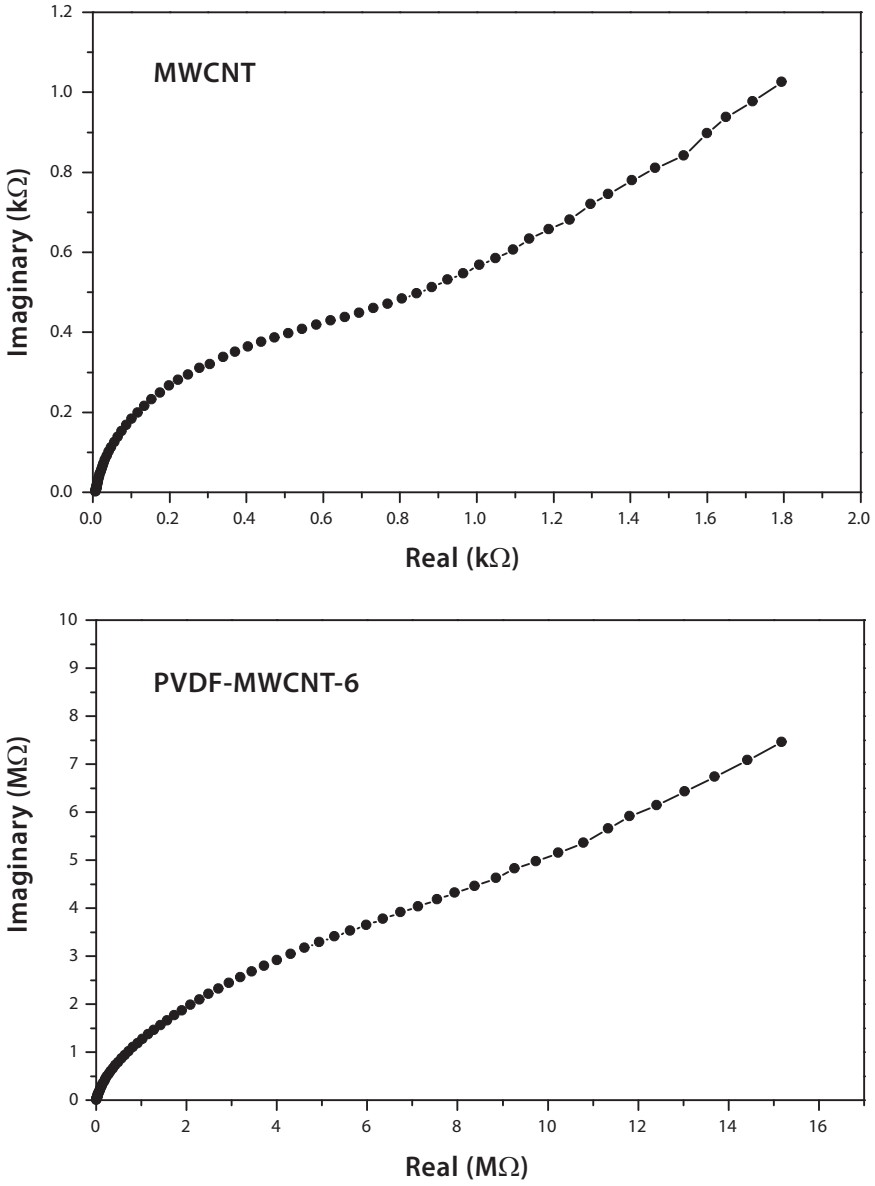

Figure 9-7. Impedance spectra of MWCNT and PVDF-MWCNT-6 measured in the frequency range 100 kHz to 0.01 Hz with an ac signal of 10 mV amplitude.

network. This is also evident from the dc conductivity measurements where 6 wt% addition of CNTs has enhanced the conductivity from 10^{14} S/cm (pristine PVDF) to 5.039×10^{-3} S/cm. This trend signifies that the resistance of the PVDF-MWCNT-6 composite decreases during reaction and this could be attributed to the fact that the charge mobility in the network at any stage of cure is more efficient with the incorporation of nanotubes and hence the system undergoes dielectric loss at higher frequencies [15]. It is interesting to observe that by increasing the wt% of MWCNTs, the imaginary part of the impedance spectrum of the composite tends to approach to the Z" spectrum of MWCNT alone.

Thus it can be seen from above results that the morphological, mechanical and electrical properties of a polymer matrix can be dramatically altered with the addition of a small percent of CNTs. With proper composite reinforcement, it is possible to get improved electric properties with increased mechanical strength.

9.4 Conclusions

Present study has demonstrated that a mere blending of few percentages of MWCNTs in a ferroelectric polymer like PVDF induces significant changes in the structure, crystallinity, mechanical strength and thermals stability of the polymer. Although there is only a minor change in the melting temperature, significant improvement in both crystallinity and thermal stability is observed along with a concomitant enhancement in electrical and mechanical behavior. The bulk modulus increases dramatically as a result – more than 100% increase above the glass transition in some cases. Impedance and SEM data confirm subtle changes in the interfacial morphology while XRD suggests the predominance of α-phase, as it is the kinetically favored process. A qualitative mechanism to account for the enhancement of modulus and thermal stability involves the interfacial anchoring of polymer chains on MWCNT surfaces modification.

9.5 References

1. M. P. Shafer, A. H. Windle, Advanced Materials, 1999, 111, 937
2. H. S. Woo, R. Czeerw, S. Webster, D. L. Caroll, J. Ballato, A. E. Stevens, E. O'brien, W. J. Blau, Applied Physics letters, 2000, 77, 1393
3. K. T. Lau, D. Hui, Composites Part B, 2002, 33, 263
4. R. H. Baughman, C. Cui, A.A Zakhidov, Z. Iqbal, J. N. Barisci, G. M. Spinks, G. G. Wallace, A. Mazzoldi, D. D. Rossi, A.G. Rinzler, O. Jaschinski, S. Roth, M. Kertesz, Science, 284, 1340
5. N. Levi, R. Czerw, S. Xing, P. Iyer, and D. L. Carroll, Nano Lett., Vol. 4, No. 7, 2004
6. E. Kymakis, I. Alexandou, G. A. J. Amaratunga, Synthetic Materials, 2001, 9108, 1
7. M. M. Demir, I. Yilgor, E. Yilgor, B. Erman, Polymer , 2002, 43, 3309
8. I. D. Norris, M. M. Shaker, F.K. Ko, A. G. Synthetic Materials, 2000, 114, 109
9. R.Andrews, D.Jacques, A.M.Rao, F.Derbishire, D. Qian, X.Fan, E.C. Dicky, J.Chen, Chem.Phys.Lett.303 (1991) 467.
10. C. Seoul, T. T. Kae, C. K. Baek, Journal of Polymer Science: Part B: Polymer Physics, 41, 1572, 2003
11. J. Gao, B. Zhao, M. E. Itkis, E. Bekyarova, H. Hu, V. Kranak, A. Yu, R.C. Haddon, J.Am. Chem. Soc. 2006
12. P. M. Ajayan, L.S. Schadler, P. V. Braun, Nanocomposite Science and Technology, Wiley-Interscience Publications, 2001.
13. R. Haggenmueller, W. Zhou, J. E. Fischer, K. I.Winey, Journal of Nanoscience and nanotechnology, 105-110, 3, 2003
14. P. Potschke, T. D. Fornes, D. R. Paul, Polymer 43, 3247-3255, 2002
15. Z. Jin, K. P. Pramoda, S. H. Goh, G. Xu, Materials Research Bulletin 37, 2002, 271-278

PART C

| Bioapplications |

CHAPTER 10

Enzymatic synthesis of hydroxyapatite-carbon nanotubes composite and its biocompatibility study.

This chapter describes a novel method for bio-inspired enzymatic synthesis of nanosized hydroxyapatite and its polymorphs on carbon nanotubes matrix using cheap agro-based waste materials i.e. wheat bran and a novel extra cellular enzyme phytase, produced by solid state fermentation of fungus Aspergillus niger. The challenge was to preserve the structure of CNTs and still come up with a way to disperse them uniformly with hydroxyapatite. The biocompatibility studied with osteoblasts cell lining shows very promising results.

10.1 Introduction

Hydroxyapatite (HA) [$Ca_{10}(PO4)_6(OH)_2$], the main constituent of the bone minerals, has attracted a lot of attention in the medical field because of its ability to promote bone growth along its surface [1]. Recently there has been a tremendous interest in the fabrication of artificial materials that mimic the structure and properties of natural bone for orthopedic and dental applications [2]. In this context, synthesis of HA is of prime importance for the fabrication of artificial bone material.

Various methods of HA synthesis have been developed which usually involves the use of organic nanophase such as acidic proteins or macromolecules to control the crystal nucleation and growth of HA. Macromolecules such as poly-(lactic acid) [3], poly (L-lactide) [4], reconstituted collagen [5], peptide-amphiphile nanofibers [6], and others have been used in the mineralization. However, these methods do not provide total control over the crystal morphology of HA which is a key parameter in its bioactivity. Moreover, HA exhibits poor mechanical properties- lower tensile strength & fracture toughness compared to bone, thus hindering its use in clinical applications. One of the way to overcome this limitation is to add reinforcing phase into the HA ceramic to improve its fracture toughness.

An ideal reinforcing material should be able to impede the crack growth by forming bridges across the crack faces in ceramic, absorbing energy during pullout and bearing much of the applied load. Its morphological characteristic such as aspect ratio is also critical since higher aspect ratio results in better reinforcement. It should form homogeneous phase in the HA ceramic without affecting its bioactivity. The unique structural, mechanical and chemical properties of carbon nanotubes makes them ideal candidate for the reinforcing phase in HA ceramic.

Carbon nanotubes have excellent mechanical properties with a tensile strength in the range of 11-63 GPa, and elastic modulus greater than 1 TPa [7]. They also possess higher aspect ratio (>1000) which makes them ideal reinforcing material. However, uniform dispersion of nanotubes in HA ceramic is difficult due to the lack of universal solvent. Hence, the synthesis of pure phase HA composite with controlled morphology along with carbon nanotubes as reinforcing material is highly desirable.

This chapter describes a novel method for bio-inspired enzymatic synthesis of nanosized hydroxyapatite and its polymorphs on carbon nanotubes matrix using cheap agro-based materials, i.e. wheat bran, and a novel enzyme phytase; produced by solid state fermentation of fungus Aspergillus niger.

Wheat bran; a by-product of the refined grains, contains abundant amount of phosphorous in the form of phytic acid. Phytic acid is known to bind essential dietary minerals, thus restricting their absorption, and also inhibits a number of nutritionally important enzymes in vivo. Hydrolysis of phytic acid often results in the loss of nutritional value. Phytase is an enzyme capable of hydrolyzing phytic acid to inorganic orthophosphate, lower esters of myo-inositol and free inositol [8, 9, 10]. Phytases (myo-inositol hexakisphosphate phosphohydrolases) belong to a special

group of phosphatases that are capable of sequentially hydrolyzing phytate [myo-inositol (1,2,3,4,5,6) hexakisphosphate] to a series of lower myo-inositol phosphates and phosphate. We used the fungus Aspergillus niger for the extracellular production of phytase enzyme by solid state fermentation of wheat bran.

The phytase enzyme was immobilized on single walled carbon nanotubes (SWCNTs) for the synthesis of nanocrystalline HA, β-tricalcium phosphate (β-TCP) and dicalcium phosphate (DCP) by a wet biomimetic method. The resulting HA-SWCNT composite was characterized by FTIR, TEM, and XRD methods.

10.2 Experimental

The purified SWCNTs (HiPCo) were purchased from Carbon Nanotechnologies, Inc., and used as received. The wheat bran used in this study was obtained from an animal feed stuff outlet at Pune, Maharashtra. Phytic acid sodium salt from corn was purchased from Sigma Chemical Company. All other chemicals used were of analytical grade and obtained from Sigma and Glaxo.

The strain used in the present work was Aspergillus niger NCIM 563, maintained on Potato Dextrose Agar (PDA) slants. Solid state fermentation of wheat bran for the production of phytase was carried out as described in a reported work [11]. Fermentation medium was inoculated with 1% (v/v) of spore suspension (5×10^7 spores per ml) prepared by suspending the spores from seven days old sporulated slant of Aspergillus niger NCIM 563. Extraction of phytate from wheat bran was carried out by following a procedure as reported elsewhere [12, 13].

After extraction of enzyme from fermented Koji as described by [11], solid ammonium sulphate was added to the supernatant to 95% saturation with constant stirring. The precipitate was collected by centrifugation at 15,000 × g for 20 min and dissolved in smallest possible volume of acetate buffer (100 mM, pH 5.5) and salt was removed by passing through Sephadex G-25 column and active fractions were concentrated through YM-30 membrane (Millipore) and used for phytase activity measurement.

The SWCNTs (10 mg) were dispersed in acetate buffer of pH 5.5 (100 mM) with the aid of probe sonicator. The extracted phytase enzyme was added to this solution and again sonicated for ten minutes. The SWCNTs immobilized with phytase enzyme were filtered through membrane filter (PTFE, 0.4 μ pore size) and washed thoroghly with water to remove excess of enzyme.

The activity of phytase enzyme immobilized on SWCNTs was measured at 50 °C using acetate buffer (pH 5.5, 100 mM) as described in the report [11]. The liberated inorganic phosphate was measured by a modification of the ammonium molybdate method [14]. A freshly prepared solution of acetone: 5 N H_2SO_4:10 mM ammonium molybdate (2:1:1 v/v/v) and 400 μl of 1 M citric acid were added to the assay mixture. Absorbance was measured at 370 nm. One unit of phytase activity (IU) was expressed

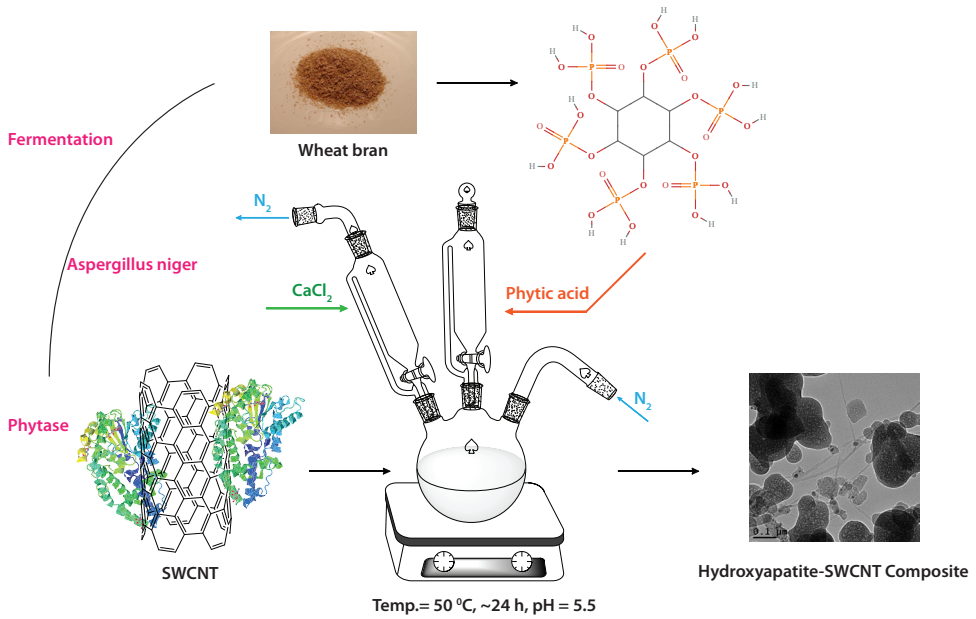

Figure 10-1. Schematic representation of the hydroxyapatite-SWCNT composite synthesis. Phytase enzyme produced by solid state fermentation of wheat bran was immobilized on SWCNTs. Phytic acid (extracted from wheat bran) was added along with $CaCl_2$ to the reaction mixture. Reaction was carried out in acetate buffer (pH=5.5, 50 mM) at 50 °C maintaining inert atmosphere by bubbling nitrogen.

as the amount of enzyme that liberates 1 µmol phosphorus per minute under standard assay conditions.

Figure 10-1 shows the schematic representation of the reaction for the synthesis of HA-SWCNT composite. The phytic acid (3 mM) extracted from wheat bran and SWCNTs immobilized with partially purified phytase enzyme were added to a three neck round bottom (RB) flask. The reaction was carried out in an acetate buffer (pH = 5.5, 50 mM) at a constant temperature of 50 °C. The solution of $CaCl_2$ in distilled water (50 mM) was added to this RB flask. Nitrogen gas was bubbled continuously to avoid carbonate contamination. The reaction mixture was stirred continuously for four hours. A white precipitate was obtained which was then aged in the mother liquor for 24 h. The final product was isolated by centrifugation in an airtight sealed containers and washed with decarbonated water and dried at 40 °C. The dried samples were calcined at ~1000 °C for two hours.

The obtained HA-SWCNT composite was characterized by different techniques to understand the formation of HA and its interaction with SWCNTs. The XRD analysis was performed using an 'X' Pert Pro diffractometer, operating at a voltage of 20 kV with a Cu-Kα radiation, λ = 1.5401 Å. The FTIR analysis was performed using Perkin-Elmer Spectrum One instrument at a resolution of 2 cm^{-1}. Samples were prepared by KBr pellet method. The transmission electron microscopy (TEM) and high-resolution transmission electron microscopy (HRTEM) images and electron diffraction patterns were obtained on Tecnai F30 FEG machine operated at 300 kV.

The biocompatibility of HA-SWCNT was checked by standard cytotoxicity screening tests. The in vitro cytotoxicity studies were done in direct contact method (ISO 10993–5, 1999) [15] using L929 (mouse fibroblast subcutaneous connective tissue) cell line [16] procured from National Center for Cell Sciences, Pune, India. The HA-SWCNT composite samples were placed onto the monolayer of cells under sterilized conditions and incubated at 37 °C under 5% CO_2 and 95% humidity for 48 h. The viability of the cells in the vicinity of the material was examined by MTT assay [17]. Control experiments were carried under similar conditions.

10.3 Results and Discussion

The activity of partially purified phytase enzyme immobilized on SWCNTs was 16.12 IU/ml and specific activity was 46.34 IU/mg.

The reaction between phytase enzyme immobilized on SWCNTs and phytic acid (extracted from wheat bran) results in the release of inorganic monophosphate due to the hydrocatalysis by phytase enzyme on the ester bond present between phosphorus and carbon of myo-inositol ring. The released phosphate molecule binds with the calcium ion and forms the white precipitate of calcium phosphate at 50 °C in an acidic environment. The residual protein along with other side products such as myo-inositol, lower phosphoric esters of myo-inositol were removed from calcium phosphate precipitate by subsequent washing with deionized water.

10.3.1 XRD analysis

The crystallization of as synthesized HA-SWCNT composite formed by the phytase enzyme reaction with phytic acid after four hours was followed by X-ray diffraction (XRD).

Figure 10-2 shows the XRD spectra of as synthesized HA-SWCNT (after four hours of reaction) and calcined (~1000 °C) HA-SWCNT composite. The as synthesized HA-SWCNT composite shows broad peaks at 28.16 and 5.32 indicating the amorphous nature with low crystallinity. However, the obtained results are comparable to the diffraction pattern of the biological apatite and are in good agreement with the previous results [18]. The phytase enzyme immobilized on SWCNTs wraps around the core of nanotubes and is responsible for the hydrolysis of phytate. Thus the nanotubes surface area is covered by the reaction products including white precipitate of calcium phosphate.

The calcination of this as HA-SWCNT composite at ~1000 °C results in the development of crystalline phase with sharp XRD peaks as shown in the figure 10-2. The XRD profile of the calcined material matches very well with those of HA, β-tricalcium phosphate (β-TCP) and dicalcium phosphate (DCP) [19]. The XRD peaks especially around 29.60 and 31.10 positions are the characteristic peaks for the calcium hydroxyapatite (JCPDS No. 09-0 432) [20]. The presence of organic molecules in residual protein also affects the crystallinity of the HA-SWCNT composite.

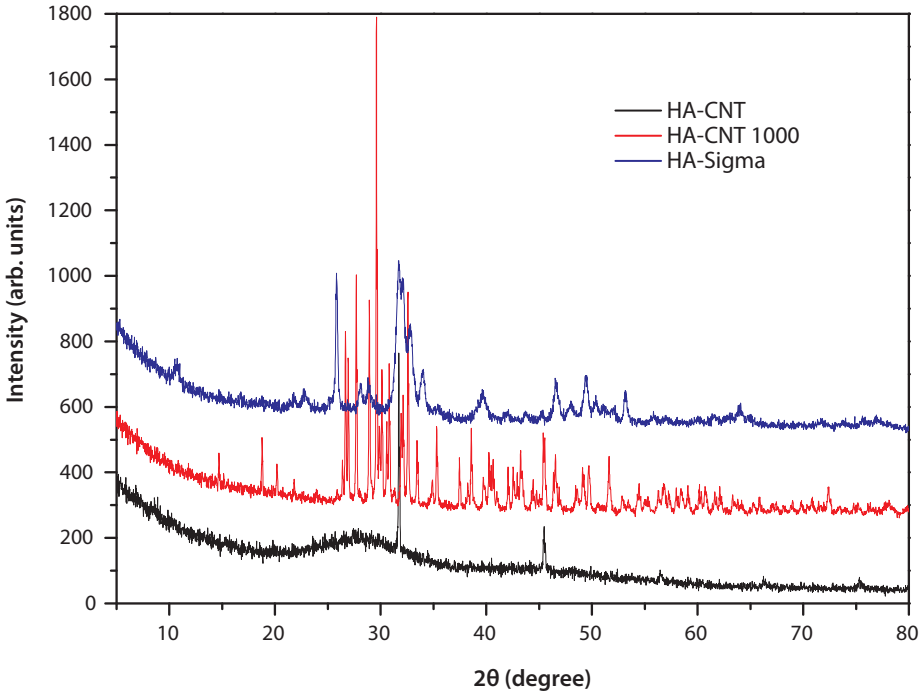

Figure 10-2. XRD spectra of as synthesized HA-SWCNT (HA-CNT) composite and calcined (~1000 °C) HA-SWCNT (HA-CNT 1000) composite. The XRD spectra of composite samples were compared with that of commercial hydroxyapatite (HA-Sigma) obtained from Sigma Chemicals.

The calcined HA-SWCNT composite thus show the presence of HA, β-TCP, and DCP forms, and thus it is polyphasic in nature. The XRD pattern show close resemblance to the diffractogram of bone material. More importantly all these forms of calcium phosphates are developed around the nanotube core due to the immobilized phytase enzyme, thus leading to the formation of homogeneous nanocomposites.

10.3.2 TEM analysis

Figure 10-3 shows the TEM and HRTEM images of the as synthesized as well as calcined HA-SWCNT composites. As it can be seen from the figure, HA forms quite a dense network around the nanotubes. HA particles were around ~50-70 nm in size and exhibit 3D, polyhedral, drop like structures including interconnected hollow spheres.

The as synthesized HA-SWCNT (images [A] & [B]) composite contains a lot of organic matter such as residual protein, side products of the phytic acid hydrolysis which form a thick coating around calcium phosphate and in turn nanotube core. Also at room temperature the crystalline phases of HA are not well developed as it can be seen from the electron diffraction pattern shown in the inset [B]. The presence of these organic molecules provides the connectivity between HA and carbon nanotubes thus forming a dense network of interconnected hollow spheres.

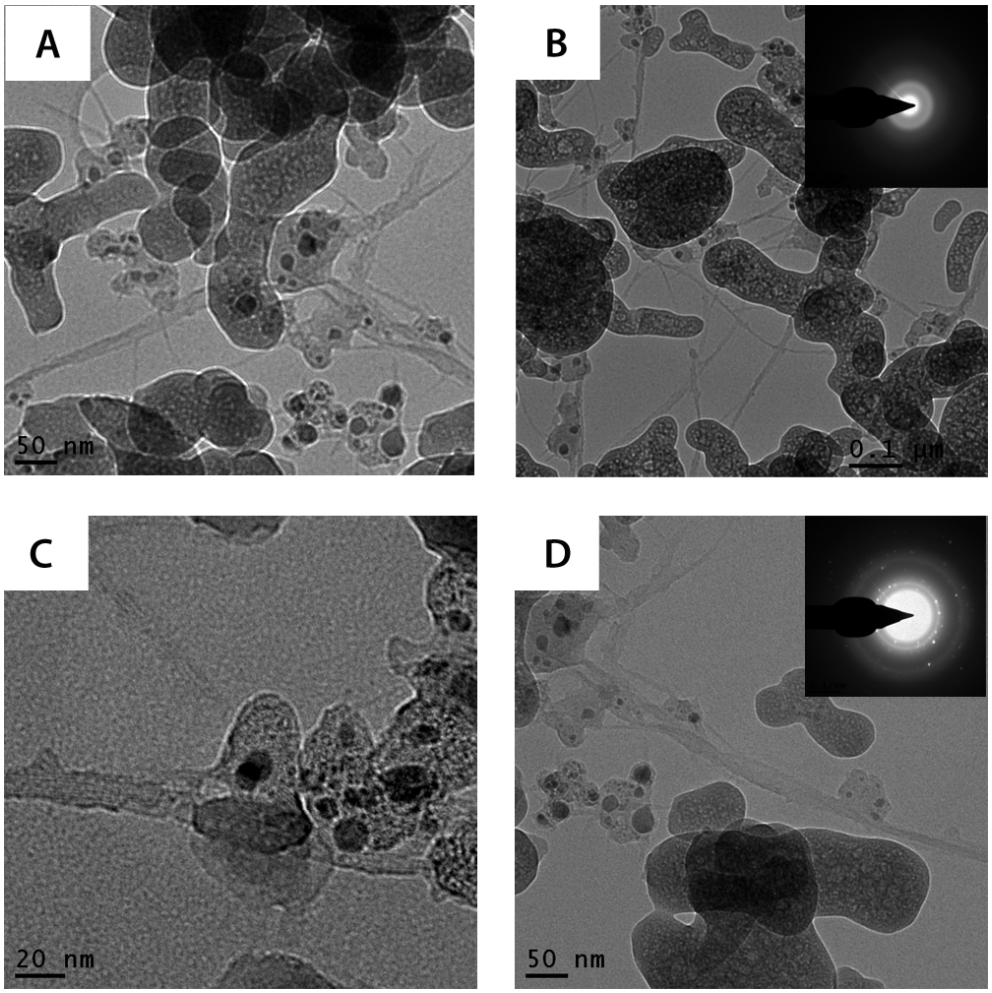

Figure 10-3. TEM and HRTEM images of HA-SWCNT composites. [A] and [B] are the TEM images of the as synthesized HA-SWCNT composites. Inset in [B] shows the electron diffraction pattern of the as synthesized HA-SWCNT sample showing amorphous nature. [C] and [D] are the HRTEM and TEM images of the calcined (~1000 °C) HA-SWCNT composites. Inset in [D] shows the electron diffraction pattern of the calcined HA-SWCNT composite reflecting the polycrystalline nature.

After calcination at ~1000 °C, the HA-SWCNT develops crystalline phases and exhibits polymorphism due to the presence of β-TCP, and DCP forms. Due to the heat treatment, the loss of organic matter occurs affecting the morphology. As it can seen from the figure (images [C] & [D]), the loss of occluded proteins changed the morphology to an irregular interconnected lattice type structure. The particle size was also reduced to ~20 to 30 nm. The HA particles are still connected to the nanotubes network despite the loss of organic matter. Thus enzymatic synthesis of HA-SWCNT composite seems to be a better method of forming nanocomposites while retaining the superior properties of carbon nanotubes.

The diffraction pattern (inset [D]) clearly shows the sharp diffused ring patterns confirming the crystallinity of the calcined calcium phosphate, where the lattice planes exhibit spacing of ~ 2.043 A° and ~ 1.328 A° corresponding to the lattice planes (113) and

(314) respectively. The pattern also suggests the polycrystalline nature of HA.

10.3.3 FTIR-analysis

Figure 10-4 shows the FTIR spectra of as synthesized HA-SWCNT and calcined composite compared with the commercial sample of HA from Sigma Chemicals.

A peak around 3450 cm^{-1} can be attributed to the combination of OH group (HA phase). The peaks in the region 600-500 cm^{-1} are due to apatitic PO_4^{3-} ν_4 modes. The peaks around 1150-1000 cm^{-1} can be attributed to the ν_1 and ν_3 modes that correspond to factor group splitting of PO_4^{3-} tetrahedral [21]. The bands at ~953-961 cm^{-1} corresponds to ν_1

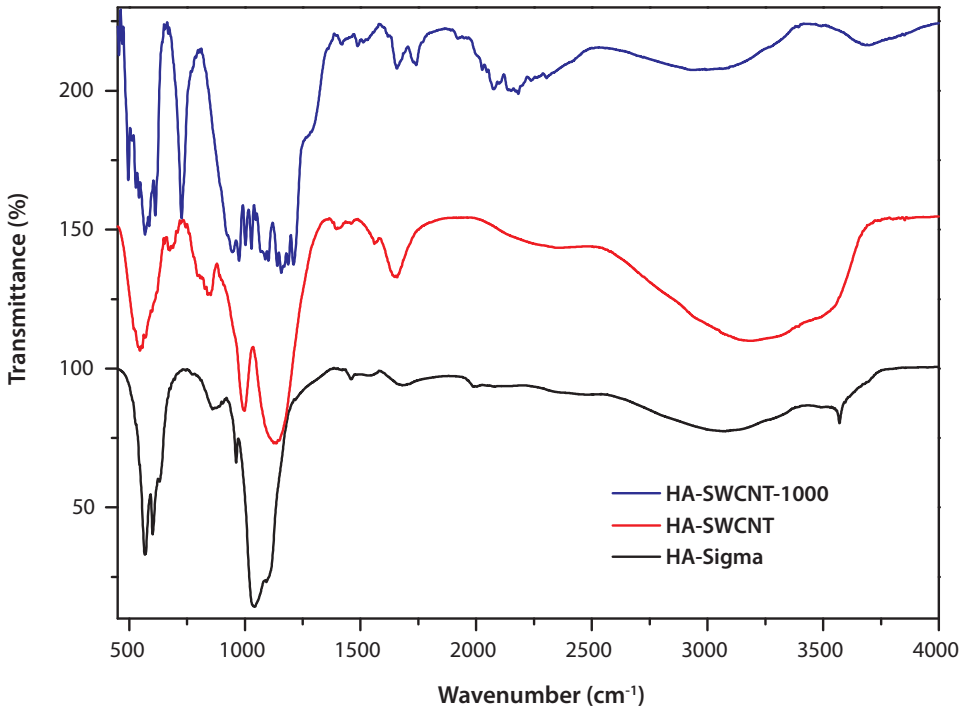

Figure 10-4. FTIR spectra of as synthesized HA-SWCNT and calcined (~1000 °C) HA-SWCNT for the identification of functional groups. Both the spectra were compared with the commercial sample of HA from Sigma Chemicals as standard.

symmetric and ν_4 P-O stretching vibrations of the PO_4^{3-} ion, respectively [22].

The two intense peaks at 1644 and 1547 cm^{-1} can be attributed to the amide group. This observation indicates that the particles in the hollow spherical/circular morphology are present with proteins that are possibly occluded into the particles or are bound to the surface of the particles [23].

The calcination treatment results in the loss of organic matter and hence the peak intensity of amide bands is reduced in the calcined sample of HA-SWCNT composite.

The peak intensities of organic functional groups around 1400 cm^{-1} were diminished after calcination treatment [24]. The FTIR spectra analysis confirms the formation of HA and its polymorphs. As it can be seen from the figure 10-4, the signatures of HA in as synthesized HA-SWCNT and calcined HA-SWCNT composites are comparable with the FTIR profile of commercial HA sample from Sigma Chemicals.

10.3.4 Biocompatibility

The in vitro biocompatibility of HA-SWCNT composite was checked with L 929

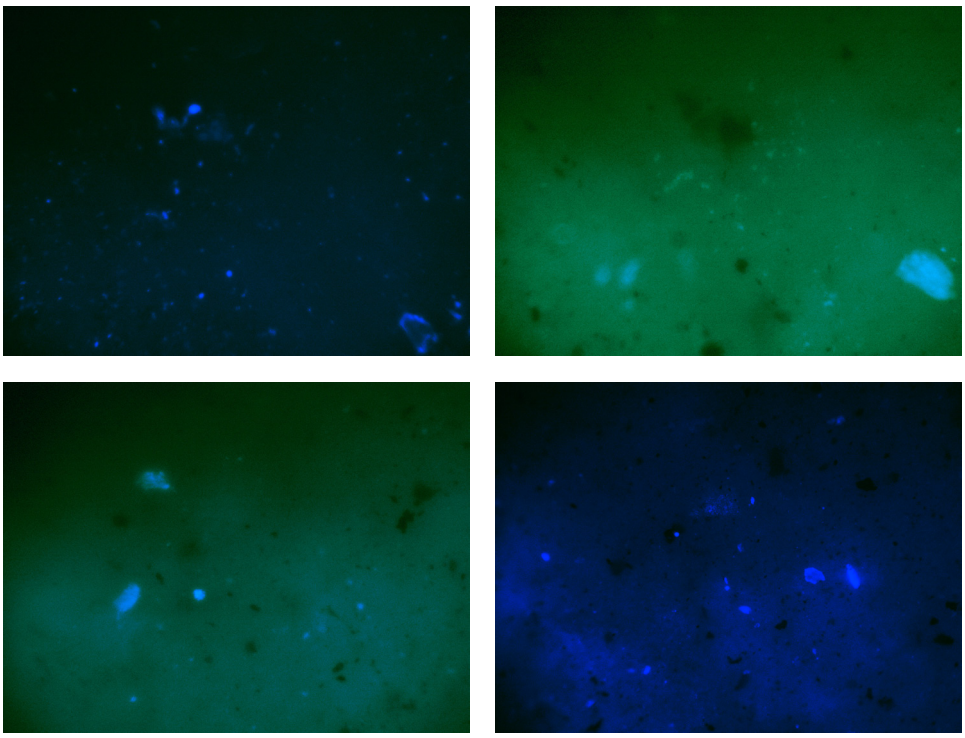

Figure 10-5. Light microscopic images of L 929 cells (mouse fibroblast) incubated with HA-SWCNT. (Under 10X magnification). Images were taken after 48 hours of incubation.

cells (mouse fibroblast) just to get a preliminary idea of possible cytotoxicity. We did not study cell growth at specific time intervals but just observed the growth of cells after 48 hours to check the non-toxic nature of HA-SWCNT composite. We observed a good growth of mouse fibroblast cells in the vicinity of HA-SWCNT composite.

Figure 10-5 shows the light microscopy images taken during the direct contact cytotoxicity test. The growth of cells clearly shows the non-toxic nature of HA-SWCNT composite. The presence of hydrogen bonding and van der Waals forces developed between the hydroxyl groups of glycol proteins present on the cells surfaces and the hydroxyl groups of HA particles is believed to facilitate the growth of cells on the composite [25].

10.4 Conclusions

The nanocomposites of hydroxyapatite and carbon nanotubes have been successfully synthesized using cheap agro-based materials, i.e. wheat bran and phytase enzyme produced by solid-state fermentation of fungus Aspergillus niger. The HA-SWCNT composites were characterized by FTIR, XRD and TEM techniques to understand the formation of HA and its interaction with SWCNTs. HA and its polymorphs were uniformly grown along the nanotubes surfaces forming homogeneous composites. The main advantage of this method is that the unique inherent properties of carbon nanotubes are retained in the composite as the growth of HA did not alter the structure of nanotubes. The biocompatibility study revealed the non-toxic nature of HA-SWCNT composites making them useful for artificial bone grafting applications.

10.5 References

1. A.E. Porter, S.M. Best, W. Bonfield, J. Biomed. Mater. Res. A 2004, 68, 133.
2. A. Tiselius, S. Hjerten, O. Levin, Arch Biochem Biophys. 1956, 65, 132-155.
3. T. Kasuga, Y. Ota, M. Nogami, Y. Abe, Biomaterials 2001, 22, 19-23.
4. Y. Shikinami, M. Okuno, Biomaterials 1999, 20, 859-877.
5. M. Kikuchi, S. Itoh, S. Ichinose, K. Shinomiya, J. Tanaka, Biomaterials 2001, 22, 1705-1711.
6. J. D. Hartgerink, E. Beniash, S. I. Stupp, Science 2001, 294, 1684.
7. M. F. Yu, O. Lourie, M. J. Dyer, K. Moloni, T. F. Kelly, R. S. Ruoff, Science 2000, 287, 637.
8. R. Wodzinski, A.H.J. Ullah, Adv Appl Microbiol. 1996, 42, 263-302.
9. E. J. Mullaney, C. Daly, A. B. Ullah, Adv. Appl. Microbiol. 2000, 47, 157-199.
10. S. K. Soni, J. M. Khire, World J. of Microbiol. Biotechnol. 2007, 23, 1585-1593.
11. T. N. Mandviwala, J. M. Khire, Journal of Industrial Microbiol. and Botechnol. 2000, 24, 237-243.
12. B. F. Harland, D. Oberleas, Cereal Chem. 1977, 54, 827.
13. M. Latta, M. J. Eskin, Agric. Food Chem. 1980, 28, 1313-1315
14. J.K. Heinohen, R.J. Lathi, Anal Biochem. 1981, 113, 313–317.
15. ISO 10993-5:1992(E). Biological evaluation of medical devices—Part 5: Tests for cytotoxicity: in vitro methods.
16. B.J. Nablo, M. H. Schoenfisch, Biomaterials 2005, 26, 4405-4415.
17. A. P. Wilson, Cytotoxicity and Viability Assays in Animal Cell Culture: A Practical Approach, 3rd ed. (ed. Masters, J. R. W.), Oxford University Press: Oxford 2000, 1, 175-219.
18. D. K. Groot, Biomat. 1980, 1, 47-50.
19. M. Jarcho, J. Mat. Sci. 1976, 11, 2027-2035.
20. F. Wang, Materials chemistry and Physics 2006, 95, 145-149.
21. T. -M.G. Chu, J.W. Halloran, S.J. Hollister, S.E. Feinberg, J. Mater. Sci.: Mater. Med. 2001, 12, 471-478.
22. F. Miyaji, Y. Kono, Y. Suyama, Mater. Res. Bull. 2005, 40, 209-220.
23. D. Rautaray, A. Sanyal, S. D. Adyanthaya, A. Ahmad, M. Sastry, Langmuir 2004, 20, 6827–6833.
24. V. Bansal, A. Ahmad, M. Sastry, J. Am. Chem. Soc. 2006, 128, 14059 –14066.
25. Y. Dong, S.S. Feng, Biomaterials 2005, 26, 6068-6076.

CHAPTER 11

Making sugar with carbon nanotubes.

This chapter describes a superior method for the conversion of cellulose to glucose and cellooligomers using carbon nanotubes. Depletion of fossil fuels has forced us to look for alternative resources and cellulose seems to be preferred choice being abundantly available in the nature. However hundreds of years of evolution has made cellulose recalcitrant- resistant to the attacks of bacteria and acids. Carbon nanotubes efficiently cracked cellulose into glucose and other cellooligomers which when subjected to enzyme hydrolysis produced ethanol.

11.1 Introduction

There has been an increasing interest in the production of energy, fuels, and chemicals from renewable biomass in order to prevent the harmful environmental consequences generated from the consumption of fossil fuels [1]. Cellulose, the most abundant source of biomass, is currently regarded as a promising alternative for fossil fuels [2]. Cellulose is not digested by human body, hence its use as a feedstock for biofuel, unlike corn or starch, would not affect the global food supply. Moreover cellulose can be derived from the abundantly available resources such as switchgrass and woody plants that can be developed on agriculturally marginal lands with minimal fertilizer, pesticide, and fossil energy inputs [3]. Hydrolysis of cellulose into water-soluble sugars is a key technology as sugars can be converted into a range of industrially important chemicals, such as ethanol, hydrocarbons, and the starting materials for polymers [4].

However, hundreds of years of evolution has made cellulose recalcitrant- resistant to the attacks of bacteria and acids. Structurally, cellulose is a water-insoluble aggregate of long-chain β- 1, 4 glucan composed of glucose monomers linked by β- 1, 4 glycosidic bonds [5]. The polymeric chains of cellulose are held together by a network of strong hydrogen bonds which makes the hydrolysis of the β- 1, 4 glycosidic bonds extremely difficult. Substantial efforts have been devoted to the development of appropriate hydrolysis routes, such as catalysis using mineral acids [6], enzyme catalyzed reactions [7], the use of subcritical and supercritical water [8], and solid catalysts for hydrogenolysis [9]. However, all these methods are either difficult to scale-up for industrial productions or too expensive, energy-inefficient for the real-world applications [10].

In this chapter, we report a novel method to convert cellulose into glucose and cellobiose using carbon nanotubes. Cellulose was dissolved in alkylmethylimidazolium ionic liquids, which typically exposes cellulose chains making them accessible for chemical transformations [11]. Addition of carbon nanotubes to these solutions and subsequent microwave treatment for a very short time cracks the cellulose into sugar and cellobiose. The most important advantage of the method is the reusability of the carbon nanotubes catalyst and ionic liquids for several transformations.

11.2 Experimental

The cellulose used in al experiments was bagasse cellulose developed by a proprietary process for the extraction of 94% α-cellulose from sugarcane bagasse [12]. The ionic liquid used to dissolve cellulose was 1-Butyl-3-methylimidazolium chloride that was purchased from Sigma-Aldrich. Single walled carbon nanotubes (SWCNTs) were obtained from Prof. Apparao M. Rao, Clemson University.

In a typical experiment 0.3 g of bagasse cellulose was dissolved in 3 g of 1-Butyl-3-methylimidazolium chloride using a microwave digestion system (Anton Paar 3000 SOLV). The solution was sealed in a Teflon-lined double-walled digestion vessel. The temperature was kept 90 °C for 90 s at 150 W of power. To this solution SWCNTs were added in 1, 3 and 5 wt%, and the resulting mixture was sealed in a Teflon-lined double-

walled digestion vessel for the microwave treatment. The treatment was carried at 40 °C for 30 s using a power of 150 W. The vessel was naturally cooled down to room temperature.

Rheological properties of the solutions were measured using MCR-301 (Anton Paar) rheometer. The Raman spectra were recorded using micro Raman spectrometer (Horiba JY LabRAM HR 800) with an excitation wavelength 632.8 nm from a He-Ne laser.

The 0.25 g of SWCNT treated cellulose in ionic liquid was dissolved in 10 ml of distilled water, SWCNTs were filtered using filter membrane, and the solution was centrifuged at 1000 rpm for 10 min. The supernatant was analyzed for the sugars. The total reducing sugars was estimated as glucose equivalent by dinitrosalicylic acid (DNS) method []. The amount of glucose and cellobiose was determined using a high performance liquid chromatography (HPLC) system (Dionex India Limited) equipped with RI-detectors. An ion exclusion column (Aminex HPX-87H, Biorad, Hercules, CA) was used at a temperature of 30 °C with 0.008 N H_2SO_4 as a mobile phase at a flow rate of 0.6 ml/min. An injection volume of the sample was 50 ml. The glucose was also estimated by glucose oxidase method [ref].

11.3 Results and Discussions

The SWCNTs treated cellulose in an ionic liquid was subjected to rheological analysis along with cellulose in ionic liquid solution.

11.3.1 Rheology

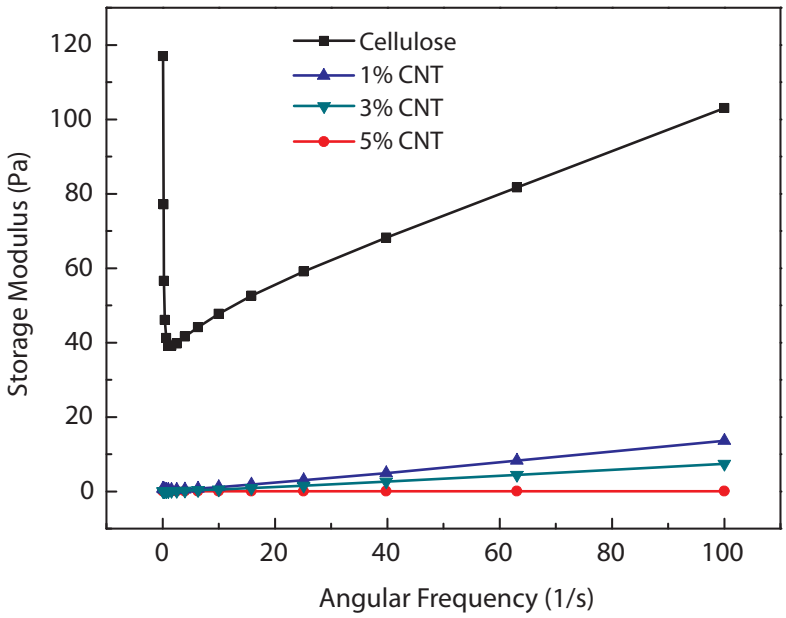

Figure 11-1. Rheological analysis of SWCNT treated cellulose in ionic liquid and cellulose dissolved in ionic liquid solutions.

Dynamic rheology is a powerful tool for evaluating the structure of melts or suspensions [13]. Figure 11-1 shows the rheological analysis of the SWCNT treated cellulose samples along with cellulose dissolved in ionic liquid solution.

As it can be seen from the figure, the storage modulus of cellulose solution ionic liquid is greater than those of nanotubes treated solutions. Ionic liquid simply loosens the hold of strong hydrogen bonding network in cellulose thus making it soluble. The resulting solution simply showed a typical gel-like behavior. Cellulose can be regenerated from this solution.

The addition of SWCNTs to the cellulose solution in ionic liquid also exhibits gel-like behavior due to the formation of a SWCNT network structure caused by strong interactions between the SWCNTs and ionic liquids [14]. However, due to microwave treatment SWCNTs create a sort of local heat centers which crack down the exposed cellulose polymeric chains in ionic liquid. The cracking of cellulose chains resulted in loss of storage modulus of these solutions. Addition of more SWCNTs simply maximizes this effect.

11.3.2 HPLC analysis

Table 11-7 shows the HPLC analysis results for the SWCNT treated cellulose samples as well as cellulose dissolved in ionic liquid solution.

Table 11-7. HPLC analysis of with and without addition of SWCNT & microwave treatment.

Sample	Total cellobiose (mg)	Total glucose (mg)
Cellulose in ionic liquid	-	-
1% SWCNT treated sample	0.2	0.8
3% SWCNT treated sample	1.0	2
5% SWCNT treated sample	1.2	2.2

Apart from glucose and cellobiose, presence of other higher sugars were speculated as the analysis of these sugars was difficult. MALDI-TOF analysis showed a number oxidative products which were difficult to analyse (Data not shown here).

Thus microwave treatment of SWCNTs added cellulose solutions in ionic liquids results in cracking of the cellulose polymer chains to produce sugar and cellobiose. More wt% of SWCNTs in ionic liquid forms network through Pi-Pi interactions which effectively attacks the exposed cellulose polymeric chains breaking down them to sugars and cellobiose.

11.3.3 Raman analysis

The filtered SWCNTs in the purification step were used for cracking next batch of cellulose to check their reusability. The same batch of SWCNTs was used for three experiments.

In all three experiments, the cracking efficiency was found to be same. The

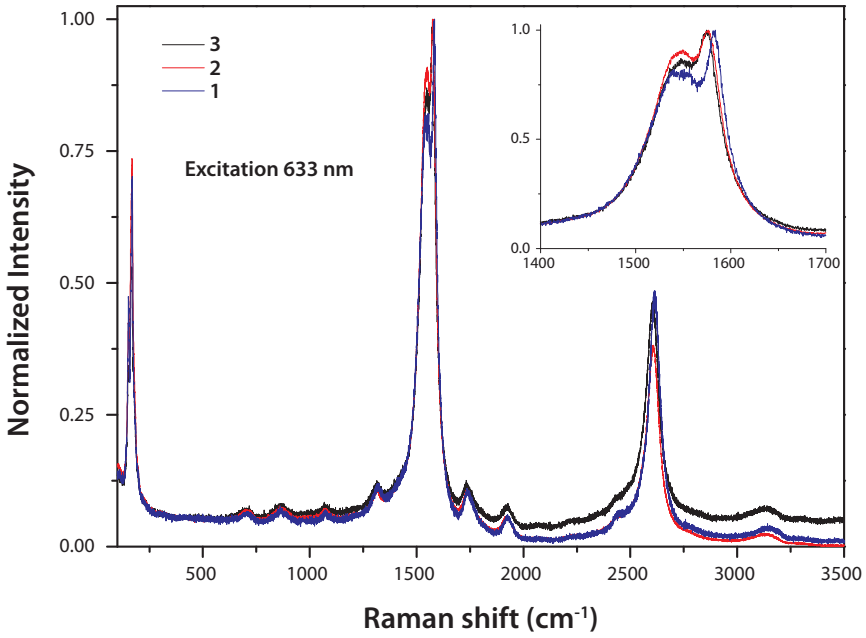

Figure 11-2. Raman spectra of SWCNTs recorded after each cellulose cracking experiments. The numbers 1, 2, and 3 denotes the number of times same SWCNTs used for cracking experiments. Inset shows the expanded region of D and G bands.

SWCNTs were analyzed by Raman spectroscopy after each experiment to follow the structural changes. Figure 11-2 shows the Raman spectra of SWCNTs measured after cracking of the cellulose.

As it can be seen from the inset in figure 11-2, the intensity of D-band increased after each cracking experiment clearly showing the generation of more defects on SWCNTs. However, the entire structure of SWCNTs seemed to be still intact. We performed nine cracking experiments with the same batch of SWCNTs which showed more or less same cracking efficiency (data not shown here) indicating excellent reusability of the SWCNTs.

11.4 Conclusions

The successful conversion of cellulose to glucose and cellobiose was achieved by dissolving bagasse cellulose in 1-Butyl-3-methylimidazolium chloride in presence of SWCNTs by microwave treatment. Ionic liquid weakens the hydrogen bonding between two cellulose linear polymer chains thus exposing them for transformation. SWCNTs in presence of microwave radiation effectively cracks the exposed chains of cellulose to form glucose and cellobiose. The amount of sugars formed was measured by HPLC analysis. More amount of carbon nanotubes results in greater conversion. The reusability of SWCNTs catalyst was checked by performing a series of cracking experiments using

the same batch of SWCNTs. They showed excellent reusability with same cracking efficiency. Raman analysis indicated more number of defects sites.

11.5 References

1. J. Hill, E. Nelson, D. Tilman, S. Polasky, D. Tiffany, Proceedings of the National Academy of Sciences 2006, 103, 11206.
2. L. R. Lynd, J. H. Cushman, R. J. Nichols, C. E. Wyman, Science(Washington) 1991, 251, 1318-1318.
3. M. Schmer, K. P. Vogel, R. B. Mitchell, R. K. Perrin, Proceedings of the National Academy of Sciences 2008, 105, 464.
4. A. J. Ragauskas, C. K. Williams, B. H. Davison, G. Britovsek, J. Cairney, C. A. Eckert, W. J. Frederick Jr, J. P. Hallett, D. J. Leak, C. L. Liotta, Science 2006, 311, 484.
5. M. W. Bauer, L. E. Driskill, W. Callen, M. A. Snead, E. J. Mathur, R. M. Kelly, Journal of bacteriology 1999, 181, 284.
6. E. Harris, E. Beglinger, G. Hajny, E. Sherrard, Industrial & Engineering Chemistry 1945, 37, 12-23.
7. Y. H. P. Zhang, L. R. Lynd, Biotechnology and Bioengineering 2004, 88, 797-824.
8. M. Sasaki, B. Kabyemela, R. Malaluan, S. Hirose, N. Takeda, T. Adschiri, K. Arai, The Journal of Supercritical Fluids 1998, 13, 261-268.
9. M. Sasaki, Z. Fang, Y. Fukushima, T. Adschiri, K. Arai, Ind. Eng. Chem. Res 2000, 39, 2883-2890.
10. A. Fukuoka, P. L. Dhepe, Angewandte Chemie International Edition 2006, 45, 5161-5163.
11. R. P. Swatloski, S. K. Spear, J. D. Holbrey, R. D. Rogers, J. Am. Chem. Soc 2002, 124, 4974-4975.
12. Varma, A.J., (2007). Indian patent application 1893/DEL/2007 dated 27 Aug. 2007.
13. M. W. Frey, J. A. Cuculo, S. A. Khan, Journal of polymer science part B: Polymer physics 1996, 34, 2375-2381.
14. R. Sammons, J. Collier, T. Rials, S. Petrovan, Journal of Applied Polymer Science 2008, 110, 1175-1181.

CHAPTER 12

Labeling the amine functionality on carbon nanotubes

Carbon nanotubes have been envisioned as an potential candidate for various bioapplications ranging from drug delivery to biosensors owing to their unique optical, electrical and mechanical properties. Most of the applications require CNTs to be functionalized using conventional organic chemistry routes. Primary amine functionality being a versatile group in organic chemistry has been widely used to functionalize CNTs. This chapter describes a unique way to tag this amine functionality on CNTs using an aldehyde molecule which forms indole adduct with two adjacent primary amine groups. This indole adduct shows strong fluorescence signal in the 380-450 nm region. With the help of this optical signal, it is possible to study the extent of functionalization as well as to use this signal to monitor CNTs in biological studies. We characterized this system with fluorescence and Raman spectroscopy.

12.1 Introduction

Carbon nanotubes, the seamless graphene cylinders, have achieved an important place in the nanoscale science because of their unique electronic, mechanical and structural properties. A wide range of applications have been realized among which bio-related applications such as nucleic acid sensing [1], gene delivery [2], drug delivery [3], biomedical imaging [4] have attracted a considerable interest recently.

Understanding of complex biological processes at molecular level is the greatest challenge in the modern biology; especially in the post-genomic era. The difficulty lies in the tracking of individual steps of multistep processes because of their multiple kinetic paths and transient intermediate states.

One of the approaches to overcome these challenges is to monitor the behavior of individual biological molecules and complexes, in vitro and in live cells by optical imaging techniques. In this context, carbon nanotubes proved to be a potential material as they fluoresce in the near-infrared region [5] and thus can be tracked out. Most importantly they appear non-toxic [6] and biocompatible [7] at cellular level. The presence of curvature in carbon nanotubes makes them ideal for further functionalization which is important in interfacing with biological systems. Through proper functionalization it is possible to engineer new materials with improved or altogether new, unique properties which can be used as new devices in biological systems.

Fluorescence visualization of nanotubes is an extremely useful technique that can be instrumental in developing nanotubes to become flexible, facile building blocks for fabricating electro-optic devices, as biological nanoprobes for cytological investigation, for micromanipulation under a light microscope, or as in situ, fluorescently detectable microsensors. Fluorescent labeling of single-walled nanotubes (SWCNTs) was attempted before using both covalent [8] and noncovalent modifications [9].

However, so far both approaches did not produce satisfactory results. Covalent modifications alter the sp2-bonded graphene sidewall and change physical properties of SWCNTs [10]. Besides the fluorophores covalently or non-covalently [11] attached to the nanotube surface were quenched due to energy transfer to the nanotube. On the other hand, the noncovalent attachment using such dyes as long-chain dialkylcarbocyanines [12] resulted in significant buildup on the SWCNTs creating bulky structures visible with optical microscopes even without fluorescence.

In this study, we have been able to create a unique fluorescence signal for carbon nanotubes through functionalization with 1, 2-phthalic dicarboxaldehyde (OPTA) molecule. OPTA is a bifunctional, fluorescent chemoaffinity label which is known to have absolute specificity for amino acids and thiol groups and has been used to ascertain the conformational flexibility and polarity of the active sites in enzymes [13]. It forms an isoindole derivative by cross linking the proximal thiol and amino groups and this isoindole derivative fluoresce in the region 420 - 480 nm.

It has been also reported that OPTA is capable of forming a fluorescent complex

by combining with two primary amine groups that are separated by 1.5 - 3 nm distance [14]. The diameter of SWCNTs being in the range 2-12 nm provides an ideal surface to fulfill this condition.

12.2 Experimental

SWCNTs were obtained from Prof. Apparao M. Rao, Clemson University. 1, 2-phthalic dicarboxaldehyde compound and ethylene diamine were purchased from Sigma-Aldrich.

The 15 mg of SWCNTs were refluxed in 6 M HNO_3(v/v 3:1) at 80 °C for 3 h to create surface oxygenated functionalities. The SWCNTs were then treated with $SOCl_2$ at 90 °C for 2 h to form acid chlorides. Finally they were treated with ethylene diamine (EDA) at 55 °C to form primary amines. The reaction mixture was filtered through PTFE membrane (47 mm, 0.2 μ) and washed several times with methanol. The sample was dried in a vacuum oven at 60 °C.

The FTIR spectra were recorded using a Perkin-Elmer 16 PC FTIR spectrophotometer. Five milligrams of SWCNT-EDA were mixed with one milligram of OPTA compound in ethanol solvent with the aid of bath sonicator.

The fluorescence signals were measured with SWCNTs dispersed with 1% sodium dodecyl sulphate solution. Excitation signal was 338 nm. All the measurements were carried out in pH 7 solution. The photoluminescence measurements were taken using Perkin-Elmer LS 55 spectrophotometer.

The Raman experiment was carried out using Dilor XY spectrometer having triple monochromator coupled with liquid nitrogen cooled CCD. Excitation wavelength of 514.5 nm from an Argon ion laser had been used with laser spot size 2 μm and the power density used was 2.38 mW/μm^2. This micro Raman experiment was carried out using Olympus microscope (model BH2) and a 50 x objective from Nikon.

12.3 Results and Discussions

Figure 12-1 shows the schematic representation of the carbon nanotubes functionalization with ethylene amine and subsequently with OPTA compound. The SWCNTs were refluxed overnight with 6M HNO_3 at 100 °C to remove metal catalyst particles and also to create oxygenated surface functional groups.

Infrared studies show the predominance of carboxylic groups among other surface functionalities. These carboxylic groups were further treated with thionyl chloride to convert them to acid chlorides which when treated with ethylene diamine form amide linkages with primary amine groups for further derivatization.

The OPTA molecule binds with the two adjacent primary amine groups to create fluorescence signal by forming an indol adduct.

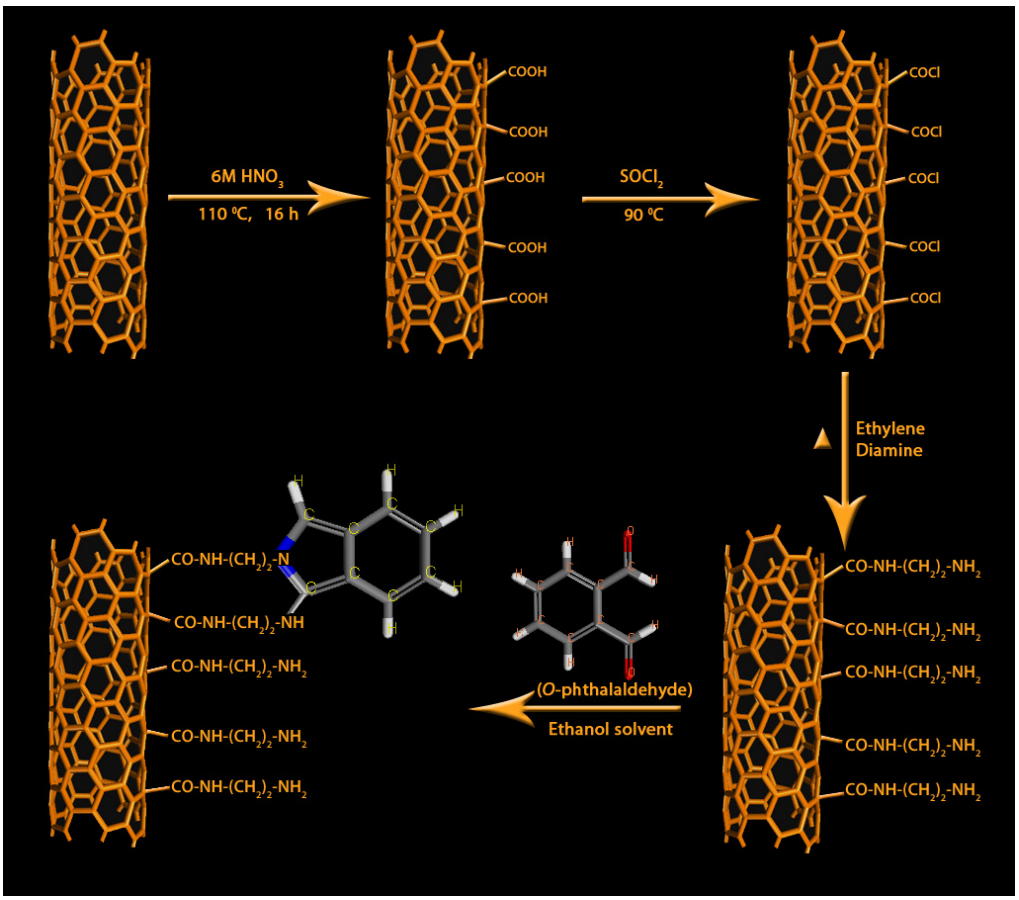

Figure 12-1. Schematic illustration of the SWCNT functionalization route to create amine functionality along the tube-walls and tube-ends. The primary amine functionality of SWCNT reacts with the OPTA molecules to create a photoluminescence signal.

12.3.1 FTIR analysis

The surface chemical changes of SWCNTs after functionalization were followed by FTIR spectroscopy. Figure 12-2 shows the FTIR spectra of SWCNTs and amine functionalized SWCNTs. Acid treatment creates a number of functional groups on the CNTs such as α-diketone, ketone, phenolic, carboxylic, carbinol, hydroquinoid, lactone of which the carboxylic groups are predominant [15]. These carboxylic groups can be further derivatized to create different functionalities.

The carboxylic groups were further derivatized to primary amines through amide linkage as seen in the figure 12-2. The FTIR spectrum of SWCNT-EDA shows peak at 1120 cm^{-1}, 1636 cm^{-1}, and 2933 cm^{-1}, which can be assigned to stretching vibrations of C-O single bonds and C-H bonds respectively.

The broad band at 3400 cm^{-1} can be assigned to O-H stretching vibrations in alcohols. The peaks at 2950, 2920, 2850, 1460, and 1335 cm^{-1} are assigned to the aliphatic C-H stretching. The peaks at 3862 cm^{-1}, 3765 cm^{-1}, 2924 and 2049 cm^{-1} are attributed to

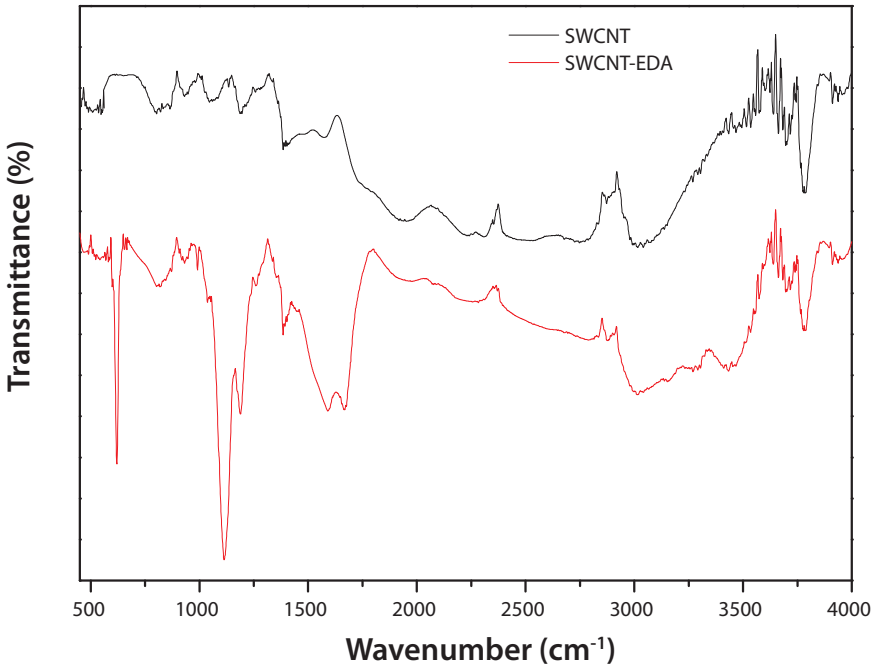

Figure 12-2. FTIR spectra of SWCNT and SWCNT-EDA. The changes in the surface functionalities can be conveniently followed by FTIR analysis.

N-H stretching and C-H stretching respectively. The peaks at 3865 cm^{-1}, 2345 cm^{-1}, 1028 cm^{-1}, 1667 cm^{-1}, and 818 cm^{-1} indicate N-H stretching , C-H, C=O, and C-N stretching respectively [16].

12.3.2 Fluorescence spectroscopy

The fluorescence signals were measured with SWCNTs, SWCNT-EDA, and SWCNT-EDA-OPTA samples dispersed in 1% sodium dodecyl sulphate solution with an excitation signal 338 nm. All the measurements were carried out in pH 7 solution.

OPTA is a bifunctional, fluorescent chemoaffinity label which is known to have absolute specificity for amino and thiol groups. OPTA forms an isoindole derivative by cross-linking amino groups, the formation of which can be detected spectrofluorometrically by monitoring the increase in fluorescence at 338 nm.

In brief, one of the two aldehyde groups of OPTA react with the one of the primary amine of SWCNT resulting in the release of a water molecule. The residual aldehyde group reacts with the other primary amine group of SWCNT with a release of another water molecule and forms a fluorescent isoindole derivative.

It has been shown that SWCNTs act as a quencher when coupled with richly aromatic compounds such as pyrenes[17], porphyrins [18] and phthalocyanines [19]. It is believed that these compounds from Pi-Pi stacking with SWCNTs which act as energy-sinkers as they accept electrons from a fluorophore resulting in the quenching of the

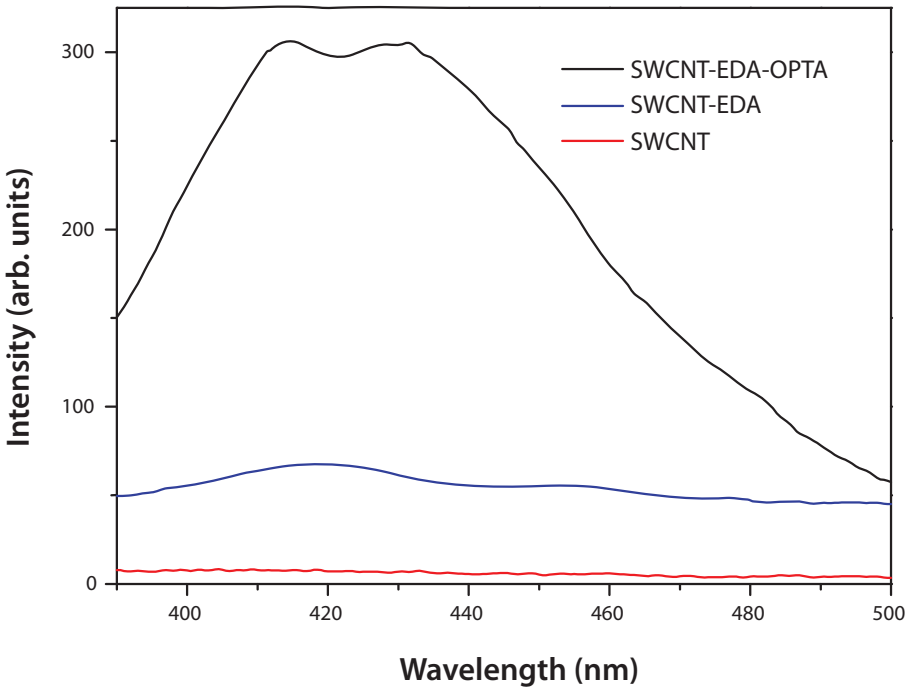

Figure 12-3. Fluorescence spectra of SWCNTs, SWCNT-EDA, and SWCNT-EDA-OPTA samples at pH 7 with an excitation signal 338 nm.

fluorescence.

Figure 12-3 shows the fluorescence spectra of SWCNTs, SWCNT-EDA, and SWCNT-EDA-OPTA samples.

Lack of - stacking with SWCNT in the formation of isoindole derivative preserves the fluorescence. Thus the reaction presents a clean–cut method for tuning the optical properties of CNTs for imaging applications. The initial surface functionalization SWNTs with amine groups not only renders the solubility- a necessary step for the manipulation of CNTs properties to fully realize their various applications, but also serves as potential sites for further derivatization such as drug molecules, as –NH2 has been proved the most versatile group in the organic chemistry. In this context, the method should also be useful in the quantification of surface functionalities of CNTs which is quite difficult due to their weak release.

12.3.3 Raman spectroscopy

Figure 12-4 shows the Raman spectroscopy of the SWCNTs and SWCNT-EDA-OPTA samples recorded with 514.5 nm excitation .

The shift in G-band and its consequent broadening clearly indicates the chemical functionalization of the sidewalls of SWCNT. The nanostructures of functionalized SWCNTs provides a ubiquitous opportunity to OPTA for the formation of a complex with

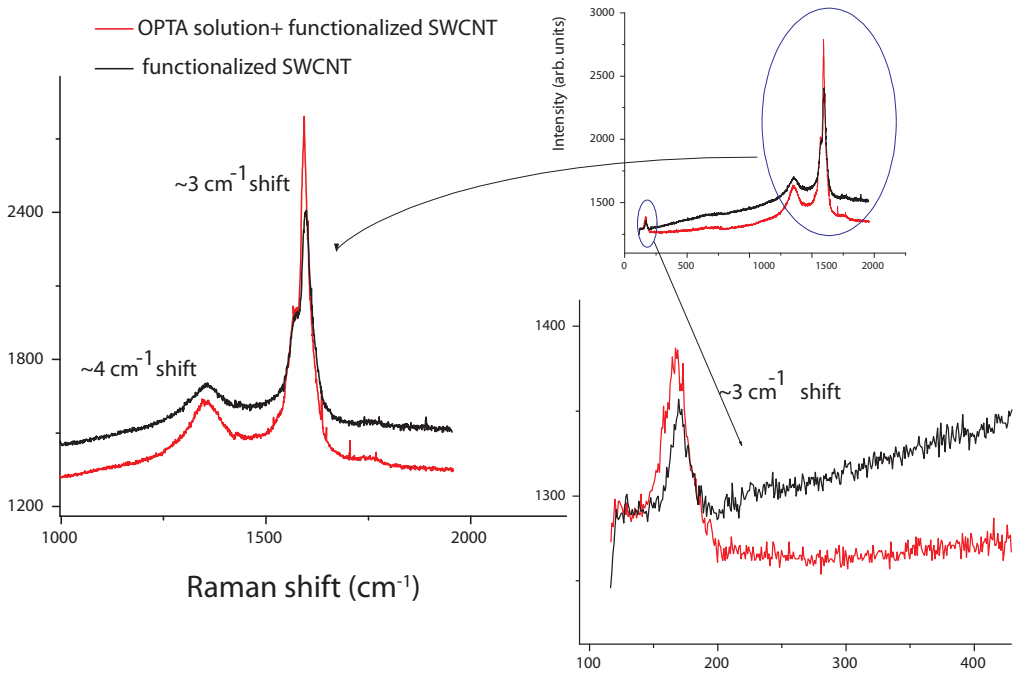

Figure 12-4. Raman spectra of SWCNT-EDA and SWCNT-EDA-OPTA. Expanded regions of RBM frequencies and D and G bands show shifting of the peaks resulted from the functionalization.

two primary amine groups that are separated by 1.5 - 3 nm distance.

There is a ~3 cm^{-1} shift in the RBM region peaks while D and G -bands are shifted by ~4 and ~3 cm^{-1} indicating charge transfer reactions between the nanotubes and surface functionalities [20].

12.4 Conclusions

This chapter describes the unique way to label the amine functionality present on the SWCNTs using an OPTA molecule. This aldehyde molecule forms an indol adduct when it combines with the two primary amine groups of SWCNTs. The indole adduct shows a strong fluorescence in the region of 420 -480 nm. The SWCNT were first functionalized with carboxylic groups via oxidation reaction. The carboxylic groups were converted to acid chlorides and then to amides via ethylene diamine reaction. The changes in the surface functionalities of SWCNTs were followed by FTIR analysis. The adjacent amine groups of SWCNTs were involved adduct formation with OPTA molecule and this adduct showed a strong and broad fluorescence signal. Raman spectra shows the shift in the peak positions in the RBM region as well as in the D and G-band positions indicating charge-transfer reactions.

12.5 References

1. C. Staii, A. T. Johnson Jr, M. Chen, A. Gelperin, Nano Lett 2005, 5, 1774-1778.
2. D. Pantarotto, R. Singh, D. McCarthy, M. Erhardt, J. P. Briand, M. Prato, K. Kostarelos, A. Bianco, Angewandte Chemie 2004, 116, 5354-5358.
3. A. Bianco, K. Kostarelos, M. Prato, Current Opinion in Chemical Biology 2005, 9, 674-679.
4. J. H. Choi, F. T. Nguyen, P. W. Barone, D. A. Heller, A. E. Moll, D. Patel, S. A. Boppart, M. S. Strano, Nano Lett 2007, 7, 861-867.
5. M. J. O'connell, S. M. Bachilo, C. B. Huffman, V. C. Moore, M. S. Strano, E. H. Haroz, K. L. Rialon, P. J. Boul, W. H. Noon, C. Kittrell, Science 2002, 297, 593.
6. D. Pantarotto, J. P. Briand, M. Prato, A. Bianco, Chemical Communications 2004, 2004, 16-17.
7. M. Shim, N. W. S. Kam, R. J. Chen, Y. Li, H. Dai, Nano Letters 2002, 2, 285-288.
8. S. Ravindran, S. Chaudhary, B. Colburn, M. Ozkan, C. S. Ozkan, Nano Letters 2003, 3, 447-453.
9. H. Murakami, T. Nomura, N. Nakashima, Chemical Physics Letters 2003, 378, 481-485.
10. S. Banerjee, T. Hemraj Benny, S. S. Wong, Advanced Materials 2005, 17, 17-29.
11. C. Ehli, G. M. A. Rahman, N. Jux, D. Balbinot, D. M. Guldi, F. Paolucci, M. Marcaccio, D. Paolucci, M. Melle-Franco, F. Zerbetto, J. Am. Chem. Soc 2006, 128, 11222-11231.
12. M. K. Gheith, V. A. Sinani, J. P. Wicksted, R. L. Matts, N. A. Kotov, Advanced Materials 2005, 17, 2663-2670.
13. S. P. George, M. B. Rao, European Journal of Biochemistry 2001, 268, 2881-2888.
14. U. B. Rawat, M. B. Rao, European Journal of Biochemistry 1997, 246, 344-349.
15. T. Ramanathan, F. Fisher, R. Ruoff, L. Brinson, Chem. Mater 2005, 17, 1290-1295.
16. G. Vukovic, A. Marinkovic, M. Colic, M. Ristic, R. Aleksic, A. Peric-Grujic, P. Uskokovic, Chemical Engineering Journal 2009.
17. V. Georgakilas, K. Kordatos, M. Prato, D. M. Guldi, M. Holzinger, A. Hirsch, J. Am. Chem. Soc 2002, 124, 760-761.
18. H. Li, B. Zhou, Y. Lin, L. Gu, W. Wang, K. A. S. Fernando, S. Kumar, L. F. Allard, Y. P. Sun, J. Am. Chem. Soc 2004, 126, 1014-1015.
19. D. Tasis, N. Tagmatarchis, A. Bianco, M. Prato, Chem. Rev 2006, 106, 1105-1136.
20. A. Rao, P. Eklund, S. Bandow, A. Thess, R. E. Smalley, Nature 1997, 388, 257-259.

CHAPTER 13

Summary and conclusions.

This chapter is the summary and conclusion of the work described in the previous chapters along with an outline of the possible future work.

The unique structural, electronic, and mechanical properties of carbon nanotubes have already pushed the boundaries of science. The advancements brought by these tiny materials are not restricted to the scientific discoveries, but are reflecting in the development of everyday real-world applications. The range of applications that has been made possible by carbon nanotubes is so vast, it is almost impossible to cover the entire field because of the rapid pace of developments.

This thesis focuses on three distinct areas that have been developed as a result of recent advances in energy related applications, mechanical reinforcement as well as selective enrichment of particular electronic species, and bio-related applications of carbon nanotubes. Although these domains of study are quite conventional, typical efforts have been made to develop those beautiful gray areas which offer new perspectives.

The first part of the thesis describes the supercapacitor applications of carbon nanotubes for the superior energy storage devices. We synthesized different allotropes of carbon that included beads, spheres, bamboo-like nanotubes and multi-walled carbon nanotubes. The energy storage capacity of each of these allotropes was evaluated using cyclic voltammetry and impedance technique. Carbon nanotubes showed better storage capacity owing to their high surface area, intertubular structure and the presence of surface oxygenated functionalities at the tube ends and along the tube walls. The availability of high surface area, and relatively inert electrochemical nature of carbon nanotubes have been fully utilized in combination with metal oxide nanoparticles (RuO_2 and IrO_2) and polymers (PAN and PBI) to achieve superior energy storage. The composite of nanotubes and PBI polymer provides a new way for the flexible and portable devices with an ability to operate at high temperature.

The second part of the thesis is focused on the development of high-performance polymer composites not only for the mechanical reinforcement but also for the selective enrichment of specific chirality. The PBI-terphthalate copolymer selectively disperses semiconducting SWCNTs and exhibits remarkable optical properties potentially useful for photovoltaic applications. The BPDA polyimide renders the solubility of nanotubes in aprotic polar solvents as well as less polar solvents along and the composite film showed mechanical reinforcement. The composite of PVDF-multi-walled carbon nanotubes showed increase in the dynamic storage modulus as well as changes in the electronic properties.

The third part of the thesis is focused on the bio-related applications of the carbon nanotubes. We have developed a novel method for the synthesis of nanosized hydroxyapatite and its polymorphs on the carbon nanotubes matrix using cheap agro-based materials such as wheat bran. The biocompatibility study of the composite showed promising results and should be useful in the artificial bone grafting applications. We have developed a superior method for the cracking of cellulose to glucose and cellobiose using carbon nanotubes. The conversion of biomass to biofuels has got immense applications. For most of the biological applications, it becomes necessary to functionalize carbon nanotubes using conventional organic chemistry routes. The decoration of carbon nanotubes with amine functionality offers many advantages as amine group is the most

versatile functional group in organic chemistry. We have developed a unique way to tag this amine functionality on nanotubes using an aldehyde molecule that forms an indole adduct with two adjacent amine groups. The adduct showed strong fluorescence signal in the 380-450 nm region, thus providing an opportunity to quantify the amine functionality on carbon nanotubes. Quantification of functionalization on carbon nanotubes is otherwise a difficult task because of the slow release of functional groups.

Although much progress has been made for realizing the practical applications of carbon nanotubes, several challenges remain. Separating and sorting carbon nanotubes by their electronic type is the holy grail of carbon nanotube science. The development of methods for selective enrichment of particular chirality and the scaling-up procedure for nanotube separation would be the area of research for near future work.

Appendices

• List of Publications

1. Arabale, G., Wagh, D., Kulkarni, M., Mulla, I. S., Vernekar, S. P., Vijayamohanan, K. and Rao, A.M. (2003). Enhanced supercapacitance of multiwalled carbon nanotubes functionalized with ruthenium oxide. Chemical Physics Letters, 376, 207-213.

2. Kulkarni, M., Kothawade, S., Arabale, G., Wagh, D., Vijayamohanan, K., Kulkarni, R. A. and Vernekar, S. P. (2005) Synthesis and characterization of polyimides and co-polyimides having pendant benzoic acid moiety. Polymer, 46, 3669-3676.

3. Dandekar, M.S., Arabale, G. and Vijayamohanan, K. (2005) Preparation and characterization of composite electrodes of coconut-shell-based activated carbon and hydrous ruthenium oxide for supercapacitors. Journal of Power Sources, 141, 198-203.

4. Hebalkar, N., Arabale, G., Sainkar, S. R., Pradhan, S.D., Mulla, I.S., Vijayamohanan, K., Ayyub, P. and Kulkarni, S. K. (2005) Study of correlation of structural and surface properties with electrochemical behavior in carbon aerogels. Journal of Material Science, 40, 3777-3782.

5. Khan, M., Sood, A. K., Mohanty, S. K., Gupta, P. K., Arabale, G. V., Vijayamohanan, K. and Rao, C.N.R. (2006). Optical trapping and transportation of carbon nanotubes made easy by decorating with palladium. Optics Express, 14, 424-429.

• Manuscripts in Preparation/Submitted

1. Chirality dependent functionalization of carbon nanotubes with polybenzimidazole-terphthalate copolymer- Selective photobleaching in the NIR region. Arabale, G., Kulkarni, M. (Journal of American Chemical Society)

2. Labeling the amine functionality on carbon nanotubes. Arabale, G., Vinod, P., Bellare, J. (Chemical Communication)

3. All solid-state carbon nanotubes polybenzimidazole supercapacitor. Arabale, G. (Journal of American Chemical Society)

4. Which carbon allotrope is best for supercapacitor applications? Arabale, G., (Journal of Physical chemistry-C)

5. Making biocompatible hydroxyapatite-carbon nanotubes composites by enzymatic way. Arabale, G., Soni, S., Khire, J., Bellare, J. (Advanced Materials)

6. Optical and electrochemical storage properties of carbon nanotubes- PBI oxadizole composites. Arabale, G., Potrekar, R., Vernekar, S. (Advanced Materials)

7. Solubilzing carbon nanotubes with long-chain polyimides. Arabale, G., Sadavarte, N., Wadgaonkar, P., Bellare, J. (Journal of Physical chemistry-C)

8. Immobilization of pepsin on with and without amine functionalized carbon nanotubes-Biocataclytic activity and structural changes. Arabale, G., Vinod, P. Bellare, J. (Journal of Physical chemistry-C)

9. Iridium oxide functionalized carbon nanotubes for supercapacitor applications. Arabale, G. (Applied Physics Letters)

10. Carbon nanotubes- PVDF composites: Structural and mechanical changes. Arabale, G., Bellare, J. (Journal of Physical chemistry-C)

11. Energy storage applications of carbon nanotubes-PAN composites. Arabale, G. (Applied Physics Letters)

12. Dielectric properties of carbon nanotubes and cellulose acetate composites Arabale, G., Shaikh, H. Bellare, J. (Polymer)

• Patents

1. An improved process for the preparation of high surface area carbon useful for fuel cell and ultracapacitor. US Patent (Pat. No. NCL-7/2003) D. Wagh, G. Arabale, M. Kulkarni, S. P. Vernekar, K. Vijayamohanan.

2. An improved process for the fabrication of ultracapacitor electrodes using activated lamp black carbon, US Patent (Pat. No.0251 NF 2004/US) M. Dandekar, G. Arabale, S. P. Vernekar, K. Vijayamohanan.

3. All solid state supercapacitors with polybenzimidazole membrane as an electrolyte. US Patent (submitted to NCL-47/2004) G. Arabale, M. Dandekar, U. K. Kharul, S. P. Vernekar, K. Vijayamohanan.

• Conferences

1. Preparation of supercapacitive material from coconut shell carbon. 13th Annual General Meeting of the MRSI held at IICT/DMRL Hyderabad, 7-9 Feb. 2002

2. Synthesis and characterization of carbon aerogels for supercapacitor applications. Sixth International Conference on Nano-structured Materials, 16-21 June 2002, Orlando, USA

3. Enhanced supercapacitance of multiwalled carbon nanotubes functionalized with RuO2. American Physical Society Meeting, Austin, March 2003

4. Preparation and characterization of high surface area activated carbon/RuO2 composite electrodes for supercapacitor applications. National Seminar on Fuel Cell, DRDO, Ambernath, 26-27 Oct. 2003

5. All solid state supercapacitors with polybenzimidazole polymer electrolyte membrane. Oral presentation in the International conference on electrochemical power systems (ICPES-2)

6. Supercapacitor behavior of RuO2 nanoparticles attached on coconut shell carbon. Poster presentation in the International conference on electrochemical power systems (ICPES-2)

7. Optical trapping and transportation of palladium decorated carbon nanotubes. International Conference on Nano Science & Technology, ICONSAT 2006, (March 16-18, 2006), India Habitat Centre, Lodhi Road, New Delhi

• Invited Talks

1. Talk-Carbon Nanotubes-Polymer Composites. Workshop on “Smart Polymers and Composites for Defence Applications”. 07 Sept. 2006, Defence Institute of Advanced Technology, Pune – 411 025.

2. Talk-Carbon Nanotubes-(R)evolutionary Material. Workshop on “Smart Materials for Defence Applications”. 28 Aug. 2008, Defence Institute of Advanced Technology, Pune – 411 025.